Molecular Manipulation

with the Scanning Tunnelling Microscope

by

Sumet Sakulsermsuk

A thesis submitted to

The University of Birmingham

for the degree of

DOCTOR OF PHILOSOPHY

Nanoscale Physics Research Laboratory

School of Physics & Astronomy

The University of Birmingham

September 2010

Abstract

This thesis presents two studies into molecular manipulation using scanning tunnelling microscopy (STM), dissociation of chrolobenzene (PhCl) and of 4,4′-dichlorobiphenyl (PCB) manipulation both on Si(111)-7×7 surface. An ab initio investigation is presented on a possible candidate for future atomic manipulation.

The dissociation of PhCl process on the Si(111)-7x7 surface was studied using an STM. STM induced dissociation was found to be temperature dependent and requires 1.4 ± 0.1 electrons per C-Cl bond breaking event. Based on work and previous work, we suggest this is a mixture of a two-electron temperature independent and one-electron temperature dependent processes. The activation barrier for the thermally assisted one-electron dissociation was measured to be 0.8 ± 0.2 eV. This appears to reflect the measured energy barrier of diffusion of 0.84 ± 0.08 eV, suggesting that the thermally promoted dissociation process proceeds via a precursor physisorbed state.

Electron injection from STM was used to induce atomic manipulation of PCB on Si(111)-7×7 surface. Four types of manipulation outcomes were observed; desorption, double dark feature, single dark feature and the generation of a bistable adsorbed switching. The PCB bi-stable switching was voltage independent, but injection tip-site dependent. This suggests that the switching process is driven by thermal excitation, but that the tip-adsorbate interactions play a role.

The computational study of naphthalene 1,8-disulfide (NDS) in gas phase was performed by the density functional theory calculations using molecular orbitals. The S-S bond lengths of NDS^{2-}, NDS^{-}, NDS, NDS^{+} and NDS^{2+} were predicted to be 3.46 Å, 2.74 Å, 2.13 Å, 2.09 Å and 2.06 Å. Therefore the disulfide bond is a strong candidate to undergo vibrational excitation due to respectively short lived ionic molecules created by charge injection from an STM tip.

To my mother and father

Acknowledgements

I would like to thank my supervisor Prof. Richard E. Palmer for giving me the opportunity to conduct a challenging and interesting research project in nanoscience. His advice and encouragement helped me to carry on working at a high standard for my PhD. I also thank my co-supervisor Prof. Roy L. Johnston for his guidance and support in the computational work.

I would like to thank Dr. Peter A. Sloan for training, discussions and helping me when I was doing my PhD. We have worked together in the same team since the new RHK STM arrived. I could not have done my PhD at this level without his support. His scientific enthusiasm and attitudes have influenced mine. There are plenty of things I learned from him, not only science. I also would like to thank Dr. Oliver Paz Borbon for his help when I worked in Prof. Roy L. Johnston's group.

I would like to thank all members of NPRL for their support and friendship. I would especially like to thank to Chris, James, Mi Yeon, Jedsada and Xin who gave me helpful advice during my studies. I would like to thank Dr. Wolfgang Theis for writing computer program at the beginning of the analysis work presented in chapter 4. I thank Vahideh and George for reading chapters 3 and 4 of my PhD draft. I also thank previous members in Chemistry, Andy, Gareth, Ben, Oliver, Nicola, Adam, Sam for their kind hospitality.

I would like to thank the Thailand Higher Educational Strategic Scholarship for financial support.

I would like to thank Thomrat and her family for all of their support, especially before I came to study in Birmingham. Without her help, I would not have come this far.

I would like to thank my family who always support and console me. I dedicate this thesis to my parents.

Contents

Chapter 1

Introduction

Since 1959, when Feynman outlined his vision in the talk, "There's plenty of room at the bottom" [1], the dawn of nanotechnology has emerged. In his talk, he suggested there is no physical law to prevent us from arranging atoms in any way we want. This would allow us for example to write letters using atoms on a surface. If we were to write all the letters of an encyclopaedia this way, it would only be the size of the head of a pin. However, we did not even have a tool to "see" atoms directly at the time of this talk. This obstacle was overcome in 1982 by the invention of the scanning tunnelling microscope (STM) by Binnig and Rohrer [2,3] as a local probe with the ability to look at individual atoms and molecules. Four years later, another family of local probe atomic force microscopes (AFM) was developed [4]. Atoms on a surface were first shown to be controlled precisely by an STM tip in the remarkable work of Eigler and Schweizer [5] in 1990 on arranging Xe atoms on a nickel surface. The age, or at least the beginning, of manipulation of matter at the atomic and molecular levels had arrived. STM has played a critical role in development of nanoscience and nanotechnology [6,7], especially in molecular electronics [8,9], nanomachinery [10] and single molecule chemistry [11]. This use of STM makes it suitable to be described as a "Feynman machine" [12]. Recent applications have included the study of organic superconductors [13] and the manipulation of spin in single atoms [14-17].

The trend of current technology based on fabrication is to go towards smaller dimensions [18]. The need to control fabrication at the molecular scale in a "bottom-up" approach will be reached soon. The chemistry and physics of aromatic organic molecules on solid surfaces has been central to many industrial technologies [19]. Controlling adsorbed organic molecules on silicon with STM gives possibilities to characterize the electrical properties of these hybrid organic semiconductor systems and to build prototypes of fundamental devices [20].

Nanostructure fabrications, such as computer chips, use the desorption of molecules in the dry etching process, such as desorbing $SiCl_2$ by thermally activated etching with Cl [21]. Fabrication at the molecular level can reach sub-Ångstrom resolution with STM lithrography [22]. In the field of catalysis, dissociation of water to generate hydrogen is highly interesting as a renewable energy candidate [23]. The various pathways of water dissociation on MgO have been studied by STM [24]. Hybrid silicon-organic microelectronic devices are attracting much interest, benefitting from advances in molecular electronics [25,26]. This should provide better stablility, lower noise and lower power losses. Advances in hybrid molecular electronics have contributed to other applications, for instance, sensors [27] and organic transitors [26]. A silicon-based quantum computer could also be built using molecular manipulation, either based on nuclear spin qubits [28] or cellular automata [29,30]. Therefore, molecular manipulation has a wide range of technological applications and demands.

My PhD project is aimed at manipulating the molecules chlorobenzene and polychlorinated biphenyl using electrons from an STM tip. The motivation is to advance the understanding of building of blocks of molecular devices. I have also simulated the naphthalene disulfide molecule using first principles electronic structure calculations. The introduction and results are divided into six chapters as follows. The fundamentals of STM and an introduction to atomic manipulation are presented in Chapter 2. This includes some of the most significant historical work in this field, for example, moving Xe atoms by an STM tip with lateral manipulation, transferring a Xe atom to a tip apex, and breaking chemical bonds inside molecules. Chapter 3 is dedicated to the experimental set up used for the work presented in this thesis. Ultrahigh vacuum experiments, working with vacuum chambers and vacuum pumps are described. Details of the STM used in the experiments, sample preparations and computer program for analysis are also described. Chapter 4 shows the first experimental results and the highlight of my thesis. The results show a new mechanism of C-Cl bond dissociation of chlorobenzene on a silicon surface. Also, nonlocal dissociation of chlorobenzene is found and described separately in appendix A. In Chapter 5, the investigation of atomic manipulation is studied on single polychlorinated biphenyl molecules. An STM tip was positioned at different sites within this molecule to inject electrons to induce bond dissociation. Various reactions were observed including binding site switching. This may aid the development of controllable

molecular switches as basic units of molecular logic devices. Besides C-Cl bond breaking, the dissociation of the S-S bond is interesting, as it has an important role in protein conformation [31]. Chapter 6 shows molecular simulation of the naphthalene disulfide molecule using density functional theory (DFT). The structures and charge transfer of negatively and positively charged ions are calculated and discussed. Extension and distortion of the S-S bond due to the addition of electron(s) to the neutral molecule was explored in negatively charged ions. In appendix B, a list of publications based on the work in this thesis is presented.

Chapter 2
Review of scanning tunnelling microscopy and atomic manipulation

At the atomic scale, quantum physics governs the behaviour of particles and matter. Scanning tunnelling microscopy (STM) is an instrument that utilizes the quantum tunnelling of electrons between a sharp tip and a substrate. Surface imaging by STM has marked a leap forward in surface science. The application of STM goes beyond just imaging the substrate surface, to the manipulation of atoms and molecules. This chapter presents the principles of STM and an introduction to atomic manipulation.

2.1 Scanning tunnelling microscopy

STM was originally a surface imaging technique, revealing surface structure at an atomic resolution in three dimensions. It was invented by G. Binnig and H. Rohrer [3] who received the Nobel Prize in physics in 1986. The key principle of STM is to exploit the quantum tunnelling effect of electrons in the very small junction between a conducting surface and a sharp metal tip when a bias voltage is applied between these two electrodes.

2.1.1 Quantum tunnelling

Here, we discuss quantum tunnelling of a beam of particles incident on a rectangular potential barrier in one dimension. Each particle has energy E and the potential barrier has height U and width d as shown in Fig. 2.1. From quantum mechanics, the state of each particle can be described by a wave function $\Psi(z)$. These wave functions can be derived from the time-independent one-dimensional Schrödinger equation,

$$\frac{-\hbar^2}{2m}\frac{d^2}{dz^2}\Psi(z)+U\Psi(z)=E\Psi(z). \tag{2.1}$$

The wave function is considered in three regions (Fig. 2.1).

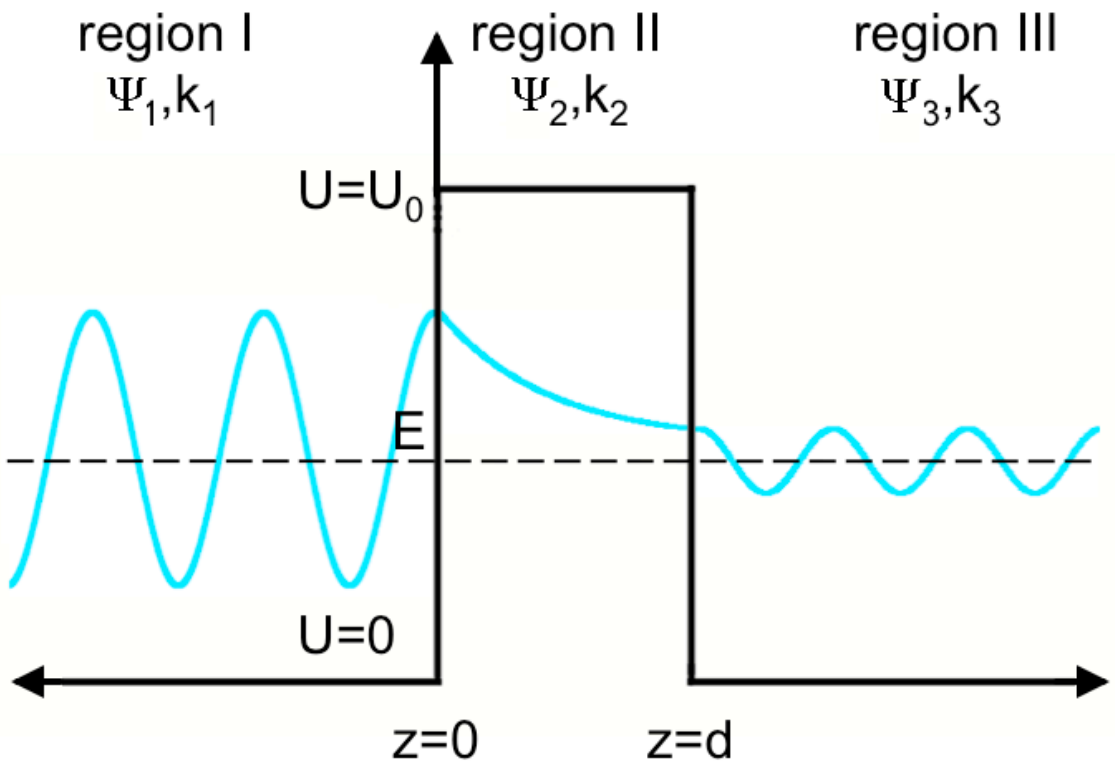

Figure 2.1. One-dimensional rectangular potential barrier which has height U and width d. Incident electrons have energy E.

Region I: $z \le 0,\ U = 0$

The wave function of the incoming particles can be written as $\Psi(z) = Ae^{ik_1 z} + Be^{-ik_1 z}$ where $k_1 = \frac{\sqrt{2mE}}{\hbar}$, m is the mass of the particle, E is the energy of particle and $\hbar$ is Planck's constant divided by 2π. The amplitude of the incident wave is set to be 1 ($A = 1$). Therefore,

$$\Psi(z) = e^{ik_1 z} + Be^{-ik_1 z}. \tag{2.2}$$

Region II: $0 \le z \le d,\ U = U_0$

The wave function in the barrier can be written as

$$\Psi(z) = Ce^{k_2 z} + De^{-k_2 z} \tag{2.3}$$

where $k_2 = \frac{\sqrt{2m(U_0 - E)}}{\hbar}$ is the decay constant.

Region III: $d \le z, U = 0$

$$\Psi(z) = te^{ik_1 z},\ d \le z \tag{2.4}$$

where $k_1 = \frac{\sqrt{2mE}}{\hbar}$.

Equations (2.2)-(2.4) have four unknown parameters which can be solved by applying continuity conditions at the two boundaries.

At region I/II ($z = 0$),

$$\Psi_I(0) = \Psi_{II}(0)$$
$$\frac{d\Psi_I(0)}{dz} = \frac{d\Psi_{II}(0)}{dz}$$

At region II/III ($z = d$),

$$\Psi_{II}(d) = \Psi_{III}(d)$$
$$\frac{d\Psi_{II}(d)}{dz} = \frac{d\Psi_{III}(z)}{dz}.$$

Then, we have

$$\begin{aligned} 1 + B &= C + D \\ ik_1(1 - B) &= k_2(C - D) \\ Ce^{k_2 d} + De^{-k_2 d} &= te^{ik_1 d} \\ k_2 Ce^{k_2 d} - k_2 De^{-k_2 d} &= ik_1 te^{ik_1 d}, \end{aligned}$$

in which t can be determined

$$t = \frac{2k_1 k_2 e^{-ik_1 d}}{2k_1 k_2 \cosh(k_2 d) + i(k_1^2 + k_2^2)\sinh(k_2 d)}. \tag{2.5}$$

Thus, the transmission of particles through the barrier is

$$T = |t|^2 = \frac{1}{1 + \frac{1}{4}\left(\frac{k_2}{k_1} + \frac{k_1}{k_2}\right)^2 \sinh^2(k_2 d)}. \tag{2.6}$$

There is a non-zero probability of finding electrons that have tunnelled to the other side of the potential barrier. For $k_2 d >> 1$,

$$T \approx \frac{16k_1^2 k_2^2}{(k_1^2 + k_2^2)^2} e^{-2k_2 d} \propto e^{-2k_2 d}. \tag{2.7}$$

Therefore, the probability of transmission is proportional to an exponential decrease in the barrier width.

2.1.2 Principles of STM

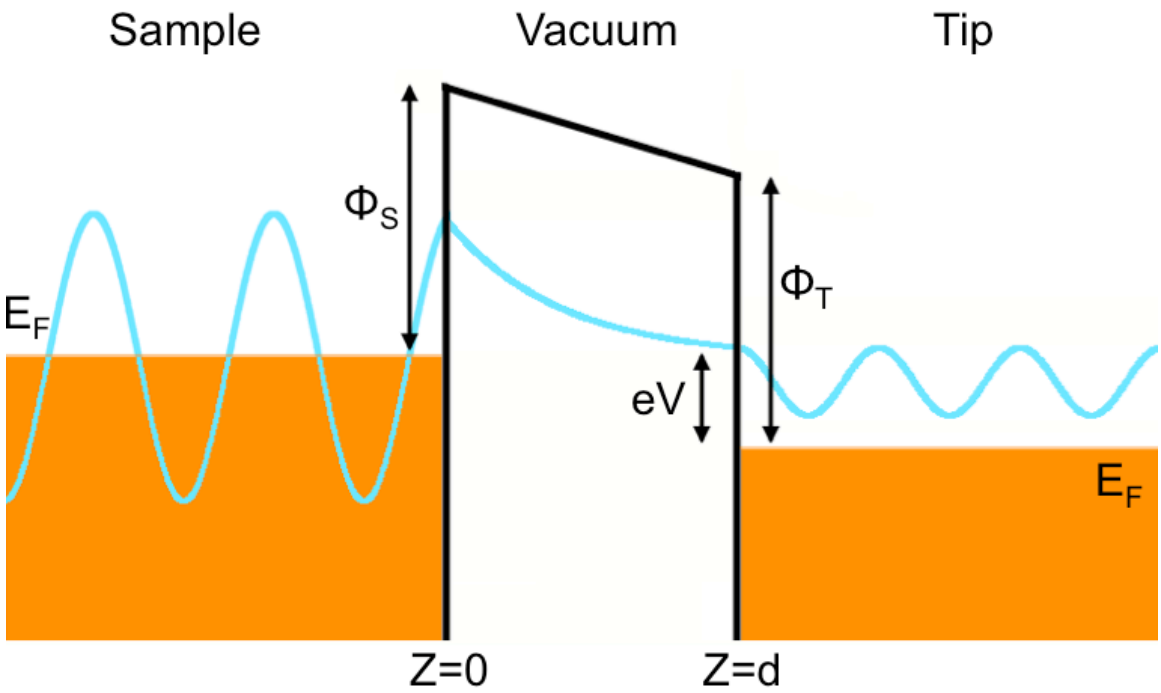

Figure 2.2. One-dimensional energy diagram of a sample-vacuum-tip tunnelling junction. Φ_S and Φ_T are the work functions of a sample and a tip. A positive bias voltage was applied to the tip.

An STM contains a tip and a substrate as electrodes. The tip is positioned close to the substrate, ~ 5-10 Å [32-33] and a bias voltage is applied to the electrodes to make an electron current tunnel through the vacuum energy barrier between these two electrodes. Three-dimensional movement of the tip at sub-atomic resolution is governed by applying voltages to piezoelectric materials attached to the tip. The tunnelling effect in the STM junction can be explained similarly to tunnelling in a one-dimensional rectangular barrier. In an STM junction, applying a bias voltage V to the sample leads to the Fermi energy (E_F) of the sample shifting from equilibium, resulting in an energy gap of eV between these two electrodes. The vacuum level was chosen to be the reference level. Thus, the electrons at E_F of the sample need energy

equal to the work function (Φ_S) to overcome the sample-tip barrier as displayed in Fig. 2.2. Electrons in occupied states between E_F and $E_F - eV$ of the sample have a non-zero probability of tunnelling to unoccupied states of the tip. To calculate the probability of tunnelling, we assume that the work function of the sample (Φ_S) and tip (Φ_T) are identical to the work function of the normal metal electrode used in STM, which is in the 4-6 eV range. Also, eV is assumed to be very small compared to Φ_S. Therefore, the sample-tip energy barrier can be taken as an approximately rectangular barrier and only states (Ψ_n) near $E_n \approx -\Phi_S$ the sample Fermi level have a chance of tunnelling. The wave function inside the barrier (region 2 from the previous section) can be written as

$$\Psi(z) \approx De^{-k_2 z} \propto \Psi_n(0)e^{-k_2 z} \tag{2.8}$$

where $|D|^2 >> |C|^2$ and where k_2 is the decay constant,

$$k_2 = \kappa = \frac{\sqrt{2m\Phi}}{\hbar} \tag{2.9}$$

where m is the electron mass. Thus,

$$\kappa = 0.51\sqrt{\Phi}\ \text{Å}^{-1}, \tag{2.10}$$

Φ being the work function in eV.

As the tip scans across the surface, the tip states are constant while the sample states vary with the location of the tip on the surface. The probability of an electron in the nth sample state tunnelling to the tip is

$$P_n(d) \propto |\Psi_n(0)|^2 e^{-2k_2 d}. \tag{2.11}$$

The tunnelling current is proportional to the summation of the probabilities of an electron having an energy state in the range of $E_F - eV$ to E_F tunnelling to the tip surface

$$I \propto \sum_{E_n = E_F - eV}^{E_F} \left|\Psi_n(0)\right|^2 e^{-2\kappa d} . \tag{2.12}$$

This summation of probabilities can be written as the local density of states (LDOS) on the sample $\rho_S(z,E)$, which is a function of the distance from the surface and the energy state. The LDOS can be expressed as

$$\rho_S(z,E) = \frac{1}{\varepsilon} \sum_{E_n = E-\varepsilon}^{E} \left|\Psi_n(z)\right|^2 \tag{2.13}$$

where ε is small enough.

The tunnelling current in Equation (2.12) can be written in form of an LDOS as

$$I \propto \rho_S(0,E_F) e^{-2\kappa d} V. \tag{2.14}$$

From (2.3) and $D >> C$, thus

$$\Psi(d) = \Psi(0)\exp(-\kappa d). \tag{2.15}$$

Then, we have

$$I \propto \rho_S(d,E_F) V \tag{2.16}$$

which means that the tunnelling current is proportional to the LDOS at the Fermi level of the sample. By taking $\Phi \approx 4$ eV, we have $\kappa \approx 1$ Å^{-1}. Therefore, if the sample-tip distance decreases

by 1 Å, the tunnelling current increases by an order of magnitude. The tunnelling current is sensitive to the sample-tip distance at the sub-atomic level. Since most of the current tunnels to the leading atom of the tip apex, this gives very high lateral resolution as well. By precise vertical control in the STM junction combined with the scanning tip in the *x*-*y* plane, atomic resolution surface images can be generated.

In STM operation, there is one main mode of controlling the vertical axis of a tip, as shown in Fig. 2.3. The tunnelling current in the STM junction is kept constant while the tip height varies. The contour of the tip along the scanning line reflects the height profile of the surface structure. Fig. 2.4 shows a schematic diagram of an STM. A feedback circuit is employed to control tip height for constant-current mode.

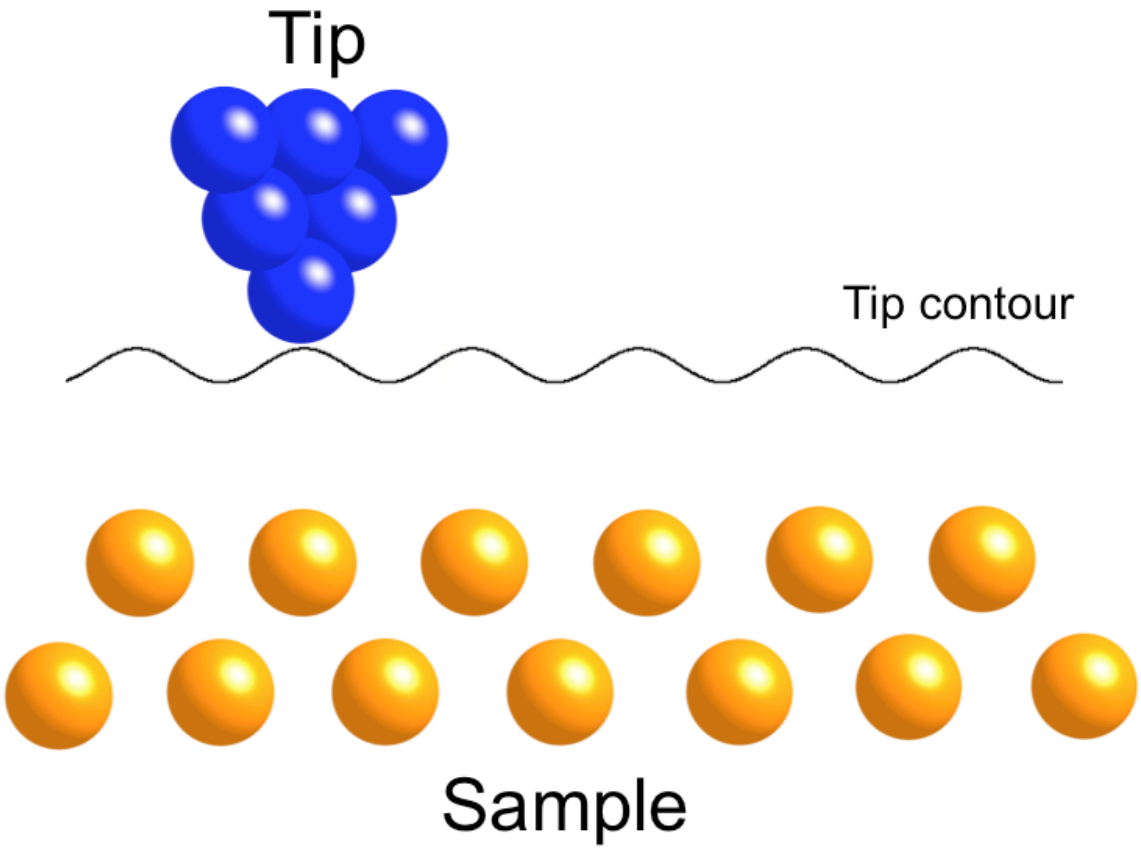

Figure 2.3. Schematic of STM scanning in constant-current mode. The tip contour corresponds to the surface structure.

Differentiating the current with respect to voltage in Equation (2.16) gives

$$\frac{dI}{dV} \propto \rho_S(d, E_F) = LDOS. \tag{2.17}$$

This derivative can be measured from changes in the tunnelling current as the bias voltage varies. The technique is called "scanning tunnelling spectroscopy" (STS).

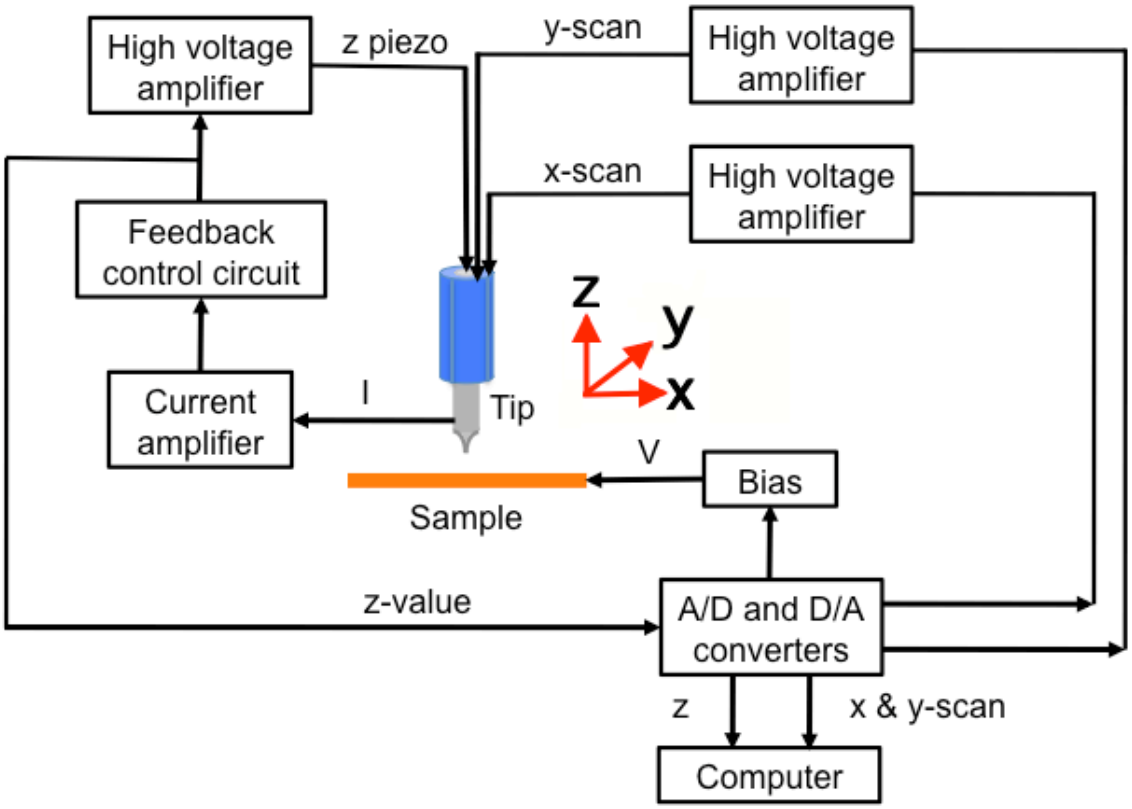

Figure 2.4. Schematic diagram of STM controlling system.

The methods used for my experiments will be described in the remaining chapters.

2.2 Literature review of atomic manipulation

STM is not only used for imaging surfaces, but also it is used to manipulate matter on surfaces. Forces between tip and sample, electric-field and tunnelling current can be employed to control matter. Progress in atomic and molecular manipulation may allow the possibility of achieving such ultimate goals as controlling chemical reactions at the atomic scale or assembling and controlling nanomachines. Here, the categories of STM manipulation mechanism will be described.

2.2.1 Mechanical manipulation

The ability to move an atom on a surface by STM was first noticed by Eigler at IBM's Almaden laboratory. Experiments were performed at low temperature (4 K) to avoid atoms moving from thermal excitation. Eigler *et al.* [5] studied and developed an atomic positioning technique, successfully arranging 35 Xe atoms on a nickel surface in the "IBM" logo (Fig. 2.5). The manipulation procedure can be described as in Fig. 2.6 by (a) the tip is located at the desired atom, (b) the tip is lowered towards the atom to increase the tip-atom interaction, (c) the tip is scanned across the surface to the destination, and (d) retracting the tip back to (e) where the effect of tip-atom interactions is weaker. In a manipulation process, the distance between the tip and the atom relates to the resistance in the tunnelling junction used to indicate the interaction strength of adsorbate-tip in the junction. The tip approaching the atom leads to the overlapping of the wave functions of the tip and the atom, resulting in a weak chemical bond forming between them. This weak bond pulls the atom during manipulation.

Other modes of lateral manipulation were studied by Bartels *et al.* [35], who conducted tip height measurement on single atoms, molecules and dimers during lateral manipulation. They explored "pulling", "sliding" and "pushing" processes with distinct characteristic tip height curves in manipulation (Fig. 2.7 (a)-d)). An attractive force is responsible for the pulling process, a repulsive force, for the pushing process. Changing the manipulation process from

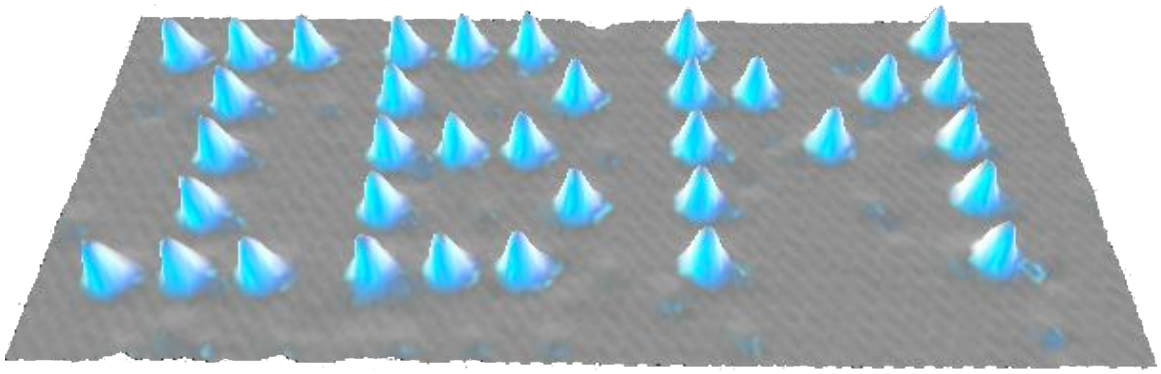

Figure 2.5. “IBM” assembled from 35 Xe atoms on Ni(110). Image taken from IBM website [34].

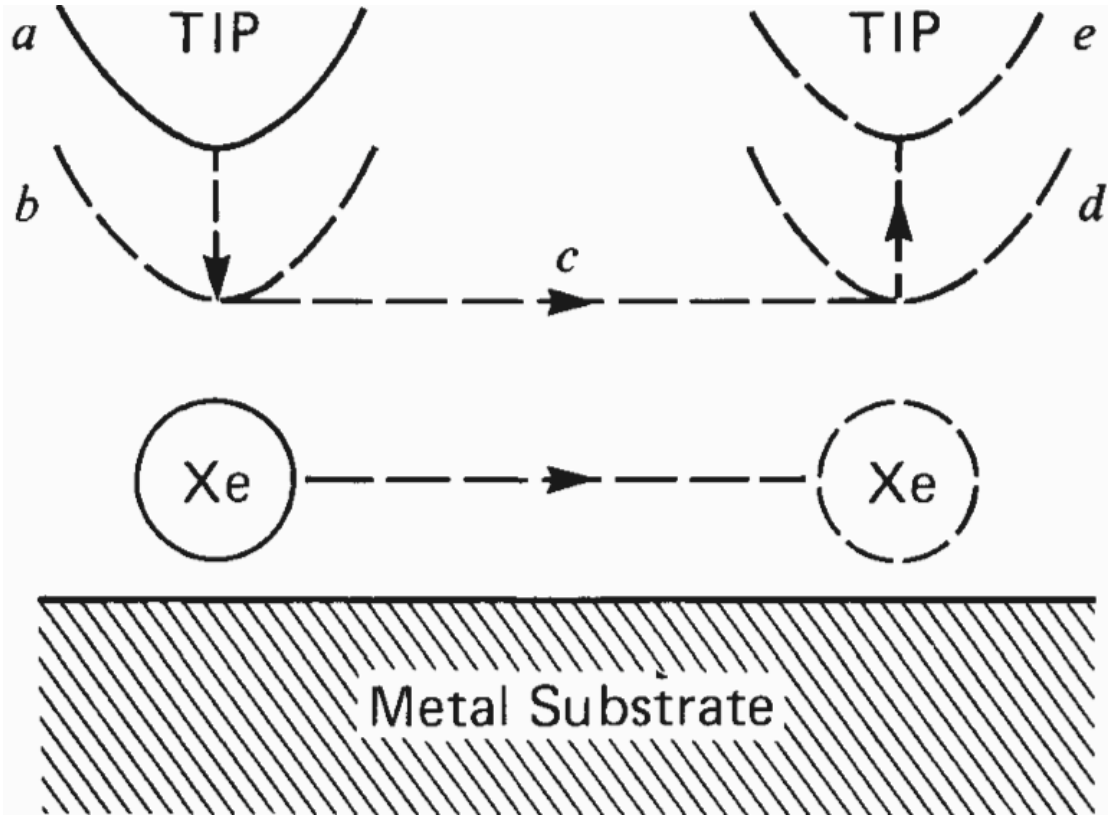

Figure 2.6. Process of sliding an atom across a surface. Picture and caption modified from [5].

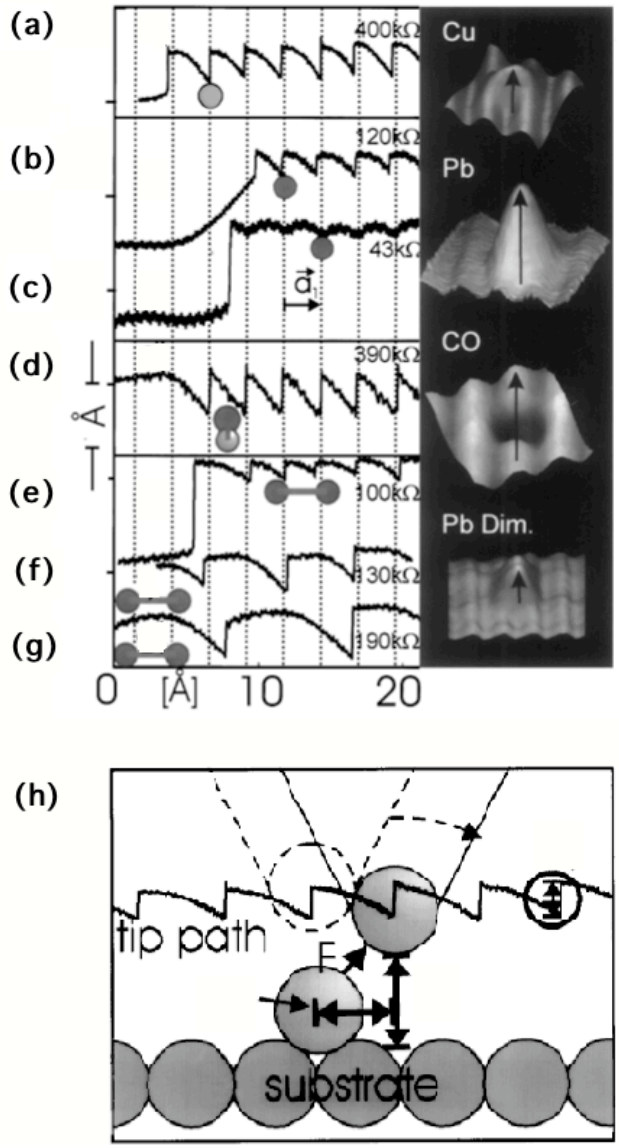

Figure 2.7. The left part shows tip height curves during manipulation of a Cu atom (a), a Pb atom (b,c), a CO molecule (d), and a Pb dimer (e)-(g) along $[1\bar{1}0]$. The tip movement is from left to right, and the tunnelling resistances are indicated. All tip height curves are unfiltered raw data. The vertical dotted lines correspond to fcc sites next to the step edge. In the right part, STM images of the different adparticles are shown. The arrow indicates the direction of tip movement. (h) A measured tip height curve during the pulling of a Cu atom is shown superimposed on a schematic drawing of the positions of the tip apex, the manipulated atom, and the substrate atoms along $[1\bar{1}0]$. Images and caption modified from [35].

pulling to sliding by decreasing the tunnelling resistance (increasing the tip-molecule interaction) was observed in Fig. 2.7 (b) and (c). Single hopping of an atom/dimer corresponds to the measured tip height curves as displayed in Fig. 2.7 (h). Increasing tunnelling resistance produces Pb dimer multiple hopping, compared to single hopping for a tunnelling resistance of 100 kΩ (Fig. 2.7 (e) and (g)). Also, tip-molecule interactions were employed for "rolling" macromolecules on surfaces such as C_{60} [36], wheels in wheel-dimer molecule [37].

The achievement of precise atom relocation by lateral manipulation leads to the possibility of assembling artificial structures using atom-by-atom processes. Crommie *et al*. [38] employed lateral manipulation to construct a circular quantum corral from 48 Fe atoms on a Cu(111) surface (see Fig. 2.8) to study confined electrons in a circular 2D box. A standing wave pattern was observed inside the atomic corral. The LDOS of surface state electrons correspond to the quantum states, $\Psi_n(r,E)$, of a particle in a circular box. The surface resonance pattern inside an atomic stadium was studied using scattering theory by the same group [39]. By employing lateral manipulation to construct quantum corrals, Manoharan *et al*. [40] demonstrated quantum mirages of the Kondo effect at the unoccupied focus in an elliptical quantum corral when a Co atom was placed at one focus of the ellipse. Quantum superposition of two electronic states [41] was investigated in the same system as quantum mirages and the lifetimes of electrons inside quantum corrals [42] were measured. Extraction of quantum phase of confined wave functions in isospectral shapes created by CO molecular corrals was demonstrated by Moon *et al*. [43]. Writing letters by atoms on a surface like Eigler's work [5] is still not the smallest size possible of data storage. This physical limitation on data storage density was overcome by encoding information in three-dimensional spatial space and energy or (**r**-E) space. Quantum holographic encoding was demonstrated by arranging CO molecules in specific designed patterns on surfaces [44], where their LDOS map at particular energy level was predicted as a bit of letters. They also showed that the different bits of letters may be encoded at separated energy levels (like pages in a book) in the same spatial space (Fig. 2.9). The calculated data storage density of a letter in one energy page is ~ 20 bits nm^{-2} while the maximum atomic density is ~9 bits nm^{-2}. Besides quantum behaviour in confined electrons in atomic corrals, atomic chains constructed by metal atoms also express a quantum character in their electronic structure [45-60]. The progress in this field has developed

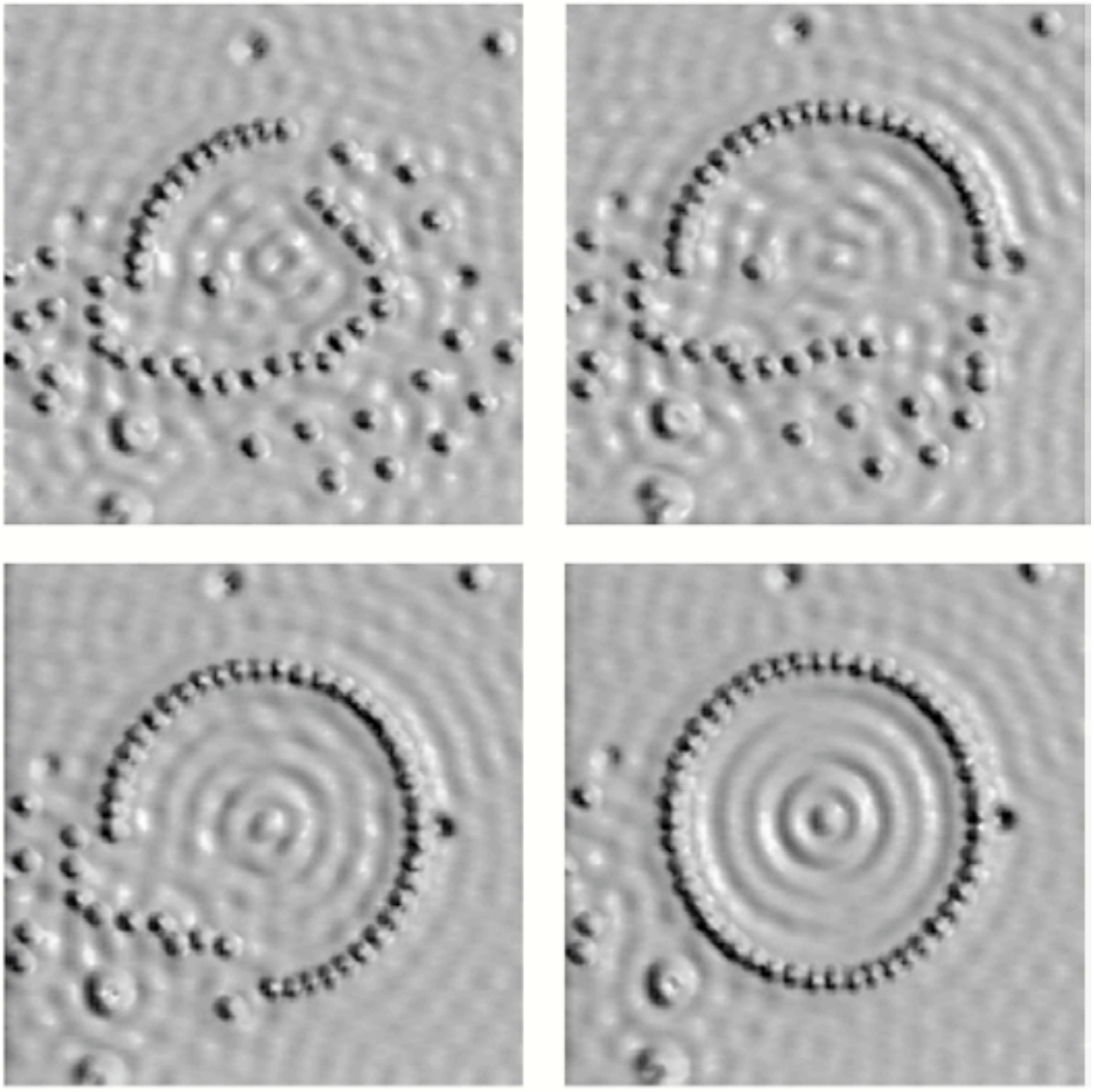

Figure 2.8. Assembly of a circular quantum corral from 48 Fe adatoms on Cu(111). Average diameter is 142.6 Å. Quantum wave resulting from electron confinement in corral was observed. Images taken from the IBM website [34].

applications for quantum information, quantum computation and quantum transport. Not only can quantum devices be accessed from STM built artificial structures, but also atomic mechanical devices can be constructed from atomic manipulation. Eigler *et al.* [61] found that the hopping of CO molecules is activated and controlled by interactions from neighbouring molecules. They

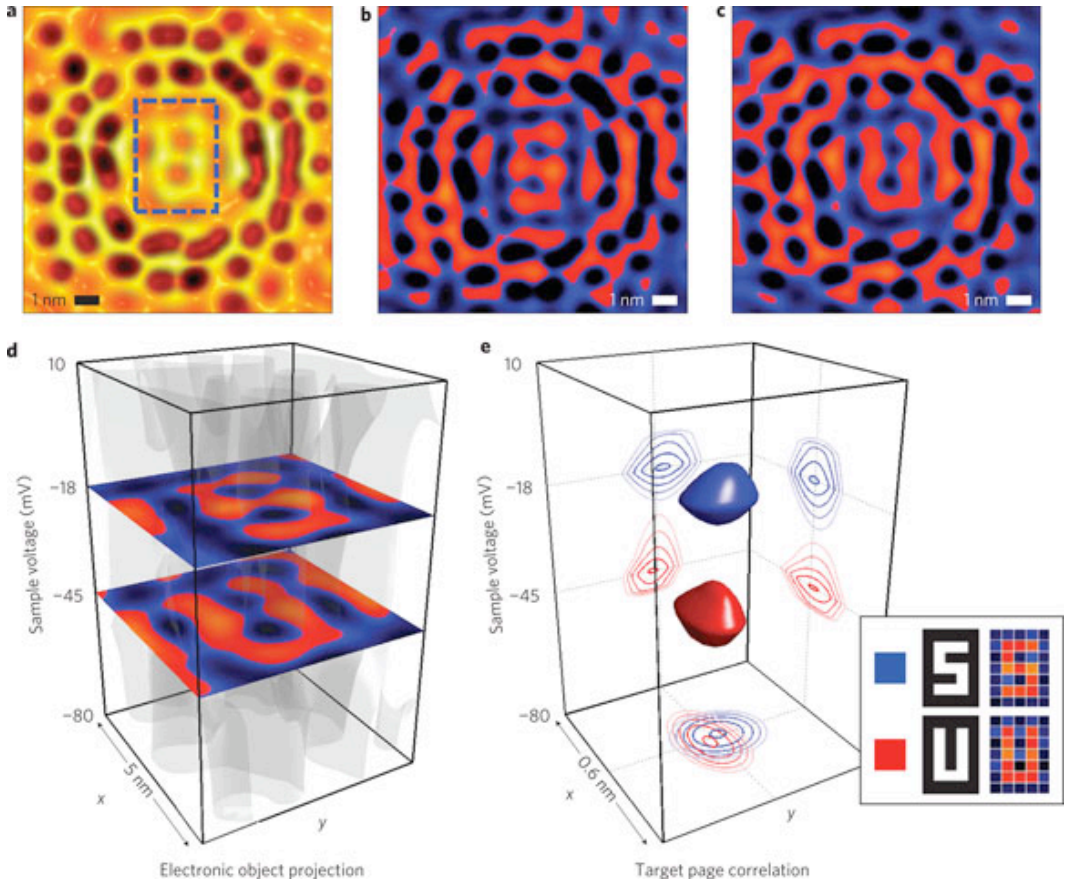

Figure 2.9. Volumetric quantum holography. (a), Topograph (13.5 × 13.5 nm^2; $I = 1$ nA; $V = -60$ mV) of a molecular hologram that encodes two pages of data at different energies in the same region of space. (b), A dI/dV map taken at $V = -18$ mV shows the *S* page. $V_{AC} = 4$ mV r.m.s. (c), Measuring dI/dV at $V = -45$ mV retrieves the *U* page. The molecules are unchanged. (d), by mapping dI/dV at many voltages between −80 and 10 mV, $\rho(r,E)$ was measured throughout the readout region. A translucent surface of constant DOS is shown. Slices through this space at the appropriate energies reveal the *S* and *U* pages. (e), the normalized cross-correlation of $\rho(r,E)$ with each template image (insets) was computed as a function of r and E. Surfaces of constant correlation (at 98% of the global maximum) are shown for each page, confirming their locations in the information cube. Contours show the maximum correlation projected in each dimension (95-99.9%). Images and caption modified from [44].

positioned CO molecules in a pattern such that one hopping molecule can activate another hopping and so on, producing so-called "molecule cascades". The series of consequential molecular hopping was exploited to design basic logic operational gates, i.e. AND and OR gates. Atomic logic circuits were fabricated from combinations of these basic gates. This success shows the promise of mechanical computational devices at the atomic scale [62]. But it remains to be seen how to scale-up to the production of nanoscale devices.

Forces used in mechanical lateral and vertical manipulation were measured with AFM for Co and CO on a Cu(111) surface [63]. The force required in moving atoms and molecules was found to be strongly proportional to the interactions of the adsorbates and the surface. Approaching a tip toward molecules in vertical manipulation can lead to the relaxation of the internal molecular bond and the formation of an interface state between the tip apex and the specific bond in the molecules [64-67].

2.2.3 Electric field induced manipulation

Since distances in tunnelling junctions are ~10 Å, an intense electric field of ~10^9 Vm^{-1} exists in this gap. Whitman *et al.* [68] exploited this field effect to induce diffusion of Cs atoms at room temperature to create chain nanostructures such as nanowire. This field modifies the energies of dipole atoms and molecules on surfaces where the tip is localized above absorbates, especially non-zero dipole moment absorbates. The dipole moment of an absorbate in the electric field is found by

$$\vec{p} \cong \vec{\mu} + \alpha\vec{E} \tag{2.18}$$

where $\vec{E}$ is an electric field and $\vec{\mu}$ is the dipole moment of the adsorbate. $\alpha\vec{E}$ is the induced dipole moment, where α is the polarizability of the absorbate. Energy of the dipole moment is perturbed by the field:

$$U_E(\vec{r}) \cong -\vec{\mu}\cdot\vec{E}(\vec{r}) - \frac{1}{2}\alpha\vec{E}(\vec{r})\cdot\vec{E}(\vec{r}). \tag{2.19}$$

Therefore, there is a force corresponding to the potential energy gradient on the atom or molecule in the field, which is used to control the direction of atom diffusion. In their work, attractive interaction results in forming longer Cs chains.

Non-reversible vertical atomic relocation of adatoms from surface to tip induced by electric-field was reported in Si(111)-7×7 [69-71]. Dujardin *et al.* [72] used vertical manipulation to extract individual Ge atoms from a Ge(111) surface. This technique is reliable enough to pick up single Ge adatoms on the surface without perturbing neighbouring Ge adatoms. Atoms transferred to the tip create vacancies on the surface, which was confirmed by calculations of tip height of vacancy and adatoms. The calculation of the potential energy (Fig. 2.10) for this system suggested the energy barriers for an adatom transference from surface to tip is reduced when the tip approaches close to the adatom (from 8 Å). When the tip-surface distance is at 3.5 Å, the potential wells of the tip and the surface start to join. As the tip approaches closer to the surface, both wells merge into a single well (Fig. 2.10 (d)). This leads to there being no energy barrier for a Ge adatom to overcome in transferring to the tip apex. An electric field was employed to further reduce the energy barrier in atomic transfer by increasing the bias voltage to +3 V (Fig. 2.10 (c)). Changing the direction of the electric field by switching the polarity of the bias voltage can displace atoms or molecules from the surface to the tip or vice versa, for example CO functionalized tips [73-75]. The electric field under an STM tip has a major role in inducing desorption of NO molecules [76]. The electric field also results in the the reduction of the energy barrier for surface atoms transferring to a tip [77] as demonstrated on a Ge(111) surface [72]. A high electric field ($V \geq 4$) is able to extract Si atoms from a silicon surface, creating nano-grooves [70] on Si(111)-7×7 and nano-pits [78] on Si(001)-2×1.

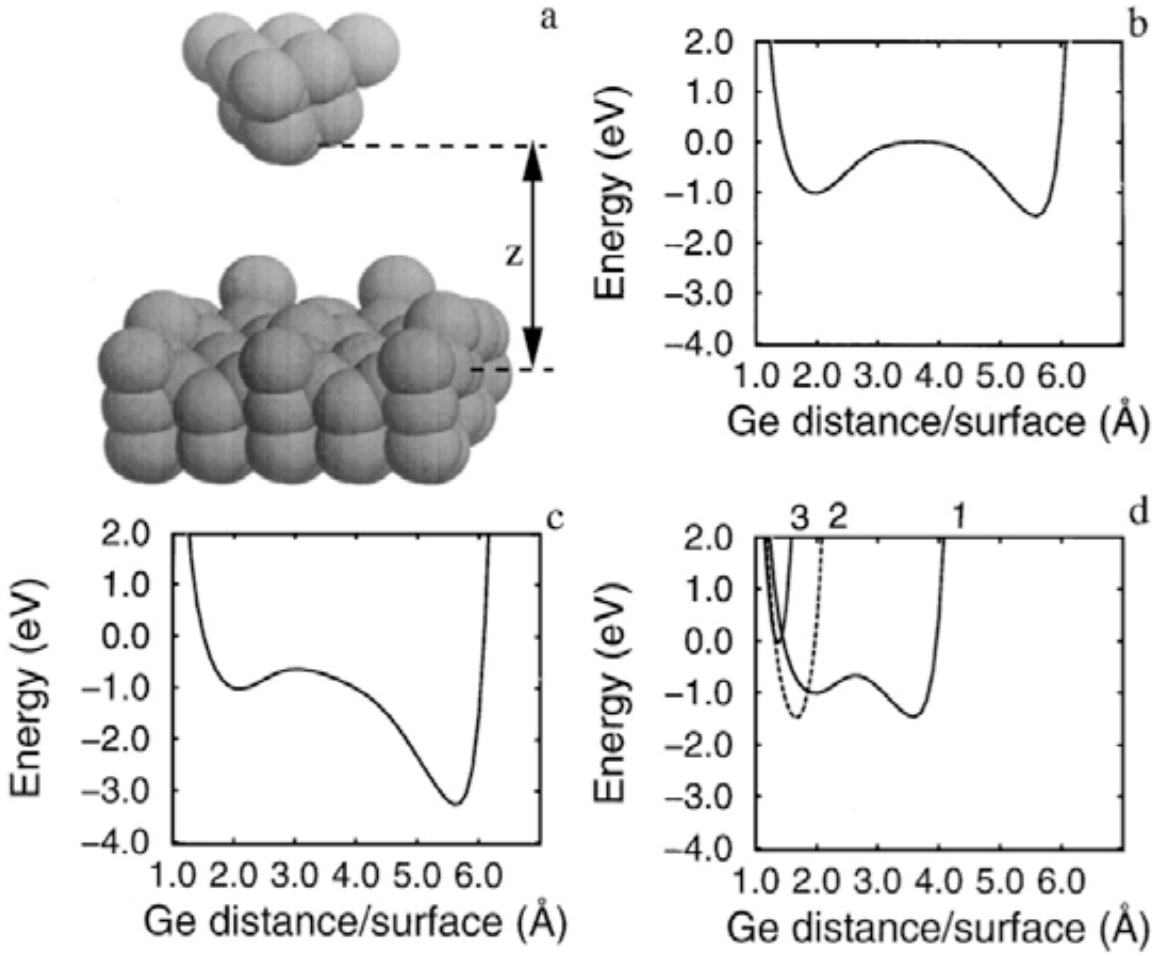

Figure 2.10. Calculated potential energy curves of a Ge adatom positioned between a Ge tip apex and a Ge(111) surface as a function of the Ge adatom altitude above the surface for different tip-sample distances *z*. In (a), a standard ball representation of the junction considered. In (b), the imaging mode, where $I = 1$, i.e., $z = 8$ Å with the tip apex lying along the surface normal of the Ge adatom. In (c), the tip apex is stopped above the Ge adatom at $z = 8$ Å. Then a sample bias voltage of +3 V is applied inducing the suppression of the surface Ge potential well. In (d), the merging of the two wells when the tip apex gently approachs the Ge adatom for $z = 6$ Å (curve 1), $z = 4$ Å (curve 2), and $z = 3.5$ Å (curve 3). The zero in energy is given by the energy of the three components of the junction (tip apex, Ge adatom, and surface) at very large separation. Images and caption modified from [72].

2.2.4 Inelastic tunnelling induced manipulation

Atoms and molecules can be manipulated with inelastic tunnelling (IET) electrons, where tunnelling electrons lose energy to excite adsorbates. A process of desorption induced by electronic transitions (DIET) was developed to describe the desorption of molecules induced by laser radiation [79,80]. The DIET process can be understood via the Menzel-Gomer-Redhead (MGR) model [81,82] as in the schematic diagram in Fig. 2.11. The ground state is excited by a Franck-Condon transition to the repulsive excited state. In this transition, the Born-Oppenheimer approximation is applied, where the nuclear positions of adsorbate are unchanged in vertical transition. Then, the adsorbate is quenched from the excited state, resulting in the return of the system to the ground state. Desorption of the adsorbate can occur if the adsorbate gains enough vibrational energy before the quenching transition, otherwise it is recaptured. It is also possible that the recaptured adsorbate is excited repeatedly until it desorbs in a so-called "desorption induced by multiple electronic transition" or DIMET [84]. Not only can desorption occur, but also other chemical reactions, for example, dissociation and diffusion.

For STM manipulation, electronic excitation can be taken by electrons (or holes) attachment where electrons from a tip attach to unoccupied (occupied) states of adsorbate targets, resulting in negative (positive) ions. This type of process was found in desorption of hydrogen on Si(100)-2×1 where electrons attached to σ^* of Si-H bonding state underwent an electronic transition [85]. The dependence of the desorption yields on current suggests the process occurs through vibrational heating of the Si-H bond. As power law of reaction rate ($R \propto I^N$) is considered [86], ten electrons ($N = 10$) [87] are required as multiple vibrational heating corresponding to incoherent excitation [88]. It was found later that the dehydrogenation on an Si-H surface is a single electron process [87] corresponding to coherent excitation [89]. Both coherent and incoherent excitation processes are comparable to DIET and DIMET. Desorption of hydrogen on Si(100)-2×1 by hole attachment with multiple vibrational heating process was reported by Stokbro *et al.* [90].

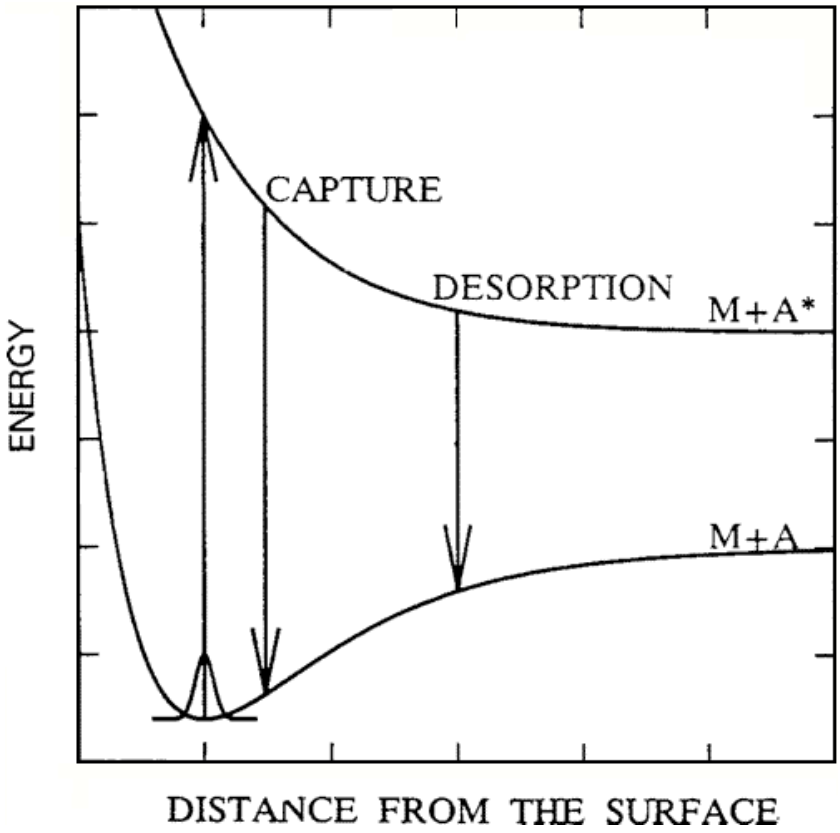

Figure 2.11. Schematic potential energy curves illustrating stimulated desorption in the Menzel-Gomer-Redhead model. A Franck-Condon transition from the ground state takes the system to a repulsive excited state. Quenching of the adsorbate excitation is assumed to return the system to a replica of the ground-state curve. Quenching can lead to either capture or desorption depending on where the quenching transition occurs. Image and caption modified from [83].

The possibility of dissociation of O_2 molecule on Pt(111) induced by tunnelling current was predicted by Salam *et al.* [90]. Experiments of O_2 molecule dissociation on a Pt(111) surface via coherent and incoherent excitation processes in vibrational excitation by injecting tunnelling electrons into individual molecules was reported by Stipe *et al.* [91]. Fig. 2.12 shows two oxygen molecules appearing like pear shapes (a). A pulse of 0.3 voltage was injected from STM tip into one molecule while the feedback loop was disabled. The sudden dropping of current indicates the moment of dissociation (b). Dissociated products can be seen as two oxygen atoms adsorbing on fcc and hcp sites (c). Repeating the process on another molecule resulted in a further two oxygen atoms adsorbed separately on the surface (d). Measurement dissociation rates at 0.4 V, 0.3 V and

0.2 V give the number of electrons (N) involved in the bond breaking process as $N = 0.8 \pm 0.2$, 1.8 ± 0.2 and 2.9 ± 0.3 respectively. Fig. 2.13 (a) presents vibrational excitation in a ladder-climbing mechanism with different energy electrons by inelastic electron tunnelling via the antibonding π^* of O_2. It was assumed that O_2 molecules are excited from the ground state to overcome a dissociation energy barrier of 0.38 eV for five vibrational steps. The vibrational energy of each single climbing step is 87 meV ($= \hbar\omega$). For a bias voltage of 0.4 V, from experimental measurement, $N \approx 1$ is due to excitation from the ground state with single step climbing, corresponding to a DIET-like process. But two and three electrons are needed for bias voltages of 0.3 and 0.2 V as measurement gives $N \approx 2$ and $N \approx 3$ as two and three climbing

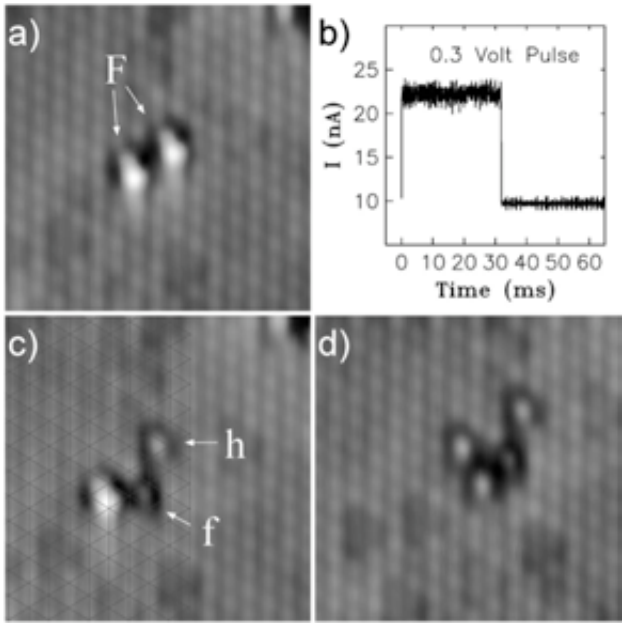

Figure 2.12. (a) STM image of two adjacent pear shaped O_2 molecules on fcc sites. (b) Current during a 0.3 V pulse over the molecule on the right showing the moment of dissociation (step at $t \sim 30$ ms). (c) After pulse image with a grid fit to the platinum lattice showing one oxygen atom on an fcc and one on an hcp site along with the unperturbed neighboring molecule on an fcc site. (d) STM image taken after a second pulse with the tip centred over the molecule showing two additional oxygen atoms on hcp sites. Raw data images scanned at 25 meV sample bias and 5 nA tunnelling current. Images and caption modified from [91].

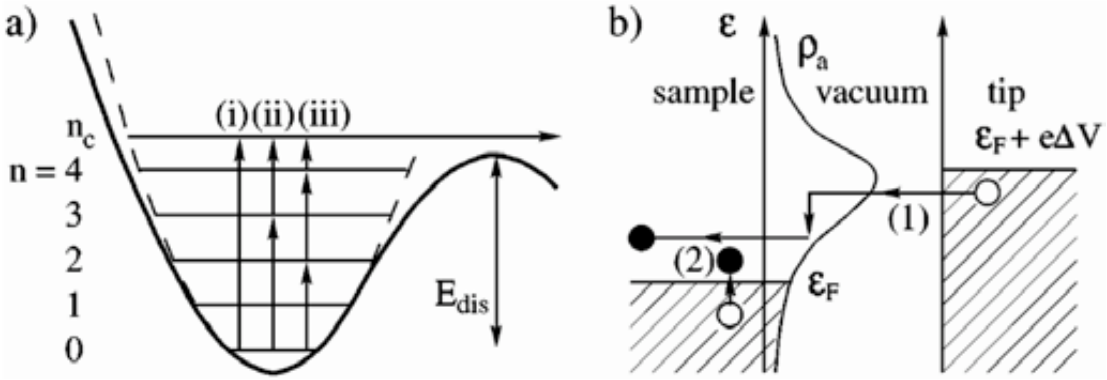

Figure 2.13. Schematic picture of the model for bond breaking of O_2/Pt(111) by inelastic electron tunnelling: (a) Potential is modelled by a truncated harmonic oscillator (dashed line). The three sets of excitations among the levels in (a) represent typical transitions that lead to dissociation for the three applied biases ΔV; (i) 0.4, (ii) 0.3, and (iii) 0.2 V. (b) Inelastic electron tunnelling to an adsorbate-induced resonance with density of states ρ_a induces vibrational excitations, (1), while electronic excitations within the substrate induces vibrational relaxations, (2). Images and caption modified from [91].

steps are needed, corresponding to a DIMET-like process. Fig. 2.13 (b) shows the IET process where tunnelling electrons loss energy through an adsorbate-induced resonance and the vibrational relaxation from electron-hole pair excitation.

In more complex molecules, for example benzene, there is more than one vibrational mode involved in molecule desorption [92]. Desorption of benzene on Si(100) by hole attachment to a π state of the adsorbed molecules was studied by Alavi *et al.* [92]. The sharp threshold of desorption yields, between –1.6 V and –2.7 V suggests electronic excitation for desorption. The desorption of benzene molecules occurs via Si-C bond breaking, where molecules attach to a surface via di σ-bonding in a butterfly-like configuration. They proposed that the ring-bending mode (X) of the molecules is excited and the energy is transferred from this excited mode to the stretched mode of bonding between the molecule and the surface (Z) as schematically shown in Fig. 2.14. Molecules from the ground state (Fig. 2.14 (a)) are excited to a positive ion state (Fig. 2.14 (b)) where the molecules evolve along the surface potential to escape from the bound neutral state, leading to desorption after the molecule relaxes to the neutral state.

Simulation of energy transference to the Z-coordinate is displayed in Fig. 2.15. It takes ~750 fs to escape the bound state, resulting in desorption. Molecular dissociation and desorption of another aromatic molecule by electronic excitation was explored in chlorobenzene on Si(111)-7×7 system [93-95].

Molecules controlled by electronic excitation was reported in studies of biphenyl/Si(100) surface [96-104]. At low temperatures, the biphenyl molecule was found to switch between two adsorption sites (S_1 and S_2) when a negative voltage pulse was applied inside the molecules [104]. It suggests electronic excitation via hole attachment into occupied π orbital of adsorbed biphenyl molecule. Different electronic resonances on two separated positions was also explored using STS of biphenyl molecules. Sub-atomic resolution of the positioning of the STM tip allowed the activation of each individual resonance inside the molecules. This has interesting applications to controlling molecules as nanomachines [105], e.g. molecular switches in molecular logic circuits.

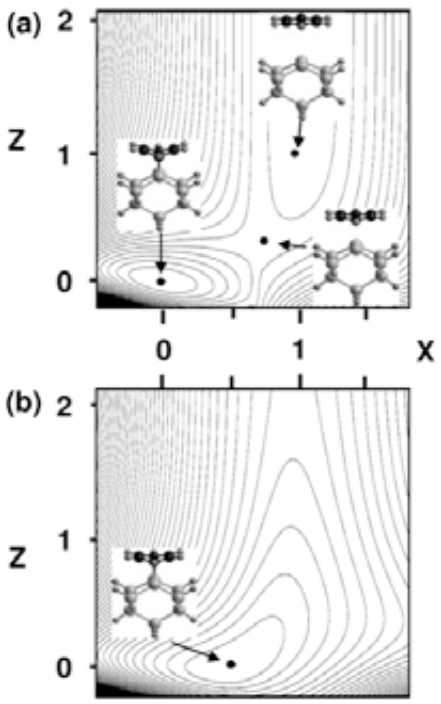

Figure 2.14. Calculated potential energy surfaces vs the dimensionless coordinates X and Z: (a) neutral state; (b) ionic state. Black dots indicate the location of stationary points and the contour curves are spaced 0.2 eV. Images and caption modified from [79].

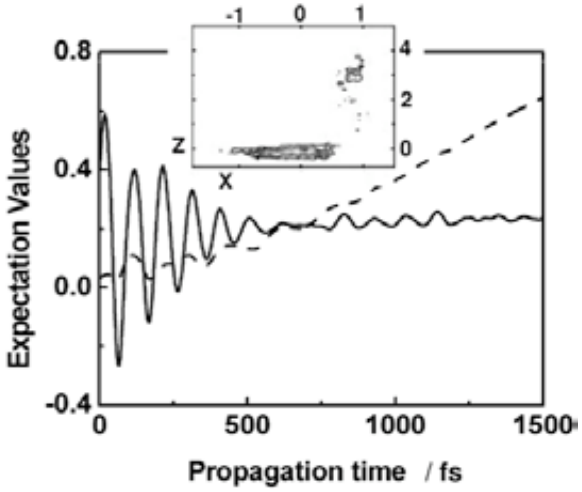

Figure 2.15. Expectation values of X (solid curve) and Z (dashed curve) in the evolving neutral state wave packet subsequent to 25 fs residence in the ionic state. The inset shows a snapshot of the wave packet 750 fs after relaxation to the neutral state. Image and caption modified from [92].

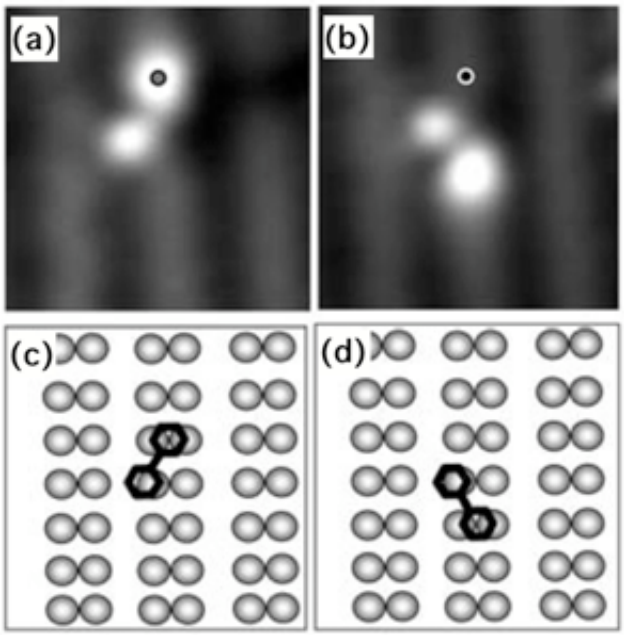

Figure 2.16. (a) and (b) after the surface voltage pulse. The biphenyl switched to its second stable state (S_1) from its original state (S_2). (c) and (e) show schematically the biphenyl molecule in its S_1 and S_2 adsorption configurations, respectively. Images and caption modified from [104].

Electronic excitation can induce electron transition from occupied to unoccupied state of atom or molecule adsorbates. This was found to be the case in desorption of hydrogen/Si(100) [106]. The $\sigma \rightarrow \sigma^*$ transition of the H-Si bond leads to desorption of dehydrogenation on a hydrogen covered Si(100) surface. It requires high voltages, field emission regime, ~6-8 V to make this electronic transition. Parallel experiments with deuterium (D) desorption were also conducted to compare with H. As D has more mass than H, it moves more slowly in an excitation state. This is observed from the lower desorption yield of D compared to H. Moreover, for a system where molecules have weak interactions between tip and surface, it is possible to excite the molecules via electron-hole pair attachment where electron and hole attach to unoccupied and occupied state of adsorbates simultaneously. It is found in fluorescence induced by an STM tip from C_{60} on ultrathin NaCl film grown on Au(111) [107].

It is also possible to use inelastic tunnelling electrons to excite molecular vibrational modes [108,109]. This type of manipulation requires applying low voltage (~mV). Molecular reactions via vibrational excitations can be activated selectively by controlling the current and energy of tunnelling electrons as Pacual *et al.* [110] reported in the desorption and translation of NH_3 molecules on a Cu(100) surface. Each reaction is induced via different internal vibrational modes. From the thresholds of reactions, excitation of the δ_s(N-H_3) mode (408 meV) is found to be responsible for molecular desorption while the ν_s(N-H) mode (139 meV) or umbrella mode is, for molecular translation. The excitation of ν_s(N-H) mode inducing lateral translation suggests energy transfer through anharmonic coupling between two different modes resulting adsorbed molecule motion [111]. From the results of desorption yield as current dependence, there are two mechanism pathways with one-electron process for below tunnelling current at ~ 0.5 nA regime and two-electron process for above, where the δ_s(N-H_3) mode is excited. Therefore, there are three mechanism pathways of Cu-NH_3 bond breaking, which can be selected by desired electron energy and current.

A coupling of particular vibrational modes associated with reactions was proposed as a mechanism for atoms or sub-molecules exchanging their bonding location in the molecules. Chemical transformation at structural molecules [112-119] such as isomerisation [112,113] and chirality [114] also can be induced by vibrational excitation process. Molecules as reaction products can be identified from their characteristic vibrational modes by STM with inelastic

electron tunnelling spectroscopy (STM-IETS) [108,109,115,116]. However, this technique can not reveal exact molecular vibrationally corresponding to molecular motions [117]. The alternative method, called "action spectrum" measuring response of vibrationally mediated molecular motion to applied bias voltage, can reveal vibrational modes which is blind for STM-IETS [117,118]. Sainoo *et al.* demonstrated the advantage of action spectra on reversible motion of *cis*-2-butene molecule on Pd(110). It revealed four vibrational modes excited by inelastic tunnelling current, while the STM-IET detected two modes from these modes. An important role of molecular orbitals (MOs) near the Fermi level (E_F) is to select which vibrational excitation is revealed by Kawai and co-workers [120]. They showed that IET electrons from a tip can excite vibrational modes by attaching to unoccupied MOs near E_F. The spatial distribution of the MOs near the E_F level of adsorbed molecules determines the excited vibrational modes.

Vertical transfer of atoms on surfaces to a tip and vice versa was first demonstrated by Eigler *et al.* [121] for reversible transferring of xenon atoms between a nickel surface and a tungsten tip as an atomic switch. The states of a xenon atom can be controlled by changing the polarity of the bias voltage and applying a current pulse. Controlled vertical manipulation for molecules was showed by Bartels *et al.* [73] with CO molecules/Cu(111) surface. A CO molecule carried on a tip was used as a "chemically functionalized tip" to image other CO molecules with greater contrast. The C atom of CO molecules always bonds with the metal atoms, thus the O atoms locate at the modified tip apex. Further studies on the CO transferring process [74] found that the hopping of the molecules to the tip is induced by electronic transitions by electron attachment to the CO $2\pi^*$ state (see Fig. 2.17). By employing these functionalized tips in vertical manipulation techniques, new vibrational modes inside molecules were explored [75] with STS and also ultimate resolution of chemical bonds of molecules was revealed in the CO functionalized tip using atomic force microscopy (AFM) [122].

Thin insulating films were used to decouple molecules to substrates [123-130]. Repp *et al.* [123] showed on ultrathin NaCl films that the electronic structure of pentacene molecules is preserved, and their molecular orbitals can be directly imaged by STM. Formation of hybridized states of a gold atom and pentacene molecule were observed by STM on thin films [124].

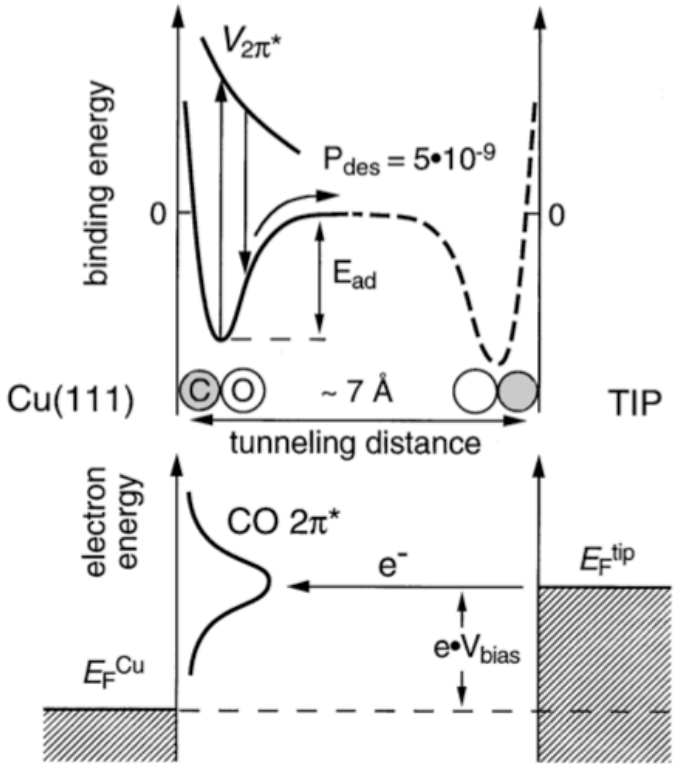

Figure 2.17. Top part: potential curve of the bound state of a CO molecule between the Cu(111) substrate (left) and the STM tip (right). A higher binding energy on the tip is assumed. Virtually no overlap between the two potential wells occurs. Additionally the assumed potential curve $V_{2\pi^*}$ of the excited state is shown. The desorption process according to the MGR model is indicated with arrows. It has a yield per excitation of $P_{des} = 5 \times 10^{-9}$. Bottom part: At positive sample bias V_{bias} tunnelling electrons from the STM tip (right) can transiently occupy states of the sample between E_F and eV_{bias}. Thus, at 2.4 bias the electrons start tunnelling into the 2π* state. Images and caption modified from [74].

Neutral Ag atoms were charged by an electron or a hole from an STM tip [126,127]. Multiple charge states of Ag atoms on NaCl films were identified as stable. It is also possible to use AFM to discriminate between charge states of atoms from noncontact mode [128].

Study of reversible switching atoms and molecules induced by STM is a fascinating field as it has applications for molecular electronics [131,132]. Most of the switches studied are bistable switches, because their two switching states are realized to be “ON” and “OFF” states

which can be used as simple logic device unit. STM can be used to change switch states of atom and molecules [121, 133-149]. Choi *et al.* [133] demonstrated electron-induced switching of azobenzene molecule on Au(111) by STM. Switching of azobenzene molecules was found to be *trans-cis* conformational changes as displayed in Fig 2.18. Conformational switching of azobenzene derivatives and other molecules induced by inelastic tunnelling electron [134-142] was also reported, for example, reversible and irreversible isomerisation of azobenezene molecules [134,135], four-step molecular switch of chlorophyll-a molecules [137], and chiral switch of propene molecules [138]. Adsorption switch can be seen in movement of atoms and molecules switches between two adsorption sites [121, 143-149] either lateral adsorption switches [143-146], e.g. hydrogen atom switching on Si(100)-2×1 [143,144] or vertical adsorption switches [121,148], e.g. Xe atom transferring between surface and tip [121]. STM is also employed to control the switching of charge states and conductance of molecule in STM junction [149].

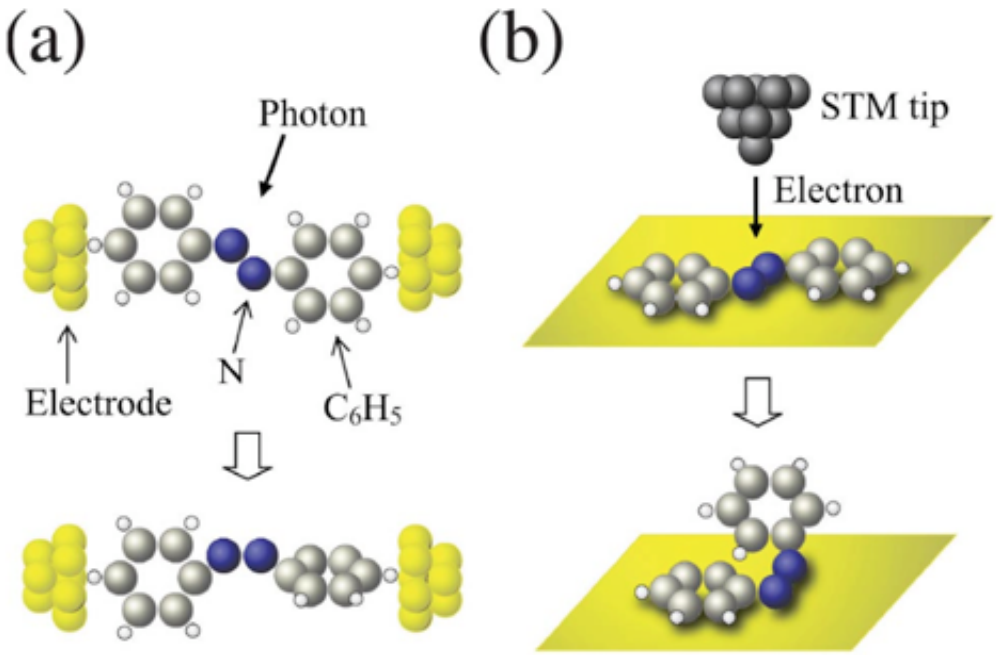

Figure 2.18. (a) A schematic of a light-driven molecular switch based on the conformational change of an azobenzene (AB) molecule in contact with two metallic electrodes. (b) A concept of electron-induced isomerisation of an AB molecule adsorbed onto a metallic surface with a scanning tunnneling microscope. Images and caption modified from ref. [133].

2.2.4 Combination of various manipulations

In some systems, there is more than one particular mechanism involved in manipulation. For example, the direction of hopping of a CH_3 molecule on Cu(111) by electrons injection from a STM tip depends on an off-centre position of the tip from the molecule and the polarity of the tip [150]. Hopping rate measurements suggest vibrational excitation processes inducing molecule translation. An inhomogeneous electric field in the STM junction was proposed as having a role in determining the hopping direction. As a CH_3 adsorbed molecule on a Cu(111) surface has a negative charge, applying a negative bias to the tip results in repulsive hopping whereas a positive bias on the tip induces attractive hopping (Fig. 2.19). By setting the electron energy and the position of the tip for injection, the direction of molecule hopping can be controlled. Nanostructures can be built up, molecule-by-molecule, from combination of two mechanisms equivalent to lateral manipulation.

Joachim and colleagues [151-153] used STM vertical and lateral manipulation to control the orientation of a selected single leg of a large molecule, Cu-tetra-3,5 *di-ter-butyl-phenyl porphyrin* (Cu-TBPP) (see Fig 2.20). There are two possible orientations of the leg, i.e. flat and non-flat to the plane of the porphyrin. Therefore, the leg swapping between these two states realises a molecular switch. Methods to measure internal conformation changes inside the molecule during manipulation were also developed [154] by recording the tunnelling currents at constant height mode of manipulation. Characteristic changes in current intensities reflect the movement mechanism of a molecule leg. Another larger molecule, called the Lander molecule, which is a molecular wire attached with four legs, was used to study conformation change and electronic interaction with copper atomic wire [155,156].

Manipulation with STM makes possible full chemical reaction synthesis at the single molecular level. Hla *et al*. [157] demonstrated the remarkable achievement of all the steps of the Ullmann reaction from two iodobenzene molecules on a Cu(111) surface (see Fig. 2.20 (a)). Initially, tunnelling electrons induce iodine atoms to split off from the iodobenzene parent molecules (b). One of the dissociated iodine atom is then transferred to the tip apex (c) making better contrast of images. This iodine functionalized tip was used to move the benzene radicals

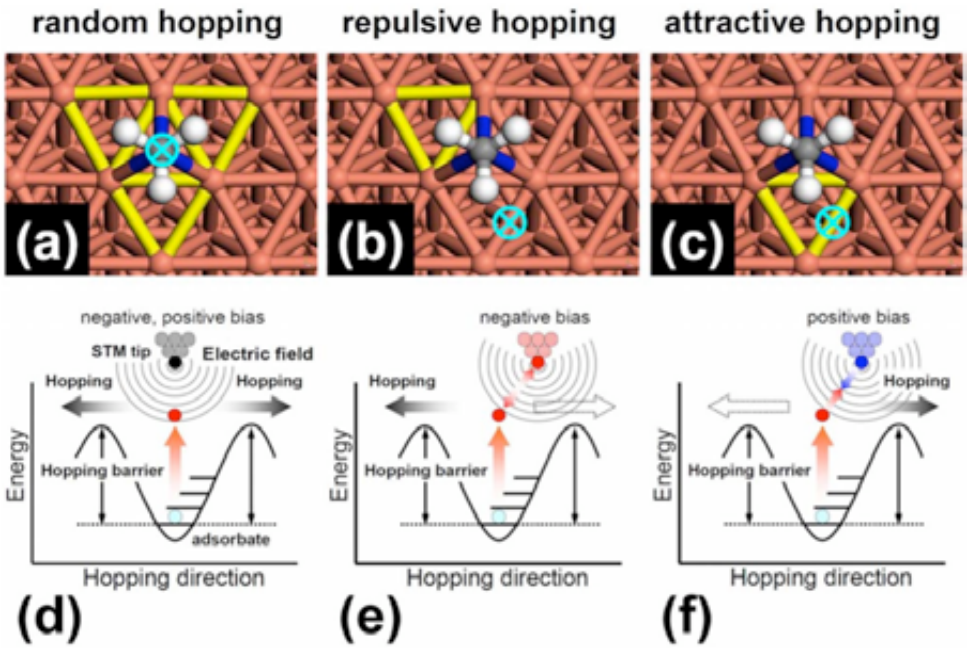

Figure 2.19. Top views of the relative position between the hopping direction(s) and the STM tip in (a) random, (b) repulsive, and (c) attractive hopping motions. The molecule hops toward the hollow sites, marked by yellow lines, when the tunnelling electrons are injected (or extracted) at the positions indicated by ⊗. Schematics for (d) random, (e) repulsive, and (f) attractive hopping. Each electric field contour is depicted with a point charge at the STM tip apex. Images and caption modified from [150]

toward each other (d) by lateral manipulation. When the radicals are close, tunnelling electrons were used to form a new C-C bond between the two radicals (e). The new synthesized biphenyl molecule was pulled along the step edge by lateral manipulation to prove bond formation (f). Finally, the iodine atom was transferred back to the surface (g). The C-C bond formation may be because vibrational excitation of the two benzene radicals leads to the rotation of the phenyl radicals in the right orientation to connect the two open bonds of each radical.

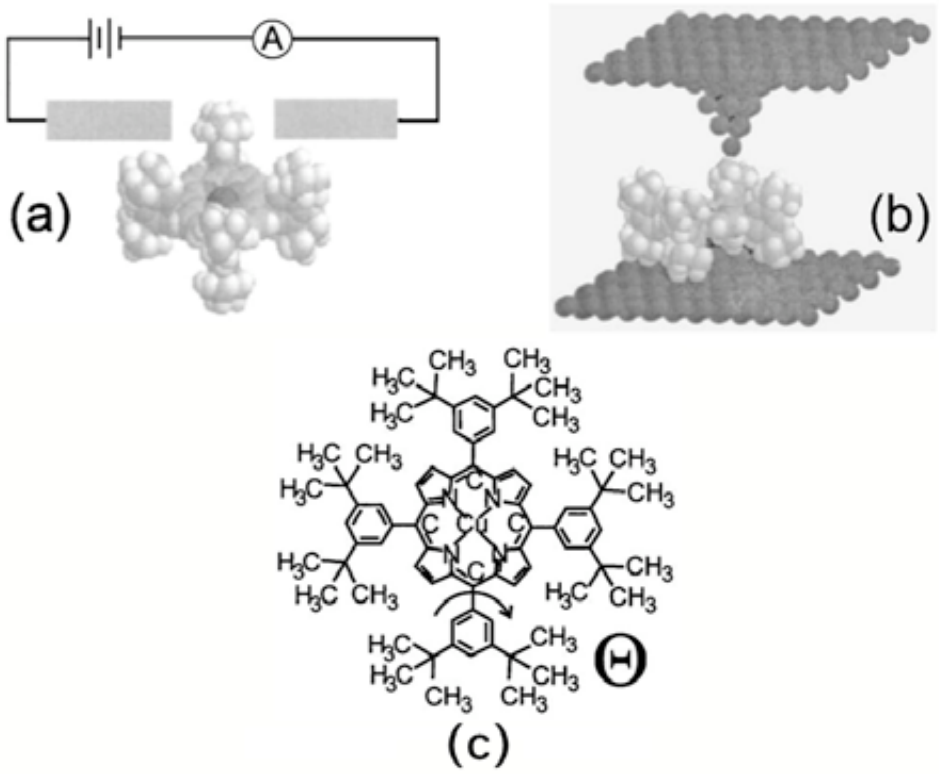

Figure 2.20. (a) Planar tunnelling junction equipped with a single Cu TBPP molecule modelling a molecular switch. The tunnelling current passes through only one leg, and the resistance R of the junction depends on the leg conformation. (b) Experimentally realized STM junction implementation of this molecular switch. (c) Chemical structure of Cu TBPP molecule. Images and caption modified from [151].

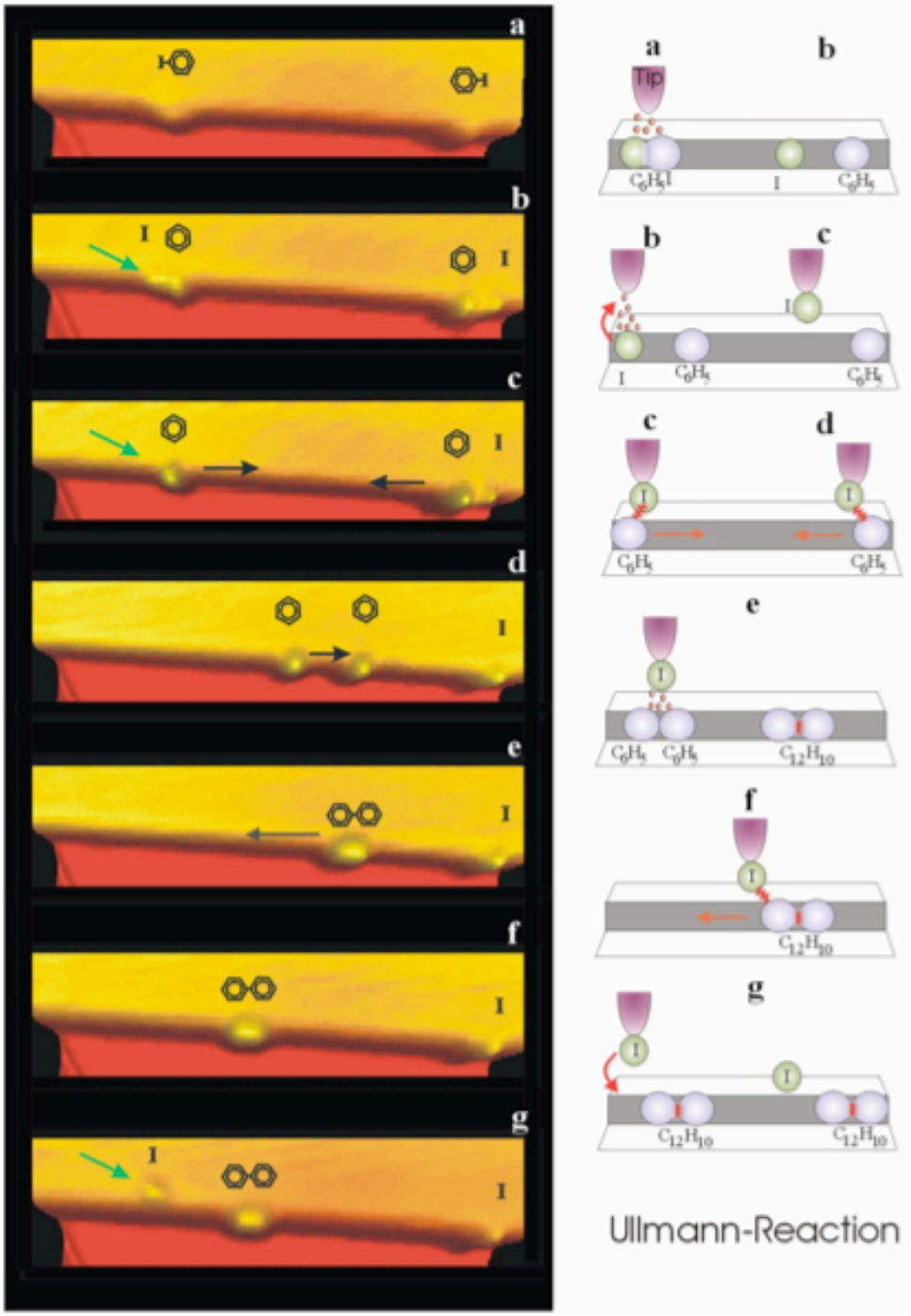

Figure 2.20. Sequence of steps in STM-tip induced single molecule Ullmann reaction on Cu(111). All reaction steps including dissociation of parent iodobenzene molecules, motion of phenyl reactants and iodine byproducts as well as association of phenyl reactants to biphenyl have been induced with the functionalized tip. Images and caption modified from [158].

2.3 Summary

Quantum tunnelling in STM and its principle in imaging at atomic level was described. Three manipulation types of atoms and molecules by STM were presented. These utilize mechanical forces, electric field and tunnelling electrons to interact with adsorbates localized in STM junctions. Mechanical manipulation is employed to create atomic structures which quantum characters, e.g. electronic quantum waves, can be observed. Molecular dynamics outcomes from STM manipulation, such as desorption, dissociation, switching, were shown. For larger molecules and more sophisticated operations, more than one type of manipulation may be needed. Advances in atomic and molecular manipulation make the possibility of nanotechnology, e.g. molecular electronics, nanomachine, and approaching to practical reality.

Chapter 3
Experimental methods

Single molecule STM experiments require ultra high vacuum (UHV) pressure (10^{-11} to 10^{-10} Torr). This chapter describes the configuration of the UHV chambers, pumps and gauges and their essential operations to provide the UHV pressure. The STM used in this thesis is a high thermal stability Besocke-type STM which is suitable for experiments at room temperature and above room temperature in my thesis. The mechanical vibration isolation and the electrical isolation were applied to achieve the greatest possible stability of the STM. The description of the STM and isolation systems are explained. Tip and silicon preparation are presented in detail, including the methods for dosing the chlorobenzene and PCB molecules. At the end of this chapter, the procedures of computer program written by Dr. Peter A. Sloan for analysing are given.

3.1 UHV chamber

3.1.1 Main chamber and preparation chamber

The UHV chamber has two principal sections, the STM chamber and the preparation chamber in which the molecules are dosed. Fig. 3.1 shows a schematic diagram of the UHV chamber system and Fig. 3.2 shows a photograph of the STM chamber, preparation chamber, load-lock and gas line for dosing. The STM chamber and preparation chamber are separated by a main gate valve (V1), which is usually closed to isolate the STM chamber from any

contamination from the preparation chamber. Both chambers have ion pumps (IP) and ion gauges (IG) to monitor the pressure in the chambers. To ensure the best vacuum condition for the STM chamber, our larger ion pump (Varian Diode 300), which is used for the STM chamber, includes a titanium sublimation pump (TSP) insert. The TSP utilizes sublimated Titanium from the filament to form a fresh Ti film which reacts with mainly active gases, e.g. N_2, O_2, H_2. A smaller IP, Varian Diode 150, is employed for the preparation chamber. These IP and TSP can maintain the STM chamber pressure to 10^{-11} torr and the preparation chamber pressure in the 10^{-10} Torr range. There is a transfer arm attached to the preparation chamber to transfer samples and tips to the STM chamber, which can store up to six tips and samples. The preparation chamber contains a quadrupolar mass spectrometer (MS) to examine gas molecule components, where chemical molecules introduced via leak-valve were ionized and measured mass-to-charge ratios through quadrupole mass-selective filter. The main turbo molecular pump (TMP, Pfeiffer, pumping speed 210 l/s) is also connected to the preparation chamber, which is used when baking the whole UHV system. Two leak valves are attached to the main chamber to introduce molecules to substrates and to the preparation chamber to examine molecular components via mass spectrosmetry.

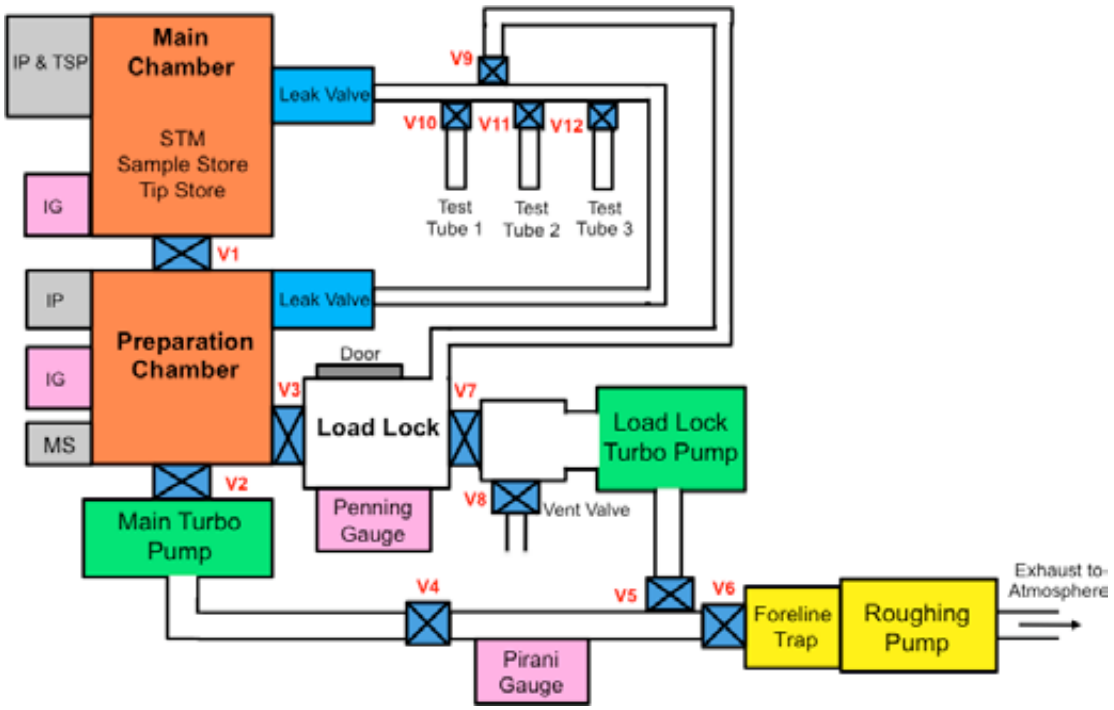

Figure 3.1. Schematic diagram showing UHV chambers and other equipment. V = valve.

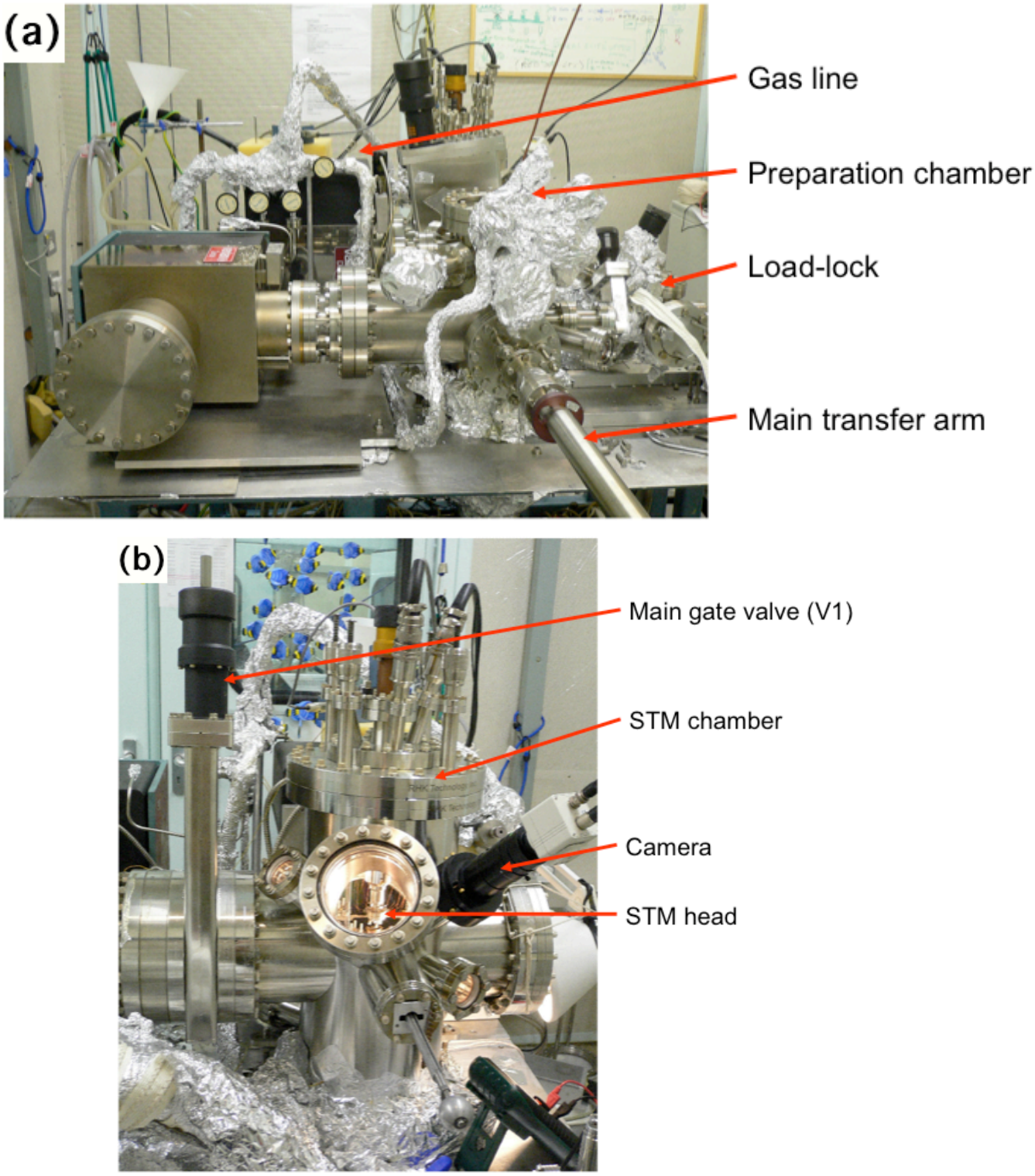

Figure 3.2. UHV-STM system. (a) Preparation chamber, load-lock and gas line. (b) Main chamber in which STM is placed.

3.1.2 Load-lock

The preparation chamber connects to a load-lock where tips and samples can be loaded. A valve (V3) separates these two sections. This valve is normally closed to isolate the preparation chamber from the load-lock and is only opened during the transfer of tips or samples. To protect the pressure of the preparation chamber the pressure in the load-lock has to be 10^{-7} or lower before the V3 valve is opened. This high vacuum pressure in the load-lock is generated by a TMP (Pfeiffer, pumping speed 56 l/s). The load-lock is also connected to the gas line via the V9 valve, so the gas line can be pumped by the load-lock TMP. V7 does not have a particular role in the load-lock and is only used when the effusion cell is attached.

3.1.3 Gas line

The gas line has an important role in the gas dosing process. Up to three test tubes of liquid sample can be attached to the gas line each with its own valves (V10-V12). The gas line is connected to two leak valves, one attached to the main chamber, the other to the preparation chamber. A computer controlled stepper motor is used to finely control the main chamber leak valve for precise molecular coverage of the sample. The LabVIEW computer program was written by Dr. Peter A. Sloan. The stepper motor also produces less vibrations than manual handling which allows, if required, dosing while imaging.

3.2 UHV operation

3.2.1 Venting

The chamber is vented via the vent valve (V8) on the load-lock to the preparation chamber and STM chamber. If venting is required, the UHV equipment that is not allowed to operate at atmospheric pressure, e.g. IPs and IGs, has to be turned off. In the case of venting the

preparation chamber, it needs to vent through the load-lock. Therefore, the V3 valve has to be opened. If the load-lock is not pumped, pumping the load-lock to high vacuum is required before opening the V3 valve. Similarly, to vent the main chamber, the V1 and V3 valves have to be opened. To vent the gas line, V9 has to be opened. Then, the V5 and V6 valve have to be shut before turning off the roughing pump and the load-lock TMP. Once the turbine speed of the TMP has been reduced to around half of its full operating speed (typically taking ~10 minutes or by listening to the sound of the turbine), the V8 valve can be opened very slowly, allowing a liquid nitrogen reservoir attached to this valve to introduce nitrogen gas to the UHV chamber. It is essential to open this valve very slowly as exposing the TMP to atmospheric pressure too fast can reduce the life-time of the TMP. A nitrogen layer on the chamber surface can protect the chamber from ambient contamination or adsorption, for example, of water. Venting the main TMP can be done in a similar fashion, however this uses air to vent instead of N_2 gas. After venting, all valves have to be closed to prevent any further contamination.

3.2.2 Pumping

To recover UHV pressure after venting, the chamber has to be pumped down and baked. All valves are closed before pumping, except the V2, V1, V3 and V7 valves, which connect the main chamber, preparation chamber and the load-lock together. Initially, the roughing pump is turned on and the V6 valve opened to pump the roughing line. When the pressure monitored by the Pirani gauge in the roughing line drops below 1×10^{-1} Torr, V5 and V4 can be opened. Pressure in the roughing line will increase to atmospheric pressure since the higher pressure from the chambers and the load-lock diffuses to the roughing line. Once the pressure drops to 1×10^{-1} Torr again, both TMPs can be started. It takes several hours to pump down both chambers to 10^{-7} Torr range. The penning gauge in the load-lock is used to monitor pressure in the chambers during this period. Once the pressure reaches 10^{-7}-10^{-6} Torr, the IG in the preparation and main chambers can be turned on. To turn on the IP, the pressure in the preparation and main chambers needs to be 10^{-8} Torr, which usually requires overnight pumping.

3.2.3 Baking

The pressure in the main and preparation chambers even after pumping will remain at ~ 10^{-9} to 10^{-8} Torr. Contaminants from the ambient environment, especially water molecules, stick inside the chamber. Thus to reach UHV, all the chambers must be baked above 100 °C to desorb water and other contaminant molecules. The maximum temperature allowed is no higher than the depolarization temperature of the piezoelectric tubes in the STM (maximum at 125 °C). It is important to prepare the chambers and the space inside the baking shields since it is not possible to make changes during baking. The metal table on which all chambers are located has to be free of paper and other combustible items. All glass windows on the viewports and UHV feedthroughs, such as the STM connections, have to be covered with aluminium foil to minimize the temperature gradients during baking. Any connections and components not designed for baking such as the stepper motor and anything containing plastic have to be detached. Both leak valves should be slightly opened as the metal components expand during baking. The test tubes have to be removed from the gas line. The STM stage has to be in the highest position and the sample holder has to be moved from the STM stage. The entire chamber is covered with shields. The shields' role is to block heat during baking. Heat for baking is generated from two sources: First, lamps are embedded on the wall shields for radiative heating. Second, heating tapes are attached to a specific location in the chamber. The locations of the heating tapes and corresponding power supply channel are shown in Table 3.1. The amount of power supplied to each heating tape can be adjusted during baking. The temperature of the chambers is measured by four nickel-chromium thermocouples attached to the chambers, as shown in Table 3.2. Temperatures during baking are monitored and recorded using a home-made LabVIEW computer program written by Dr. Peter A. Sloan. This program controls the power supply and smoothly raises the temperature from room temperature to the setpoint temperature (125 °C) and then keeps this setpoint for 48 hours (or more) before the baking process is halted. After a cooling period (taking ~1 day), the pressure usually reaches 10^{-10} Torr in the main and preparation chambers. The valves between chambers, i.e. V1-V3, can be shut to isolate each chamber. The TSP in the main chamber can be cooled by filling with liquid nitrogen and then the titanium filament is flashed to produce a thin film of clean titanium on the chamber wall. These titanium

films are very reactive to gas molecules inside the chamber. This should result in a pressure in the main chamber of 10^{-11} Torr.

Heating tape channel	Location
1	Gas-line (leak valve on preparation chamber)
2	Load-lock
3	Gas-line
4	Gas-line (leak valve on STM chamber)
5	STM chamber base
6	Main TMP
7	Preparation chamber base
8	Main transfer arm

Table 3.1 Location of heating tape corresponding to power supply channel.

Thermocouples	Location
1	STM top
2	STM base
3	STM/Prep gate valve
4	Prep base

Table 3.2 Location of thermocouples in chambers.

3.2.4 Leak detection methods

To maintain UHV conditions the vacuum system should be tightly sealed. Leaks will usually be caused by incorrect positioning or the absence of a copper gasket in a flange joint, a joint that has not been tightened, a broken feedthrough, or a ruptured bellows. Such a leak can be simply detected by splashing isopropanol over the vacuum joints and monitoring pressure changes. Another way to detect small leaks is to employ a He mass spectrometer. He is introduced to a suspected joint and the leak can be located by observing the helium peak at mass 4.

3.2.5 Transfer system and sample holder

The transfer system consists of a long transfer arm with a fork that fits into grooves on a specially designed sample holder. This transfer arm moves the sample from the main chamber to the preparation chamber and vice versa. The sample holder is shown in Fig. 3.3 (a). There is also another type of sample holder designed to measure the temperature in the main chamber. The top piece of the holder has helical ramps that are used for the coarse approach. There are also two grooves on the sample body that allow the sample to be transferred throughout the apparatus using forks. Fig. 3.3 (b) displays the tip transfer holder with the tip holder mounted on the central hole. It is identical to that used for sample transfer. There are three rods that can be inserted into the holes on the STM head. These guide the tip holder to the tip socket on the central scanning tube. The tip holder has to be very precisely aligned to the tip socket on the STM head, otherwise damage may occur to the central tube during the tip transfer step. A new tip with a diameter of 0.20-0.25 mm is mounted onto the tip holder which is placed onto the tip transfer holder. The sample holder and tip transfer holder both have a U-shaped bottom, which is specifically designed to fit into the sample stage as shown in Fig. 3.3 (d). The role of the wire outside the sample holder is to make contact with metal clips on the sample stage, which in turn is connected to the feedthrough. This is used to apply current through the wire to heat the sample.

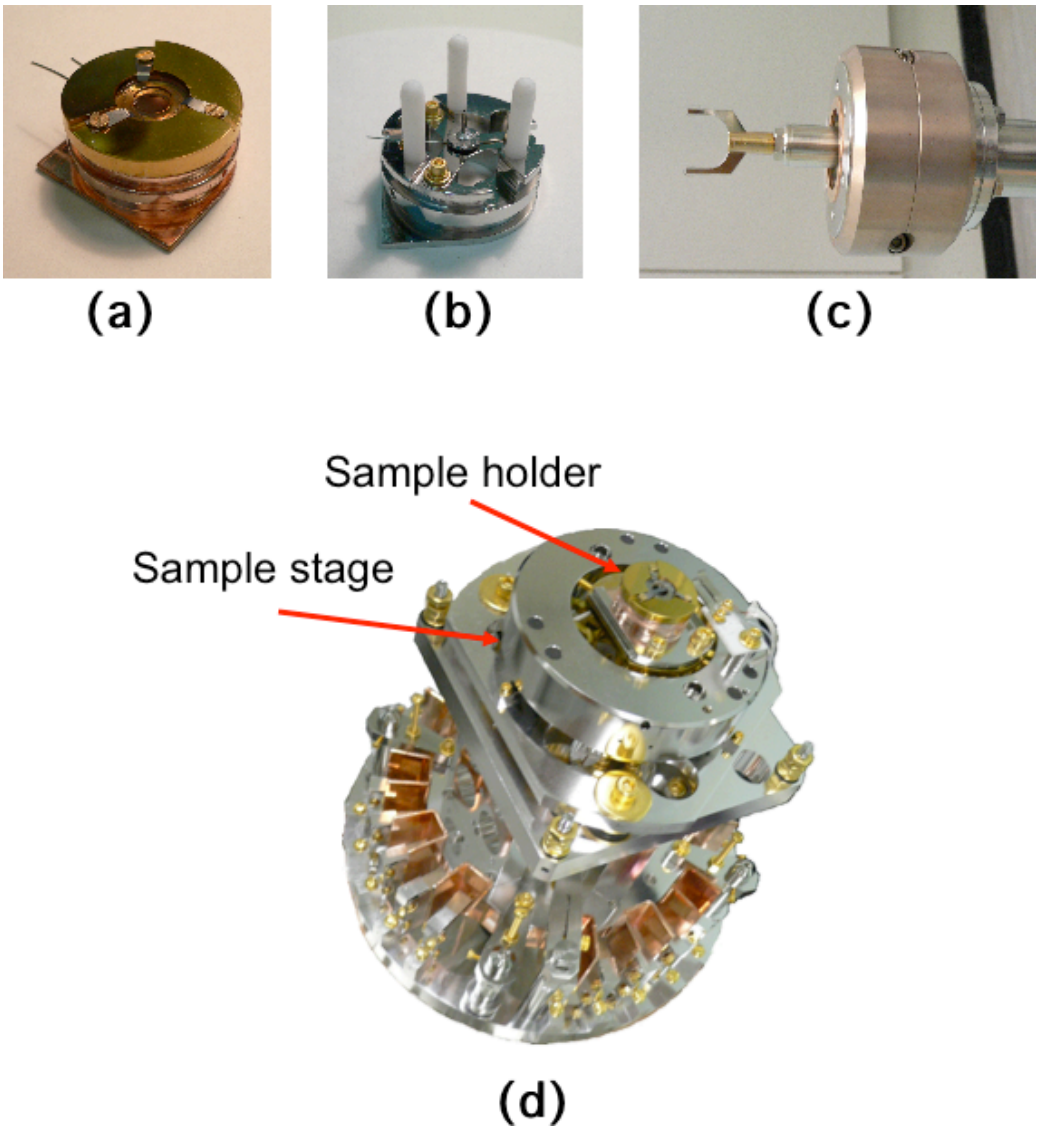

Figure 3.3. (a) Sample holder. (b) Tip transfer holder with the tip holder in the central hole. (c) Fork attached to the transfer arm. The fork is used to hold the sample holder or the tip transfer holder in the chambers. (d) Sample holder attached onto the top of the sample stage. The sample stage is isolated from external mechanical vibrations by an eddy-current damper, stacked plate and springs.

3.3 Scanning tunnelling microscope

3.3.1 Description

The scanning tunnelling microscope used is a commercially available "Besocke-", "Beetle-" or "Walker-" type STM (RHK 400) [159,160]. The scan head contains four identical piezoelectric tubes. The three outer piezoelectric tubes are used for coarse movement and a fourth central tube is used for scanning. This central scan piezo holds the tip. The outer tubes have sapphire balls attached to the ends that rest on the three helical ramps of the sample holder, and each ramp has a height of 0.75 mm (Fig. 3.4 (a)). The coarse approach consists of the head walking down the ramps until the tip, which is mounted on the central piezo, is within tunnelling range. Then the central scan piezo is used to position the tip in the lateral X-Y directions (maximum scanning area ~ 6×6 μm^2 range in this work).

The Besocke-type STM allows highly stable operation of the tunnelling gap [159,160]. This design has a smaller mechanical loop than the typical STM, i.e. the tripod scanner, since the scanning head has a smaller size and only thin copper wires are connected to the scanning head (Fig. 3.4 (b)). The Besocke-type STM has high frequency resonance, allowing high speed scanning with a lower noise level. Since all three piezoelectric tubes are identical and the scan head has a symmetrical arrangement, the thermal drifts are largely compensated on all axes, resulting in minimum thermal drifts. These types of STM are powerful tools for performing atomic manipulation experiments at room temperature or above.

All four piezoelectric tubes are single tube scanners that can be moved in three directions, X-Y-Z. The outer electrode of the piezo tubes is divided lengthwise into four sections, as illustrated in Fig. 3.5 (a). The movement of the piezoelectric tubes in the X-Y plane is achieved by applying the opposite bias voltage between the opposite quadrants of the outside electrodes, i.e. a positive bias between one outer electrode and the inner one and a negative bias between the opposite outer electrode and the inner one. Movement in the Z direction is achieved by applying a voltage between the inner electrode and the four outer ones. A maximum voltage of about ±130

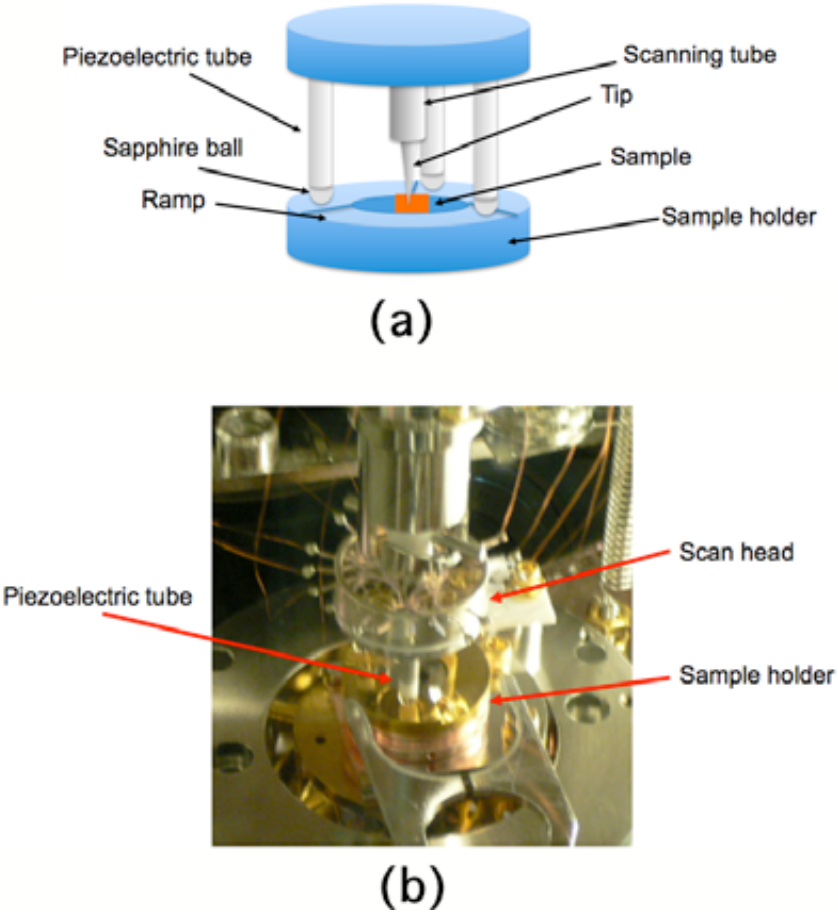

Figure 3.4. Besocke type STM. (a) A schematic representation of the STM head resting on the helical ramps of the sample holder; the components of the STM are also illustrated. (b) Inside view of the STM in the main chamber.

V can be applied. Fig. 3.5 (b) presents the "slip and stick" movement mechanism of the piezo tube. In the first step, the piezo leg is extended to push the head up. In the second step, it is bent and lowered. If this action is fast enough, the glass ball will move ("slip") to the lateral side, making the whole head displace in the desired direction. The direction of movement depends on how the tube bends.

The STM head is lowered onto the prepared sample by turning the manipulator. Once the legs of the STM head touch the sample ramps the STM head is lowered extremely carefully until

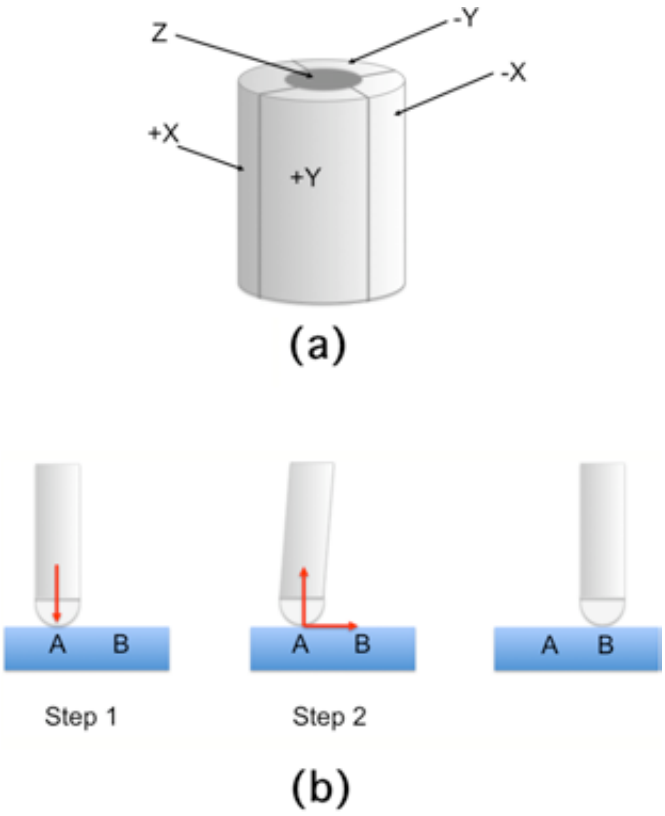

Figure 3.5. (A) Scanner tube consisting of four separate sections: the outside electrodes for movement in the X-Y direction and the inner electrode for movement in the Z direction. (B) Process of tube movement with slip and stick method from A to B. Red arrows show the extending/contracting direction of the tube and the side movement of the glass ball.

it is isolated from the manipulation. Then, the coarse approach can be started. Continuous motion of the STM head is controlled by the SPM 100 via the computer, where pulses of sawtooth type voltage are applied to each piezo leg. The position of the tip in the X-Y plane can be adjusted to avoid undesired areas, for instance, high corrugations or steps. The ideal surface is the flat area of the sample. The coarse approach is monitored via a camera on a window port. Once the tip is at the desired position (very close to the sample), an automatic tip approach can be started. Parameters for the automatic approach are set (normal use: bias voltage= +3 V, tunnelling current=100 pA, feedback gain=3). When the tip reaches the tunnelling range, the approach is stopped. The tunnelling current can be equal to the current setpoint. This tip approach procedure is crash-free.

3.3.2 Mechanical vibration isolation

The stability of the STM junction is very important for measuring the tunnelling current signal since it is sensitive to the distance between the tip and the sample (~10 Å). Therefore, the tunnelling gap needs to be isolated from external vibrations. To isolate the tunnelling gap from mechanical vibrations, a combination of several vibration damping systems is applied to minimize external noise [161]. All chambers and pumps are placed on a metal table on a ten-ton concrete block, which in turn is placed on floating supports, all of which are located in a sound-proof room. This isolates the UHV chambers from ground vibrations and acoustic noises. In the main chamber, the whole STM stage is suspended via springs such that it is separated from the chamber walls (Fig. 3.6 (a)). An eddy-current damper and stacked plate (indicated in Fig. 3.6 (b)) are used to reduce vibration of the sample stage. These isolation systems prevent high frequency vibrations (>50 Hz) coupling to the tunnelling junction. The Besocke-type STM is built on rigid metal components with a small mechanical loop. This special design has high frequency resonance characteristics preventing coupling with low frequency vibrations from outside. Combining all vibration dampers together ensures the minimal possible vibration for the STM operation.

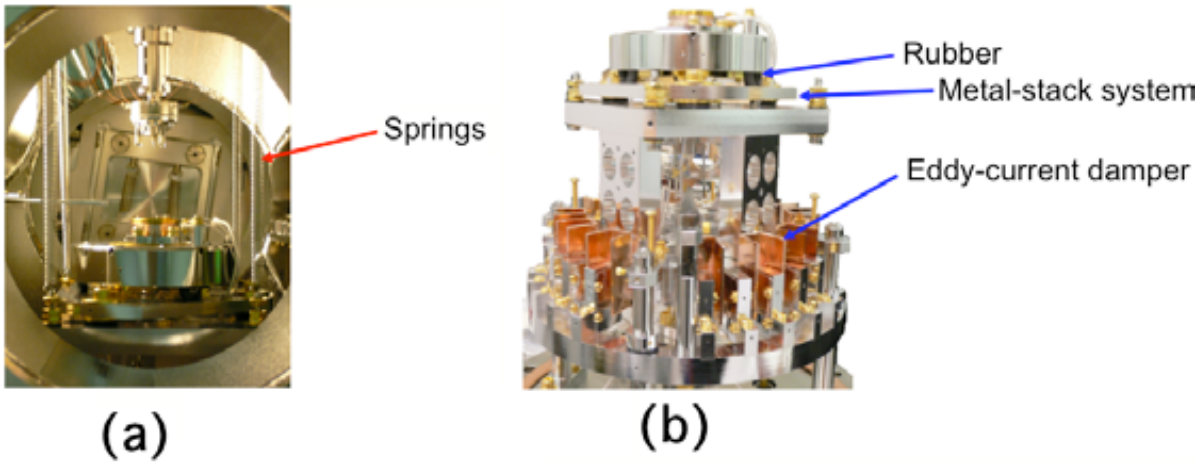

Fig. 3.6. Mechanical vibration isolation. (a) Suspension springs to prevent vibration of the whole STM stage. (b) Metal-stack system and eddy-current damper to avoid the vibration of the sample stage.

3.3.3 Ground loops

Ground loops created by sharing a common ground terminal in the electrical system of the apparatus are a major cause of noise [162]. For instance, in an UHV-STM apparatus, a ground loop can be generated if pumping units, power supplies and electronics are connected to the same electrical ground. In order to solve this problem an isolation transformer as illustrated in Fig. 3.7 is placed in the electrical circuit/system to avoid direct electrical connection between the different units (e.g., between the STM electric units and the pumping units). Moreover, the electrical ground cables wrapped around the electrical cables are used as shielding elements to protect the signal from noise generated by external electromagnetic waves.

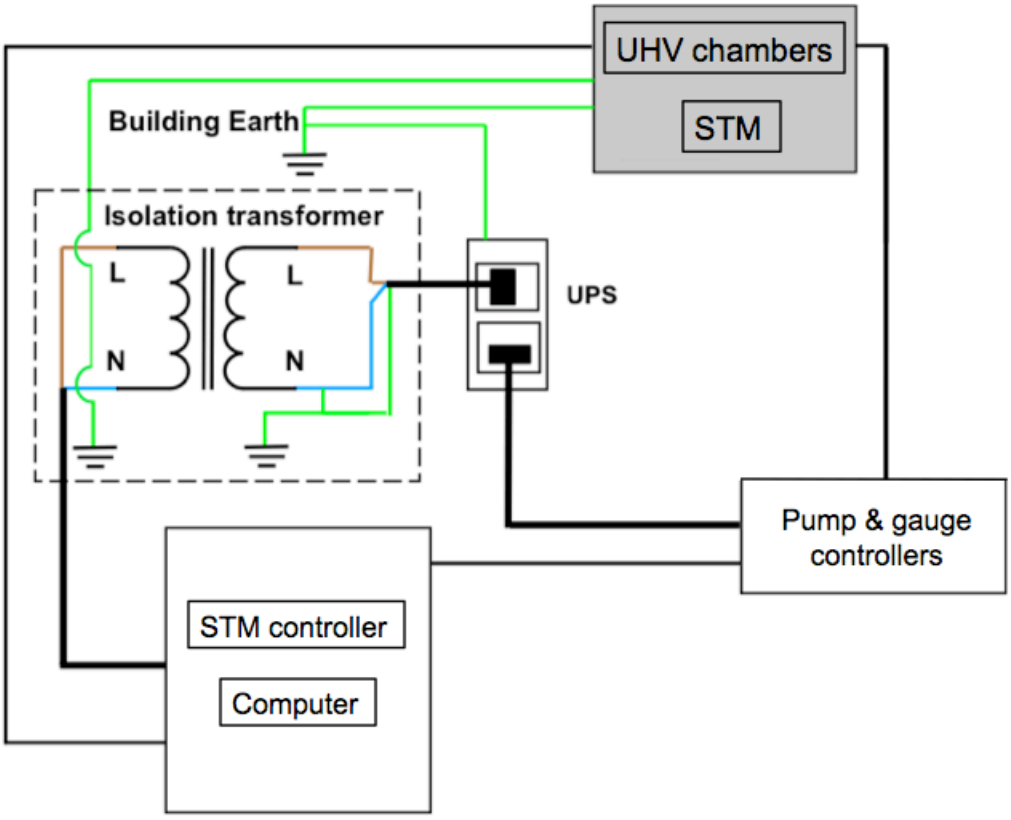

Figure 3.7. Simplified schematic of the electronic units and isolation transformer, used to break the ground loop. (UPS = uninterruptible power supply. FUNC GEN = function generator. L (N) is the live (neutral) electrical wire.)

3.4 Tip preparation

STM tips are typically prepared by mechanical cutting or electrochemical etching. The method and selection of material depend upon the objective. The first approach is simple and fast but the shape of the tip apex cannot be controlled. The mechanical cutting method does not produce an oxide layer, which is suitable for ambient environment experiments. The second method, however, produces better quality tips. Using this method, it is also possible to prepare tips in a controlled manner. Thus, the etching method is appropriate for use in UHV-STM studies.

3.4.1 Pt-Ir tips

Pt-Ir tips are usually prepared using the mechanical cutting method. In this method the first cut is made using pliers at 45° with respect to the Pt-Ir wire. It is important to apply the force parallel to the wire while pulling the pliers backwards. Then, the wire has to be rotated 90° before the second cutting step that is done 0.5-2 cm from the apex. The apex shape can be monitored under an optical microscope.

3.4.2 W tips

Tungsten tips are widely used for UHV-STM studies. These tips are prepared by electrochemical etching. This method is reproducible and the shape of the tip can be controlled by etching parameters. A good tip has to be sharp and symmetric with an apex radius of less than 100 nm in order to achieve atomic resolution imaging. Another important parameter is the tip aspect ratio, which is the ratio of the height (h) to the diameter (d) of the tip as shown in Fig. 3.8. Low-aspect ratio tips have fewer mechanical vibrations, and are therefore better for imaging.

The etching procedure is performed in a 2 M NaOH solution prepared 24 hours before the etching process. The tungsten wires used are of 99.95% purity, 0.25 nm diameter from

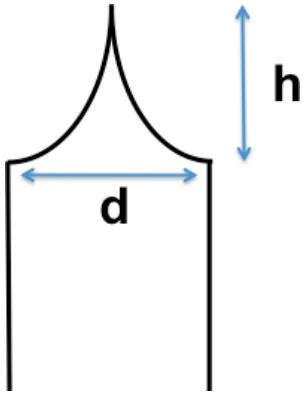

Figure 3.8. The aspect ratio of the tip is h/d, where h = height and d = diameter.

ADVENT. The tungsten (W) wire has to be cleaned with isopropanal/acetone solution for 10 minutes, then cleaned in an ultrasonic bath and finally, rinsed several times with distilled water. The electrochemical reaction is given by:

$$\text{Cathode: } 6H_2O + 6e^- \rightarrow 3H_2(g) + 6OH^-,$$

$$\text{Anode: } W(s) + 8OH^- \rightarrow WO_4^{2-} + 4H_2O + 6e^-,$$

$$\text{Overall: } W(s) + 2OH^- + 2H_2O \rightarrow WO_4^{2-} + 3H_2(g).$$

Based on the chemical reaction, the submerged tungsten wire acts as an anode, which preferentially corrodes. The interface between the W wire and the electrolyte creates a meniscus around the wire, which is important for defining the corrosion area and thus affects the final shape of the tip. The height of the meniscus has a remarkable effect on the final shape of the tip apex (i.e. aspect ratio), which can be changed by moving the wire into (away from) the air/electrolyte interface to stretch (shorten) the meniscus [163].

Fig. 3.9 shows a schematic view of the etching process. The negative electrode is a ring, 2-3 cm in diameter, made from gold wire. This gold ring is dipped by ~ 5 mm into 2 M aqueous NaOH. A length of tungsten wire (the positive electrode) is pushed through the centre of the ring and held in place there. The ring creates a symmetrical etching volume around the W wire. Cut tungsten wires generally have defects at the end. Therefore, a two-step etching process is

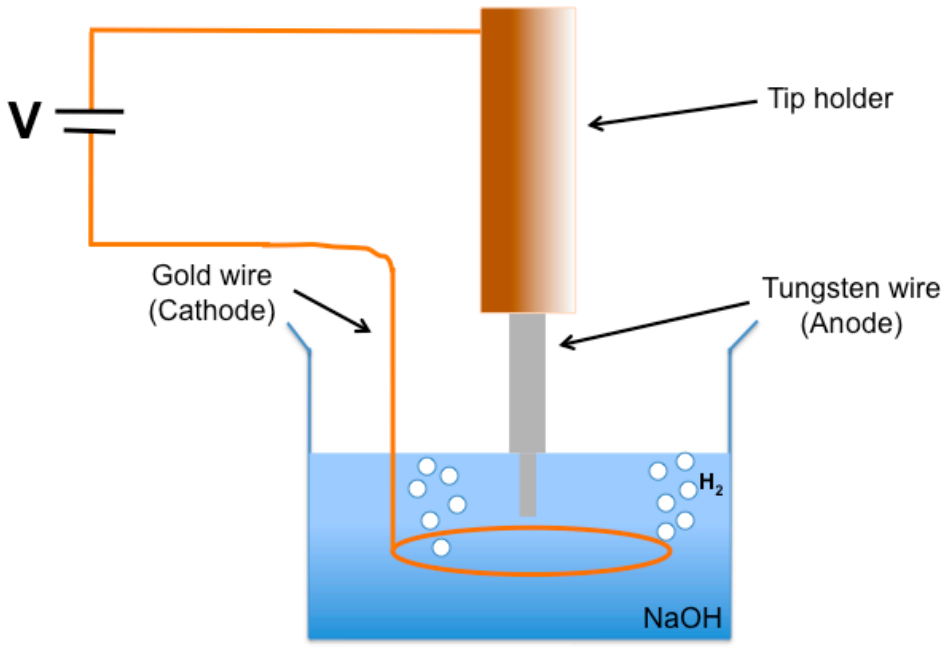

Figure 3.9. Etching process diagram. A gold ring was employed as the cathode and tungsten wire was used as the anode in an electrochemical cell. Hydrogen bubbles were generated around the ring during the etching process.

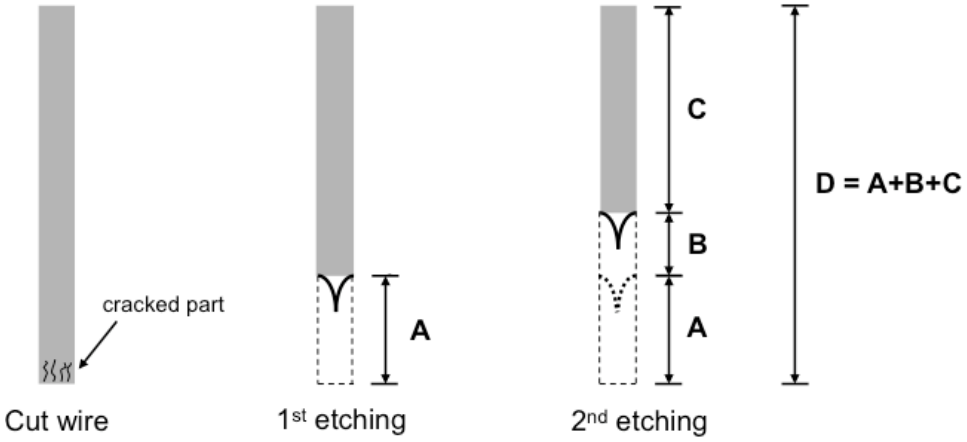

Figure 3.10. Cut tungsten wire with cracks at the cutting location. The first etching step removes these defects, A = 5 mm. The second etching step produces a sharp tip, B = 3 mm. The length of the cut wire (D) can be determined by selecting the final length of the etched wire (C).

conducted. The first step is to remove damaged parts of the cut wire and the second step is to etch a properly shaped tip, depicted in Fig. 3.10. The length submerged in each step is in the range of 3-5 mm. It has been reported that immersing 1–3 mm creates a sharp tip for wire with a diameter of 0.25 mm, whereas longer lengths cause bending of the tip [163,164] or "ball-shaped" features. The latter may be due to the melting of the wire by heat generated while the tungsten necks off. In contrast, immersion of 8 mm resulted in a sub-100 nm tip apex for wire with a diameter of 1.6 mm [164], whereas 1-2 mm immersion produced a tip apex of over 1 μm. In this work, two-step etching was conducted using tungsten wires with a diameter of 0.25 mm and an immersion length of 3 mm. The hydrogen bubbles generated during the reaction can cause disturbances on the surface around the tip, resulting in an undesirably shaped meniscus. However, the bubbles have an insignificant effect on the shape of the etched tip apex.

Fig. 3.11 (a)-(d) indicates the etching apparatus and the preparation steps. As mechanical vibration can disturb the shape of the meniscus, the whole etching process has to be performed on

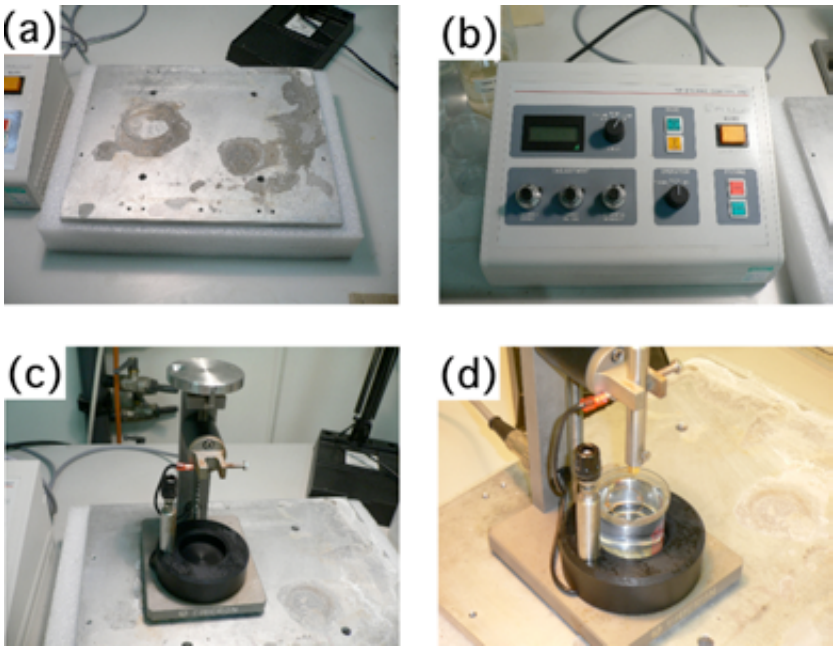

Figure 3.11. Apparatus for etching and preparation. (a) A soft foam block for vibration isolation. (b) and (c) Omicron controller unit and tip etching stage which allows fine control of the cutoff time and length of tip submerged in solution. (d) Complete setting for etching.

a soft foam block to hinder any external vibrations caused by the table and floor (Fig. 3.11 (a)). The cutoff time is a crucial factor determining the sharpness of the tip, with a shorter cutoff time giving a sharper tip [163]. Therefore, a DC etching apparatus from Omicron (illustrated in Fig. 3.11 (b) to (d)) operating with various cutoff modes was used to control the etching process. The whole process required to produce a tip takes about 20 minutes. The etched tips were usually characterized using an optical microscope and the sub-100 nm apex of the tip was measured by scanning electron microscope (SEM).

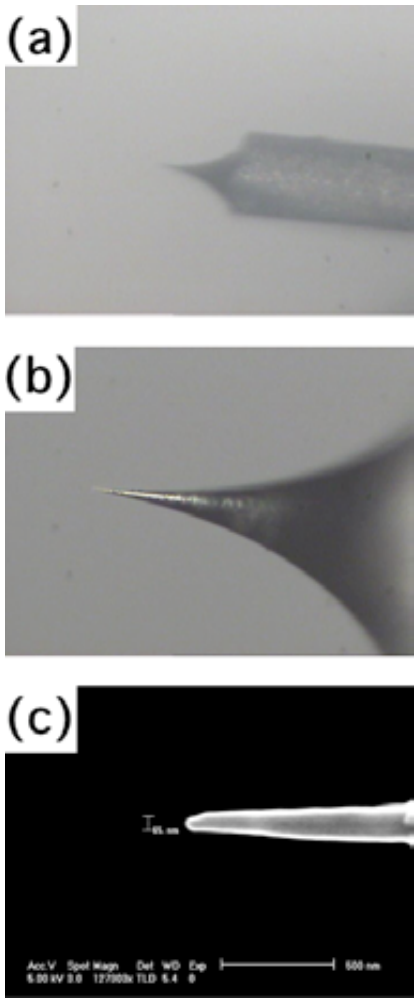

Figure 3.12. Etched tips viewed microscopically. Sharp tip apex observed under an optical microscope at a magnification of (a) 5× and (b) 20×. (c) The tip width of 65 nm was measured by SEM. All images are of the same tip.

3.4.3 Tip annealing

The one big disadvantage with etching techniques is the oxide layer formed on the W wire after the etching process. This oxide layer (tungsten trioxide) results in instability of the tunnelling condition and low resolution of the STM images. The rate of oxide growth post-etching is very fast, at around 10 Å per 20 seconds as shown in Fig. 3.13 [165]. To remove the tungsten trioxide, the tip was resistively heated at 1075 K under UHV conditions [166]. During

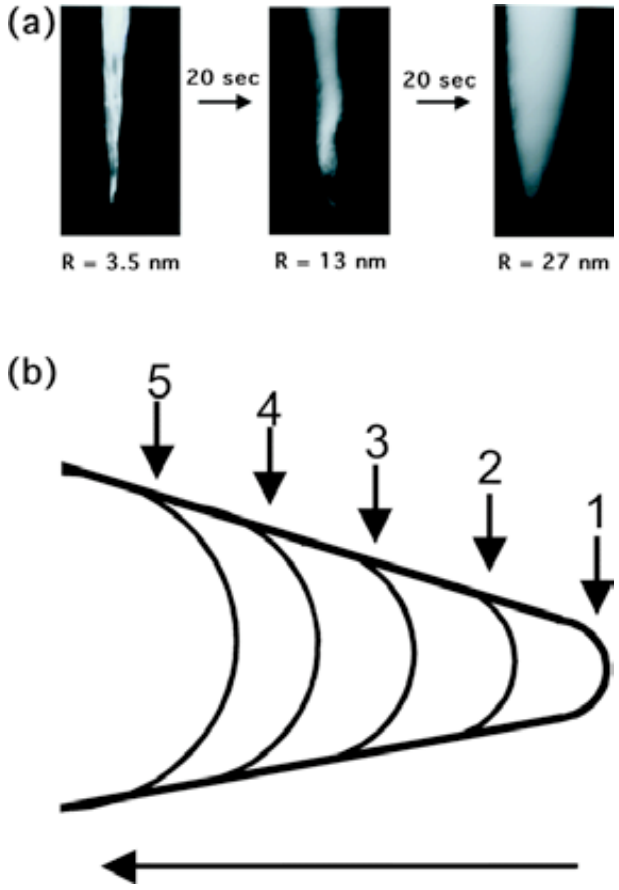

Figure 3.13. (a) A sharp tip, before and 20 and 40 s after the etching process. (b) Schematic of the tip blunting that occurs after etching. Position 1 corresponds to the etched tip with a tip radius of ~5 nm. Position 2 and 3 correspond to 10 and 20 s after the etching process, with a diameter of 5 and 10 nm respectively. Images and caption modified from ref. [165].

the heating process the tungsten trioxide reacts with tungsten to form tungsten dioxide, which will sublimate according to the following chemical reaction:

$$2WO_3 + W \rightarrow 3WO_2 \uparrow .$$

Fig. 3.14 is a schematic diagram of the resistive tip heating circuit. To make a circuit, a larger diameter tungsten wire (0.5 mm) is mounted onto a modified ion gauge and is connected near the top of the etched wire. During the heating process, current from a DC power supply is ramped until a bright orange colour (around 3-5 A) is observed. The W wire is then kept at this temperature (~1300 K) for 2 seconds. This first annealing step removes the oxide layer and repairs the crystallographic defects at the tip. Then, the current is turned down until the tip is a dark red colour and it is held in these conditions for 10 minutes to remove other remaining impurities. After degassing, the tip is cooled down for about 15 minutes, then the tip is mounted on the tip holder and transferred to the STM chamber.

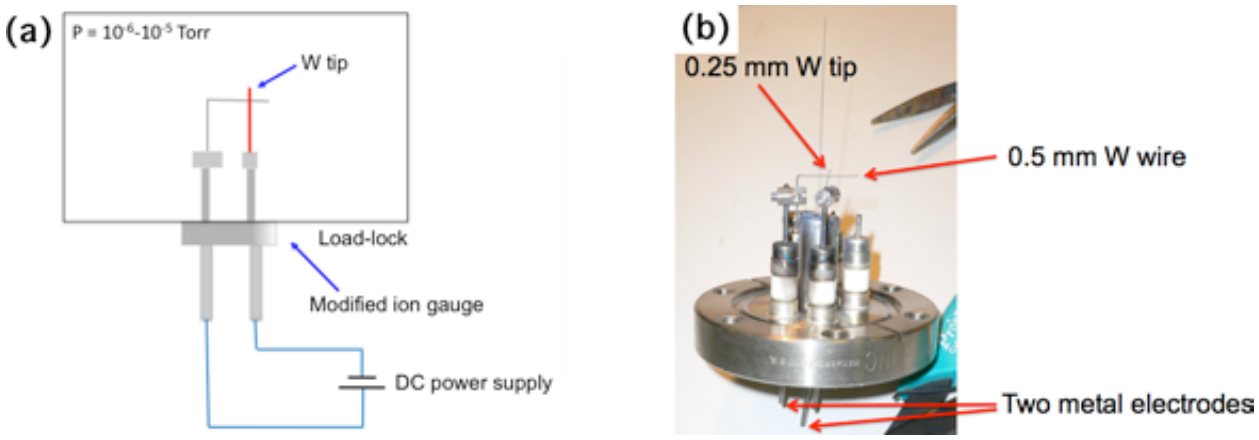

Figure 3.14. Tip annealing process operating in the load-lock. (a) Schematic diagram of the electrical circuit for heating the tip. (b) Tip and wire mounted on a modified ion gauge.

3.4.4 *In situ* tip modification

The condition of the STM tips may change during scanning, manipulating molecules or even when approaching the sample. This may be due to a change in tip shape, or the picking up of some molecules from the sample, leading to lower conductivity and blunting of the tip. These affect the quality of the scanning images, for example, by losing atomic resolution, and producing double images (i.e., superposition of images generated from two tips on the apex). *In situ* modification of the tip can be conducted by picking Si surface atoms from an Si(111)-7×7 surface with the tip end. This manipulation can be performed by applying pulses of –4 to –6 V to bias the clean silicon surface and thus extract silicon atoms by field ion emission [167-169]. Generally, this procedure improves the resolution of the image. Chemical interactions may be involved in silicon extraction, thus the decreasing of the tip-sample distance can enhance the adatom extraction from surfaces. If the tip shape is still not good enough, –8 to –10 V can be applied for 10 s to form a sharp needle tip [170]. Imaging of clean Si(111)-7×7 at bias voltages of +1 to +2 V and –1 to –2 V is normally used to check images after modification. Tip modification may need to be repeated for many cycles until the desired image quality is achieved. A new tip will be replaced if prolonged tip amendment does not improve the tip.

3.5 Sample preparation

3.5.1 Si(111)-7×7

The 2 mm × 9 mm Si(111) samples are cut from a phosphorus-dosed n-type silicon wafer with 99.999% purity and a thickness of 0.38 mm. Typically, the resistivity of cut silicon samples is 1-30 kΩ cm. The prepared samples are mounted onto the sample holder between two sapphire washers to isolate them from the body of the sample holder. Both ends of the samples must be placed on Tantalum plates, which have contacts to the sample holder body and wire extended outside the body. The contacts between the Ta plates and the samples have to be checked by

measuring the resistance between the body of the sample holder and the wire. Compressed N_2 gas is used to clean dust from the sample holder before transferring it to the load-lock.

These samples are transferred to the main UHV chamber for degassing at ~600 °C overnight to remove the oxide layers and other contamination by direct-current heating. Then, the sample temperature as a function of current is measured by a pyrometer with an emissivity of silicon of 0.65, and the temperature of the samples is allowed to increase up to 1250 °C. After this step, the sample temperature can be controlled with current from an external power supply. To create a Si(111)-7×7 surface, two flashing steps are required. First, the sample is flashed at 1250 °C for 20 seconds. The pressure in the main chamber increases as the sample becomes hotter. The pressure in the chamber should not rise above 1×10^{-8} Torr during flashing. This step can be repeated many times, especially for new samples. Then, a second flashing is followed by ramping the sample temperature to 1250 °C for 5 seconds; the temperature is then rapidly reduced to 960 °C and then cooled by 1 °C s^{-1} to room temperature. Fig. 3.15 shows a clean reconstructed Si(111)-7×7 surface, of 600 Å × 600 Å, with a small percentage of defects (less than 1%).

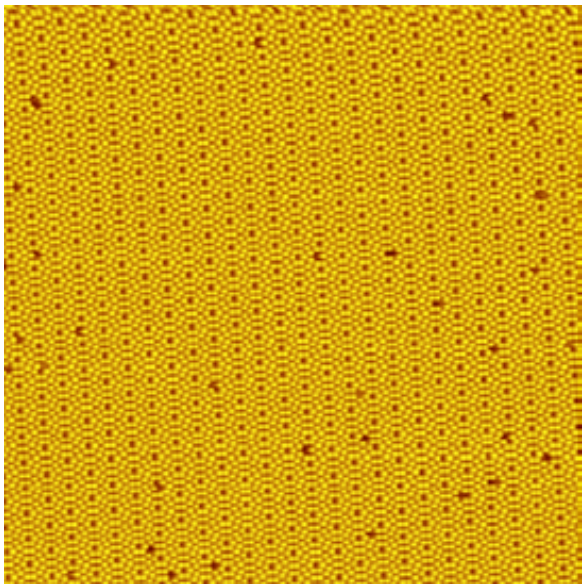

Figure 3.15. Reconstructed Si(111)-7×7 surface. The STM image was taken at +2 V, 100 pA, and is 600 Å × 600 Å in size.

3.5.2 Dosing of chlorobenzene

Liquid chlorobenzene is added to a test tube 1-2 cm from the bottom of the tube, which is then attached to the gas line (in Fig. 3.2 (a)). Before introducing chlorobenzene onto the silicon sample, chlorobenzene needs to be cleaned of contaminants from the ambient environment using the Freeze-Pump-Thaw procedure. Initially, the clean gas line must be pumped through the load-lock by turning on the roughing pump and the main turbo pump until the pressure in the load-lock is 10^{-7} to 10^{-6} Torr. When the pressure is less than 1×10^{-5} Torr, the valve between the load-lock and the gas line (V9) can be opened slowly until the pressure drops to the 1×10^{-5} Torr range. Then, the Freeze-Pump-Thaw procedure can be carried out. First, use liquid nitrogen to freeze liquid chlorobenzene to the solid form, causing other contaminant gas molecules to be trapped inside the frozen solvent as bubbles. When the solvent is frozen, the valve between the test tube and the gas line (V10, V11 or V12) can be opened slowly to pump undesired gas from the test tube. This valve can be closed when the pressure drops to the high vacuum level to prevent losing chlorobenzene molecules from the test tube, since it evaporates faster at this low pressure. Then, a water bath at room temperature is used to thaw the frozen solvent until it completely melts to liquid. The release of gas bubbles can be observed as unwanted gases, such as nitrogen, oxygen, carbon monoxide, carbon dioxide and others, are extracted from the solvent, which will be pumped from the test tube in the next Freeze-Pump-Thaw cycle. This procedure should be repeated until no further release of gas is seen as the solution thaws. The purity of the chlorobenzene solvent should be checked using the mass spectroscope in the preparation chamber. This can be done by introducing chlorobenzene from the test tube to the gas line and the preparation chamber via the leak valve. The peaks from the mass spectra show the chlorobenzene signature and other light molecule gases, i.e. hydrogen and helium. Purified chlorobenzene molecules are pumped to the gas line by opening the valve between the test tube and the gas line for a certain time, since the gas line has a pressure equivalent to the load-lock, ~ 10^{-6}-10^{-5} Torr and the vapour pressure of the solvent is quite high (~15 Torr). The molecules in the gas line are exposed to the sample in the main chamber via a leak valve governed by a step motor, in turn controlled by a computer program. Exposures are calculated in Langmuir (L), such

that 1 L is 1×10^{-6} Torr · s, and the sticking coefficient is one. The maximum pressure during dosing is typically limited to 8×10^{-10} Torr to avoid contaminating the main chamber.

3.5.3 Dosing of polychlorinated biphenyl

The solid powder of 4,4′-polychlorinated biphenyl (4,4′-PCB) used for experiments in chapter 6 has a vapour pressure of 10^{-12}-10^{-4} atm at 25 °C [171]. To dose these solid phase molecules, the dosing process requires heating to enhance their vapour pressure. The Near Ambient Temperature effusion Cell (NATC) in Fig. 3.16 (a) is used to heat the organic substrate to 350 °C. It provides accurate temperature regulation via thermal fluid oil with a compatible control thermostat CCx-304B vpc. Silicone oil is used as the thermal medium and is heated in a bath inside the thermostat and pumped through the effusion cell. The thermostat controls the temperature of the oil in the bath, which in turn regulates the temperature of the effusion cell.

PCB substrates are deposited inside the glass cell tube of the effusion cell (Fig. 3.16 (b)). Then, the effusion cell is attached to the load-lock located in the green rectangle in Fig. 3.16 (c), to which the shorter transfer arm is attached. It is crucial to locate the heating-exit of the cell in the upper position as shown in Fig. 3.16 (d). The thermally isolated hoses are arranged and connected to the cell with a sealing plug. The effusion cell and the load-lock have to be baked so that they outgas once before dosing. Since the molecules in the cell evaporate and are pumped to the outside through the exhaust line, this causes the loss of molecules from the cell. To minimize this loss, the cell temperature is kept at 70-90 °C during outgassing, compared to the normal baking temperature of the load-lock of 90-120 °C and the total time of baking is limited to 2-3 hours. This outgassing process also makes the PCB substrates more pure since the substrates were in the ambient environment before being deposited. The pressure at the load-lock is monitored during baking. After the baking process has finished, the load-lock and the cell are allowed to cool down. The decrease in the pressure of the load-lock is expected to be 10^{-7}-10^{-6} Torr. PCB molecules are still pumped from the system at room temperature at a lower rate than during baking. Venting the load-lock halts the pumping of PCB molecules out of the cell. After finishing this procedure, the clean PCB molecules are prepared to dose for experiments.

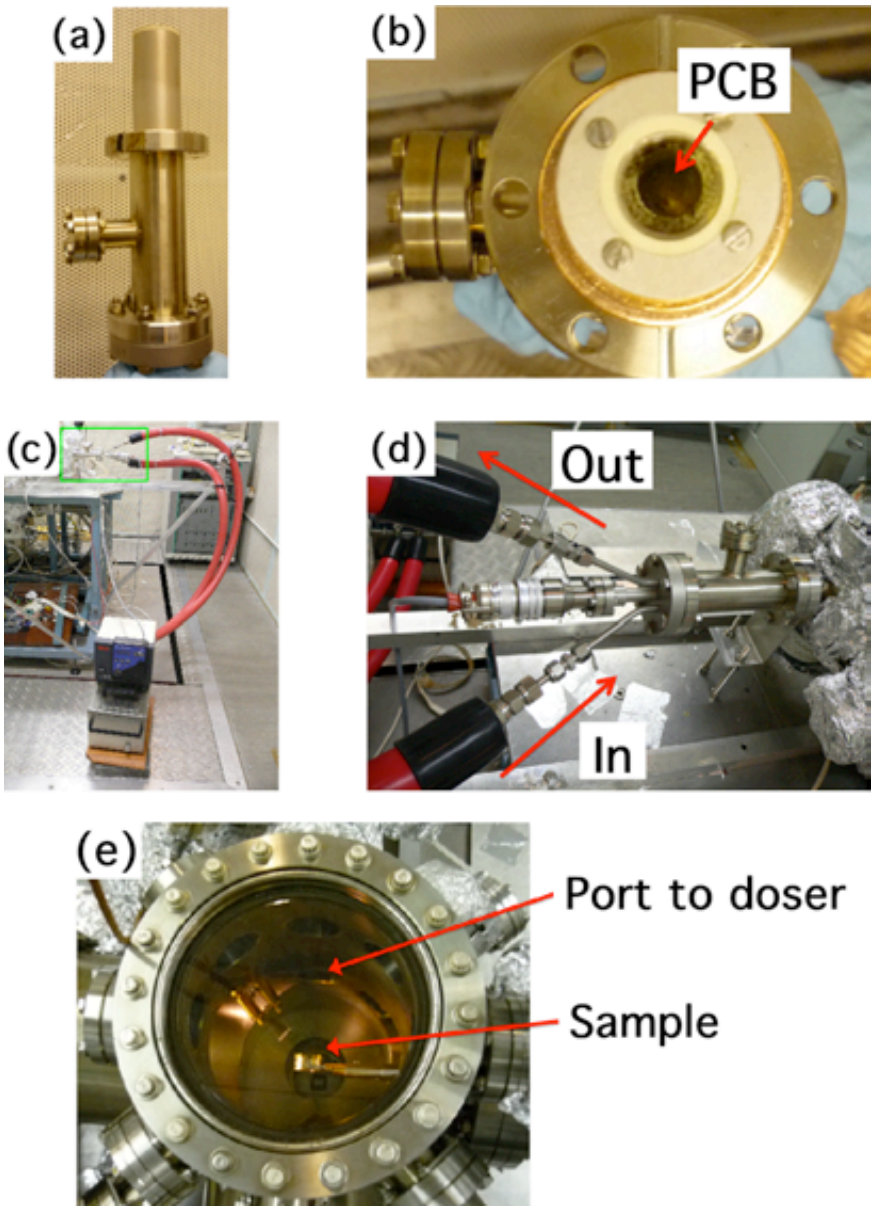

Figure 3.16. (a) Near-ambient temperature cell (NATC). (b) PCB molecules are deposited inside the cell. (c) The NATC is attached to the load-lock and connected via thermo fluid hoses and a thermostat. The NATC on the load-lock is highlighted by the green rectangle. (d) Higher resolution image of the NATC from another direction. The outlet has to be in the upper position. (e) The silicon sample is rotated to be vertical in relation to the port from the load-lock for molecule dosing.

To introduce the PCB molecules onto the silicon sample, the load-lock has to be set in high vacuum at 10^{-7}-10^{-6} Torr. Then, the effusion cell is heated up to 40-50 °C. The pressure at the load-lock increases from background pressure due to PCB molecules evaporate at higher rate. The clean reconstructed silicon sample is moved from the STM chamber to the preparation chamber in which the base pressure is normally in the order of 10^{-10} Torr with the main gate valve (V1) opened. The sample has to be located in same position as the port from the cell (the load-lock) and the plane of the sample has to be perpendicular to the port (as shown in Fig. 3.16 (e)). The aim of this is to maximize the cross section of the molecular flux hitting the sample. The small gate valve between the preparation chamber and the load-lock (V3) is opened slowly and the increasing pressure in the preparation chamber is monitored intensively until the desired quantity of molecule dosing is achieved. Then, the sample is transferred back to the sample stage in the main chamber. Exposures are calculated in Langmuir with uncorrected pressure (1 L=1×10^{-6} Torr s). For example, to achieve 0.01 ML of PCB, the silicon sample has to be exposed to PCB molecules for 2 seconds at 5×10^{-9} Torr. It is difficult to regulate the exact exposure as the pressure in the preparation chamber cannot be fully controlled by the valve. Furthermore, the sample may be exposed to PCB molecules in the chamber during transfer back to the main chamber. However, these uncontrolled effects have a minor contribution to molecule coverage. After molecule dosing has finished, the heating of the cell and the load-lock pumping can be stopped to prevent molecule loss from the cell and to prepare the cell for STM operation. V7 can optionally be closed before venting the load-lock to prevent N_2 molecules contaminating the PCB in the effusion cell.

3.6 Computer program

STM images for the experiments on Si(111)-7x7 were processed mostly by a MATLAB computer program written by Dr Peter A. Sloan. Applying this program to STM images leads to a very effective result analysis with fast processing. The program procedure contains two parts namely searching for molecules and comparing before and after images.

3.6.1 Searching for molecules

This part of the program's procedure aims to find adsorbed molecules on the Si(111)-7x7 surface. Raw STM input-images should have 10 pixels (or line) per nanometre. Thus, each Si adatom is therefore covered by ~25 pixels. The program transforms raw STM images (e.g. RHK or Nanonis format) to a new format, i.e. a simple two dimensional matrix. All of the analysis performed is based on this 2D matrix. The elements of the matrix are the raw Z-piezo height. Parameters of the STM image such as image such as image size, number of lines, bias voltage, tunnelling current, time when scan started and total time for scan are also tagged onto the matrix.

After the input-image is converted to the matrix format, the user has to select the region which is of interest in the input-image for analysis. Steps, grain boundaries, obvious contamination and large regions of defects can therefore be removed from the subsequent image analysis. A line-by-line inear normalization is then performed only on the selected region. In order to search for molecules in th image, the program has to recognize the locations of adatoms and corner holes in the input-image. This can be done when coordinates of unit cells are explored. Firstly, the input-image is correlated with a library of images of a single corner hole and surrounding corner adatoms. As a unit cell of the Si(111)-7x7 surface is surrounded with corner holes, finding the corner hole positions is the key to specifying unit cells. Next, the orientation of the input-image corner holes is determined by applying the best matched corner hole image from different angles. This best matched corner hole image is correlated to the input-image and then a correlation-image with maxima at all corner hole sites is created. A box centred on the centre of the input-image is used to find the maximum number of corner-hole positions in

the correlation-image. The location of cormer holes and unit cells are specified in the box. Then the locations of the neighbouring corner holes are predicted by utilizing the size of the image, the size of a unit cell and the angle of rotation. Predicted points in the input-image search in a 3 Å x 3 Å box around them in the correlation-image in order to ensure maximum correlation. This method allows a small degree of thermal drift and piezo creep in the input-image to be corrected for. From the known unit cell, all the locations of corner holes in the input-image are found sequentially by the searching and predicting procedures mentioned above in a spiral fashion around the know unit cell until the entire chosen region has been covered. In each unit cell, the adatom locations are corrected for by applying the neighbouring corner hole coordinates.

There are two ways to search for adsorbed molecules or occupied adatoms sites. These are

A) The program designates occupied or unoccupied adatom sites from guesses based on a simple threshold (0 nm) level (The state is designated as occupied if the level is less than 0 nm). The user can correct this threshold level if the guesses are wrong.

B) A unit cell with some adsorbates is chosen by the user to give the threshold of occupied or unoccupied level to the program.

From given information, the average heights of an occupied and unoccupied site are determined within a 2 Å radius around each of the 12 adatom sites. Next, each unit cell and adatom site is tested with the average height within that 2 Å radius in order to determine the occupied or unoccupied height compared to the previous step. By using this procedure, the threshold for occupied or unoccupied sites is set for each individual input-image. Moreover, noise and tip state problems in the STM images are almost eliminated from the analysis process.

3.6.2 Comparing before and after images

A pair of sequential STM images (called “before” and “after”) need to be compared so that interesting quantities such as the number of molecules which have desorbed from the before image, can be known. Initially, before and after images are analyzed to locate molecule

coordinates by searching for molecules. The input-image matrices of the before and after images, which address occupied and unoccupied sites, are correlated to generate a new matrix containing only those unit cells which exist in both the before and after image. In this new matrix, 12 adatoms in each unit cell are labelled according to whether they were occupied or unoccupied in the before and the after images. From this matrix, individual adsorbed molecules losing their adsorbed sites can be detected. The change in the total number of adsorbed molecules can therefore be measured.

Chapter 4
One-electron dissociation of chlorobenzene

In this chapter, the dissociation of chlorobenzene (PhCl) on the Si(111)-7×7 surface was studied using room temperature STM. The structure of chlorobenzene adsorption on the Si(111)-7×7 surface was introduced. The displacement of molecules from the electric field effect and tip-molecule interactions in STM images was investigated to check the valid parameters for making "passive" images. The dissociation of the chlorobenzene process at room temperature was conducted. An analytical scheme was used to analyse experimental data to show how STM manipulation can induce dissociation and desorption, which together present a coupling effect in the calculation. A new one-electron dissociation process, combined with a two-electron process at room temperature [94], was explored. Temperature-dependence experiments for molecular dynamics (i.e. displacement, desorption and diffusion) were established to explore the energy barriers for these dynamics processes. The calibration of STM-induced displacement of molecules from thermal effects was performed. Temperature-dependent experiments above room temperature were then shown to promote the one-electron dissociation process. The activation energy of the one-electron process shows that it proceeds via a physisorbed state, the molecule being promoted from the chemisorbed states by thermal excitation.

4.1 Introduction

4.1.1 Adsorption of chlorobenzene on the Si(111)-7×7 surface

4.1.1.1 Si(111)-7×7 surface

The structure of Si(111)-7×7 can be described with the dimer-adatom-stacking fault (DAS) model proposed by Takayanagi *et al.* [172]. This surface contains several types of distinct surface atoms containing: adatoms–the atoms at the first top layer on the surface, rest atoms–the atoms at the second top layer where their dangling bonds are not saturated and corner holes–atoms at the fourth top layer located at the corner of the cell are surrounded by a ring of 12 atoms. These surface atoms are located on two main distinguishable sites, faulted and unfaulted halves, to form a unit cell as shown in Fig. 4.1. Adatoms are located on the top surface layer and divided into three corner adatoms and three middle adatoms for each half unit cell. Rest atoms are in the second subsurface layer and the corner holes are in the fourth layer. All these surface elements provide dangling bonds. There are 19 dangling bonds in one unit cell. Fig. 4.2 (a) shows an unoccupied state STM image of clean Si(111)-7×7 taken with +1 V sample bias, 100 pA. The unit cell is marked with a blue box, the orange balls correspond to adatoms and the dark circles are corner holes. Half unit cells can be distinguished from occupied states by a negative STM image, which shown in Fig. 4.2 (b) taken with –1 V sample bias, 100 pA. It is known that for negative bias voltage images the faulted half appears brighter than the unfaulted half. Rest atoms in the subsurface can be observed as each rest atom surrounded with three adatoms above them.

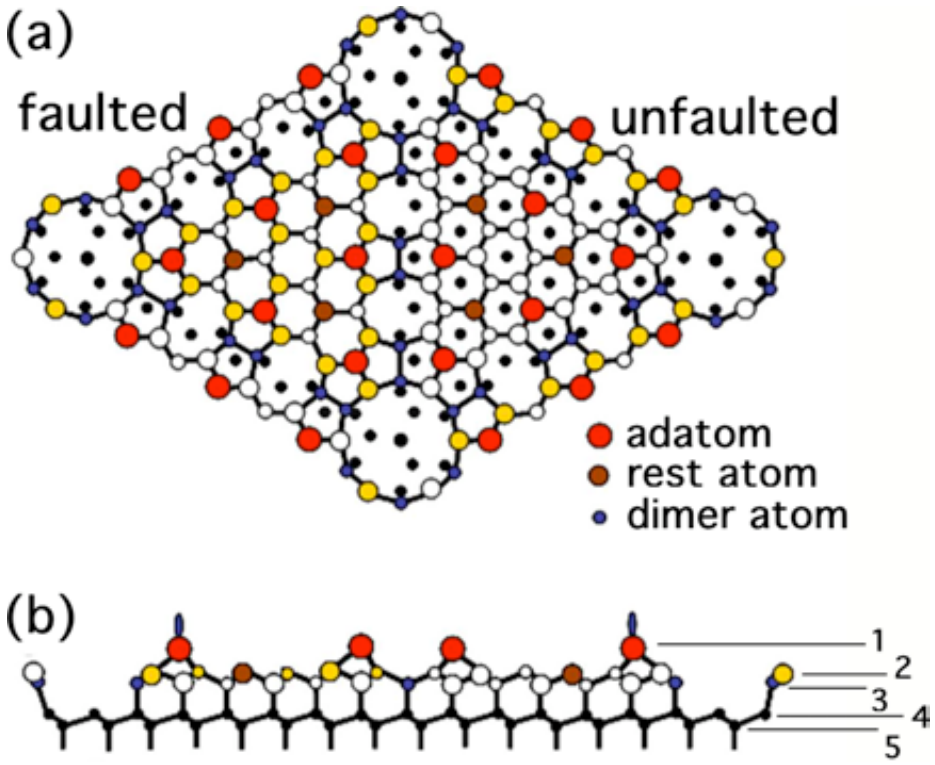

Figure 4.1. Schematic diagram showing the (a) top and (b) side view of the Si(111)-7×7 DAS model. The faulted (Unfaulted) side is the main triangle on the left (right). Image modified from ref. [173].

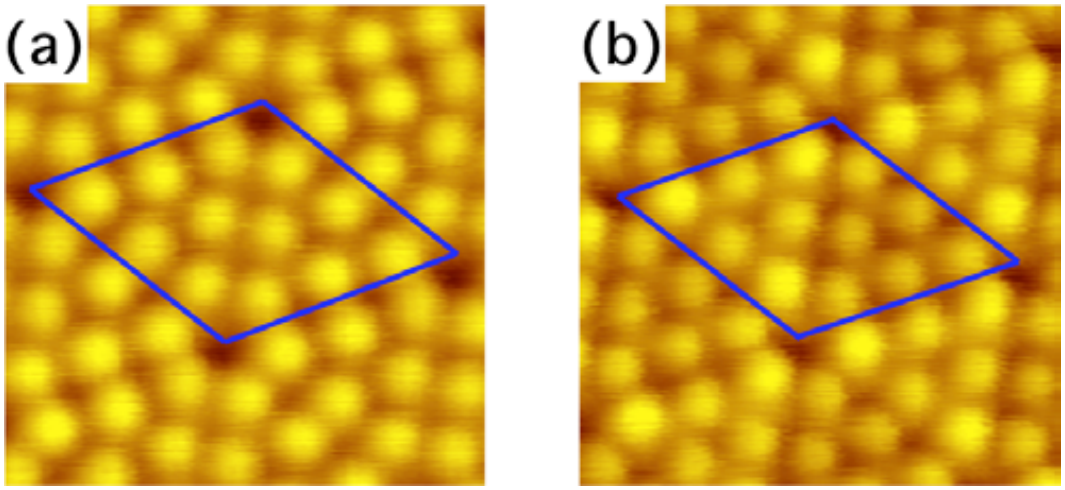

Figure 4.2. Clean Si(111)-7×7 STM images taken with (a) +1 V, 100 pA. (b) –1 V, 100 pA. The unfaulted site appears less bright than the faulted site at negative sample bias voltage. The unit cell is illustrated by the blue box.

4.1.1.2 Adsorption configuration of chlorobenzene on the Si(111)-7×7 surface

The adsorption of the chlorobenzene molecule on the Si(111)-7×7 is displayed in the STM images of unoccupied states in Fig. 4.3 (a). The middle adatom (depicted by the blue arrow) appears slightly darker then the clean adatom, and the rest atom can be noticed nearby. This is because one of the carbon atoms in phenyl ring was saturated by bonding with the dangling bond of the adatom and another bonded with the rest atom. This chlorobenzene bridging configuration adsorption was proposed by Cao *et al.* [174] because 2,5-carbon atoms in the chlorobenzene ring bind with a pair of nearest neighbour adatoms and rest atoms through dangling bonds as shown in Fig. 4.3 (b). This is called the "bridging configuration". The whole chemisorbed molecule tilts ~13° with respect to the surface plane. The 2,5-carbon atoms in chlorobenzene change their hybridisation from sp^2 to sp^3 to form chemisorption. This leads to losing molecule planarity by the non-bonded part bending upwards like a butterfly.

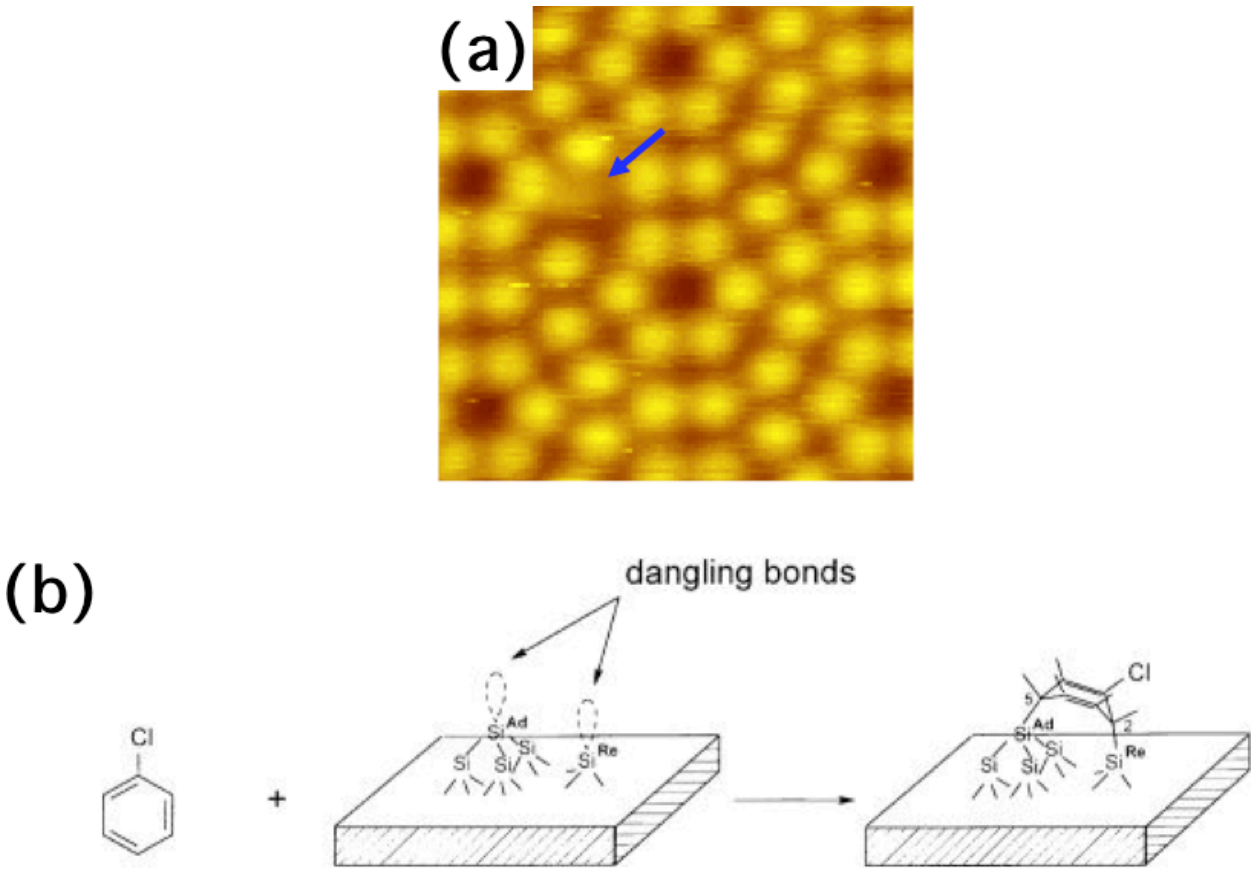

Figure 4.3. (a) STM image of chlorobenzene (C_6H_5Cl) adsorption on the Si(111)-7×7. The blue arrow points to the adsorbed molecule. (b) A schematic diagram of chlorobenzene adsorption on the Si(111)-7×7. Note that the 2,5-carbon atoms in C_6H_5Cl are stereoselectively bonded to two adjacent adatom-rest atom sites in the unit cell. Image modified from ref. [174].

4.1.2 Dissociation of chlorobenzene

The mechanism of chlorobenzene dissociation can be revealed by electron transmission (ET) spectroscopy and simulation [175-180]. Electron capture is also well known to result in the dissociation of molecules as:

$$PhCl^- + e^- \rightarrow Ph^\bullet + Cl^- \quad (4.1)$$

via a dissociative electron attachment (DEA). An interacting electron that is trapped in a molecule has an energy that resonates with the molecular state. This produces a short-lived radical anion that is stable enough to allow the electron to interact with the molecules and break the C-Cl bond. The key factors to achieving dissociation are the electron energy and temporary anion lifetime. The adsorption of molecules on the surface can affect these parameters. Therefore, molecules on the surface dissociate through different processes [94] than molecules in the gas phase [175-180].

4.1.2.1 Dissociation in the gas phase

Many experiments and calculations studying chlorobenzene dissociation in the gas phase have revealed the nature of bond breaking using DEA to unsaturated halocarbons [175-180]. Fig. 4.4 presents the excitation of the vibrations (k,l), p and q of chlorobenzene molecules indicating the selectivity of resonant vibrational excitation. Vibration p is ring breathing mode which is excited by electron attachment to π* orbitals on the C-C bonds. Vibration q is C-Cl stretch mode which is excited by electron attachment to $\sigma^*_{C\text{-}Cl}$ orbitals. Their board band peaks are at 4.5 eV and 2.6 eV. The superposition of excitation of the vibration k and l was observed in the band around 0.8 eV. Both vibration modes are located on the ring with involving C-C stretching. Therefore, it was excited by temporary electron attachment to π* orbitals. Table 4.1 shows the vertical attachment energies (VAEs) from the ET spectroscopy (ETS) studies of anion states, which correspond to the negative value of the vertical electron affinities. It has been found that

the VAE of the low-lying π* orbital is lower than that of the σ* orbital [176,177] and that the maximum dissociative yield occurs near the lowest π* resonance energy [175-177]. Therefore, when an electron collides with a molecule to form a temporary negative ion, it is preferably captured inside the molecule in the π* orbitals, not the σ* orbitals. In the ground state, the π* orbital of a neutral chlorobenzene molecule is isolated from the σ* orbital by the C-Cl bond lying over the nodal plane of the π* orbital [175]. This symmetry of the orbital configuration prevents electron transferring to the chlorine atom due to no coupling of the π* and σ* orbitals, causing a high activation barrier. It is crucial that an excess electron interacts with the chlorobenzene molecule transferred to the chlorine atom to form a negative chlorine ion for the

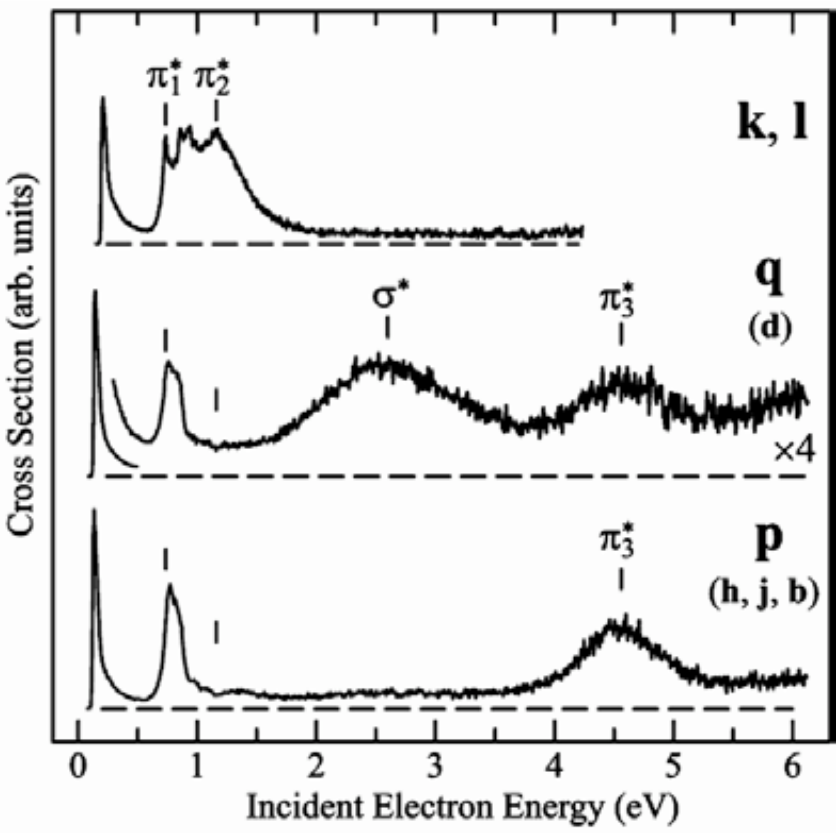

Figure 4.4. Cross sections for exciting the vibrations p, q and (k,l) as indicated on the right. The vibrations given in parentheses lie close in energy and overlap partly with the main vibrations. Image and caption modified from ref. [180].

	VAE (eV)	
	ETS	Theory
π_1^* (b_1)	0.8	0.96
π_2^* (a_2)	1.2	0.97
σ^* (a_1)	2.6	2.30
π_3^* (b_1)	4.6	5.5

Table 4.1. Experimental and calculated VAEs using the Koopmans theorem with HF/6-31G* orbitals [180].

C-Cl bond dissociation. Spontaneously, the excess energy from the electron impact is transferred to excite the molecule vibrational modes [175]. The important mode for C-Cl bond breaking is the excitation of an out-of-plane bending of the C-Cl bond, leading to a mixing of the π^* and σ^* orbitals [180], as shown in Fig. 4.5. Through the vibronic coupling of the temporary molecular anion, the symmetry is broken and the activation barrier is reduced [175,180]. Then, the electron is transferred from the π^* orbital of the molecule to the σ^* orbital of the C-Cl bond. This leads to the production of Cl^-. They are dissociation of the C-Cl bond [175]. Therefore, the dissociation process in the gas phase requires one electron to proceed.

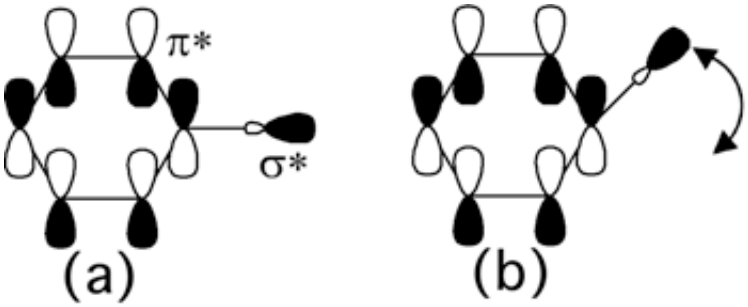

Figure 4.5. The C-Cl bond bending mode: (a) the C-Cl bond lies on same plane as the ring. There is no coupling between the π^* orbital of the molecule perpendicular to the ring plane and the σ^* orbital of the C-Cl bond. (b) The C-Cl bond wagging out-of-the plane. Images modified from ref. [181].

4.1.2.2 Dissociation on the surface

Experimental studies have shown that a chlorobenzene molecule can be dissociated by either an electron [93] or a photon [182] on the Si(111)-7×7 surface. Unlike one-electron dissociation in the gas phase, the dissociation process of chlorobenzene on the Si(111)-7×7 surface by STM at room temperature is found to require 1.8 ± 0.3 electrons [94]. It is considered to be two-electron process as shown in Fig. 4.6. The important factor to determine differences between two distinct conditions is the lifetime of the vibrational coupling mode that allows the electron transfer to the mixing of the π*/σ* orbitals by relaxing in the electron transferring barrier [183]. The lifetime of negative ion resonance (~1 fs) on the surface is shorter than that of the gas

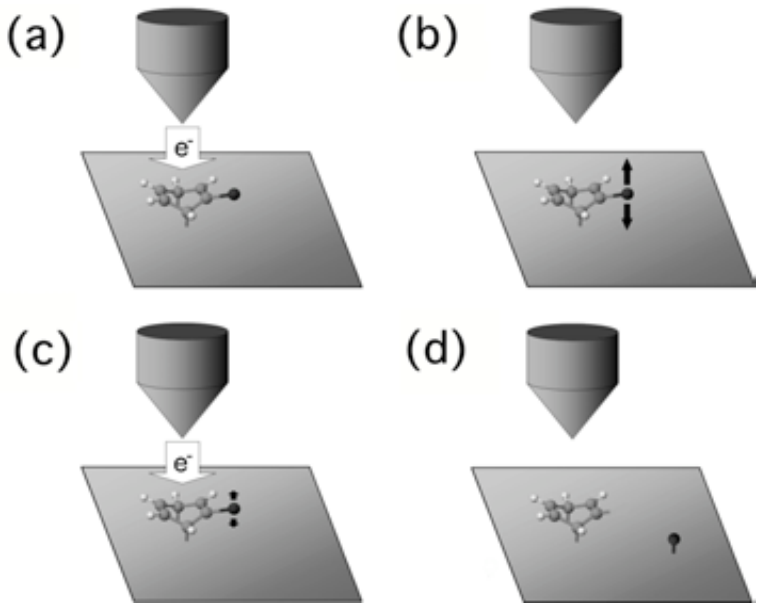

Figure 4.6. STM-assisted two-electron dissociation process on a surface. (a) An electron from the STM tip interacts with the molecule. (b) The C-Cl wag mode is excited by some dissipated energy from the electron before leaving the molecule to the substrate. (c) The second electron is captured in the π* orbital and the C-Cl out-of-plane bending mode is excited. (d) The electron is transferred to the σ* orbital by mixing the π* and σ* orbitals, resulting in C-Cl bond breaking by DEA. Images and capture modified from ref. [94].

[184,185]. At room temperature, molecules are in a chemisorbed state on the surface. A butterfly-like adsorption configuration with the di-σ bonding of chlorobenzene on the Si(111)-7×7 has been reported, which frees the C-Cl bond from substrate interactions [174]. In the proposed process [94], the first electron from a STM tip is captured in molecules forming a temporary negative ion. Because the desorption of chlorobenzene is a one-electron process, most adsorbed molecules in this state will desorb. However, some molecules remain on the surface and some are in a "pre-dissociation state", because the energy from the first electron excites the vibration of the C-Cl wagging mode, thereby reducing the activation energy barrier for electron transfer. If a second electron from the STM tip interacts with the molecule while it is in the pre-dissociation state, it can overcome the relaxed barrier of the π*/σ* mixing orbitals to the C-Cl bond. Similar to the process in the gas phase, this leads to C-Cl bond breaking and generates a Cl^- ion, which is ejected and possibly adsorbed back onto the surface at a certain distance from the molecule.

4.2 Current dependence of chlorobenzene displacement

Because the gap between the tip and surface is ~10 Å, there is a strong electric field in between (~10^9 Vm^{-1}). The electric field could affect the displacement of the molecules, i.e. desorption or diffusion. This displacement of the molecules from the electric field is enhanced when the distance of the tip-sample is reduced by increasing the tunnelling current. The reduction of the tip-sample gap also increases the tip-sample interactions. The displacement of molecules can change the population of adsorbed molecules by taking STM images. Measuring this effect is important for the main experiments to ensure that the displacement of molecules from scanning a STM tip does not vary by increasing the electric field or the tip-sample interactions.

4.2.1 Experimental methods

The silicon sample was flashed to generate the Si(111)-7×7 surface in the STM chamber. This procedure was performed overnight with a computer-controlled power supply to automatically apply a current through the sample at a set value and time. This reduces thermal drift for experiments on the following day. The chlorobenzene molecules were prepared, purified and introduced by the method described in Chapter 3.

The displacement of molecules can be observed by comparing two consecutive STM images to find out which molecules desorb or diffuse. The electric field effect in the STM junction was varied by changing the distance between a tip and substrate by tuning the value of the tunnelling current (2 to 500 pA). The effects of thermal drift and piezo creep generally appear in an STM image as a distorted image. These effects are enhanced at elevated temperatures. They can also cause a problem when comparing two STM images, for example, the subtraction of two images. To overcome these problems, a homemade computer program written by Dr. Peter A. Sloan (see chapter 3) was used to search the molecules in each unit cell on the surface and record the coordinates of molecules in a new formation. Then, the two STM images were compared by the program to explore which molecules were displaced from their original sites. By using this program, analysing the displacement of the molecules was conducted accurately.

4.2.2 Results and discussion

Fig. 4.7 shows the displacement rate from consecutive STM images taken with +1 V and a tunnelling current of 2 to 500 pA. The displacement rate leads to a small change on the tunnelling current. This implies that increasing the electric field or tip-molecule interaction does not change the population of the molecules at a bias voltage of +1 V. Therefore, STM images taken with a voltage and tunnelling current in this range are strictly “passive”.

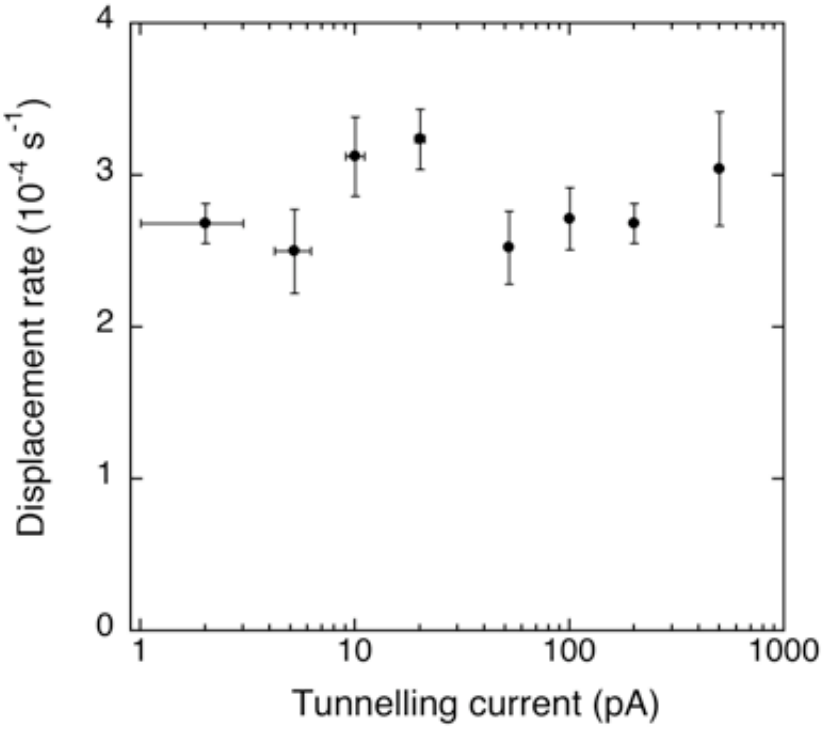

Figure 4.7. The dependence of the displacement rate at +1 V with a tunnelling current of 2 to 500 pA, 297 K. Results show molecular displacement is current independence. Thus, scanning images in this A total of 111,490 molecules were accounted in the analysis.

4.3 Dissociation of chlorobenzene at room temperature

The two-electron dissociation process of chlorobenzene by electrons from a STM tip at room temperature was reported previously by P. A. Sloan and R. E. Palmer [94]. Here, we repeated this experiment with our adopted calculation to determine a more accurate the number of electrons involved in the dissociation process.

4.3.1 Results and discussion

A typical chlorobenzene of 0.3 L was exposed to the reconstructed Si(111)-7×7 sample. When dosing was finished, the presence of adsorbate molecules on the surface was confirmed by

STM images at +1 V. The dissociation of the chlorobenzene molecules can be induced by scanning the STM tip to a whole image with a bias voltage of +3.5 V [93], called a "manipulation scan". The images of the adsorbed molecules before and after the manipulation scan were taken with passive parameters (+1 V, 100 pA). The molecular dissociation on the surface can be investigated by taking an array of sequential STM images before and after manipulation. Six distinct tunnelling currents (50, 100, 200, 300, 400 and 500 pA) in the manipulation scan were selected to observe any changes in the dissociation rate. The STM tip state has been shown to play a crucial role in both induced molecule dynamics [186]. To avoid tip influence on the results at a particular tunnelling current, the tunnelling current was switched to other values (from the set of tunnelling currents) after an experiment was finished to average the tip effect. The quantification of the number of distinct molecules in the STM images was achieved by knowing the different characteristics of each molecule through features appearing at various voltages. Chlorobenzene molecules appear as dark spots at +1 V and +2 V with respect to silicon adatoms [93]. By contrast, chlorine atoms can be identified as dark spots at +1 V and bright spots at +2 V [187]. From four sequential STM images, we counted the population of dissociation events, N_{diss}, as the number of chlorine atoms from the difference between the number of bright spots in the +2 V images before and after manipulation. The voltage and current used to image the chloride atoms have barely an effect on displacing the chloride adsorbed site, since the probability of the diffusion and desorption of the chloride adsorbate caused by hot electrons is much less than 1% [188]. Therefore, the images scanned at +2 V are still "passive". Fig. 4.8 shows a series of consecutive STM images of a chlorobenzene partially covered by the Si(111)-7×7 surface taken at the same location with bias voltages of +2 V (a), +1 V (b), +1 V (c) and +2 V (d). Fig. 4.8 (c) and (d) show that the manipulation scan induces both the desorption and dissociation of the chlorobenzene molecules. To uncover the precise molecular dissociation mechanism, it is necessary to measure desorption processes simultaneously with dissociation, as described later. Similarly, the population of desorption events, N_{des}, is found from comparing the number of dark spots in +1 V images before and after manipulation. Precisely analysing the location of the phenyl ring is outside the scope of this study. There are two possible cases for the phenyl ring after dissociation. First, if the phenyl ring still bonds to the adatoms, it appears as a dark spot.

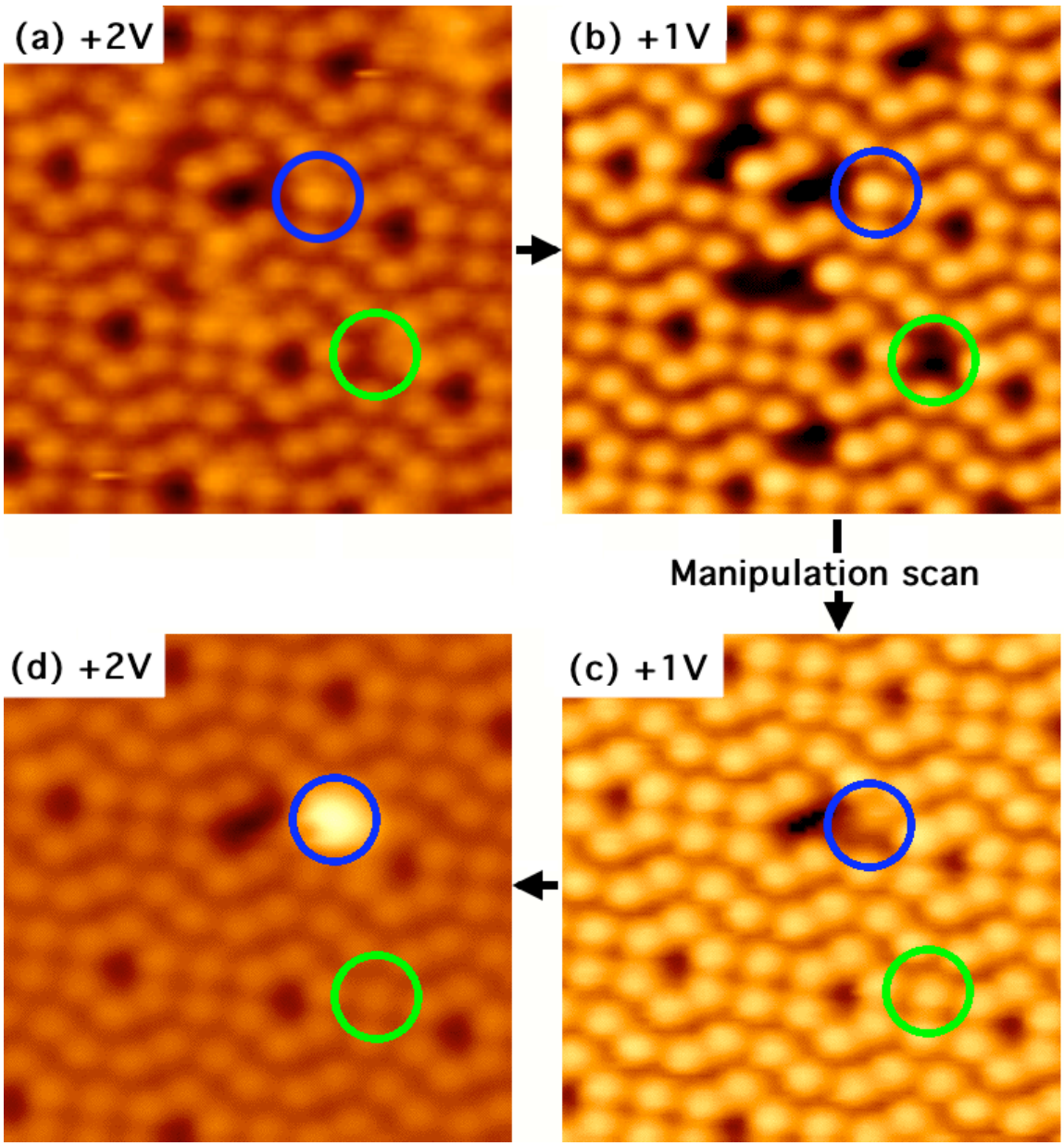

Figure 4.8. Sequential STM images (80 Å × 80 Å) selected from full image of 450 Å × 450 Å demonstrating the dissociation and desorption of a chlorobenzene molecule on the Si(111)-7×7, before manipulation at a surface bias voltage of (a) +2 V and (b) +1 V and afterwards at (c) +1 V and (d) +2 V (tunnel current 100 pA). The blue circle marks where dissociated chlorine attaches to the silicon adatom after the manipulation scan of +3.5 V. The green circle indicates one of the molecule desorptions after manipulation.

The population of desorption can be calculated from $N_{des} = N_{dark}^{before} - N_{dark}^{after}$. Second, if the dissociated phenyl ring is desorbed, there will be no entity remaining on the surface. Thus, the population of desorption can be calculated from $N_{des} = N_{dark}^{before} - N_{dark}^{after} - N_{diss}$. As the desorption yield is much larger than the dissociation yield [94, 95, 186] and the difference between the two cases is only N_{diss} term, there is no significant difference between the two cases. Therefore, it is assumed that the phenyl ring remains adsorbed after dissociation.

To confirm that adsorbed molecules require more electrons than molecules in the gas phase, the number of electrons required for dissociation on the surface was calculated. For this, elaborated quantitative analysing of both the dissociation and desorption is required.

The rate of dissociation can be written in form of power law as:

$$\frac{dN_{diss}}{dt} = k_{diss} N_a \left(\frac{I}{e}\right)^n , \tag{4.2}$$

where N_{diss} is the number of dissociation events, k_{diss} is the dissociation yield, N_a is the population of chlorobenzene molecules, I is the tunnelling current during manipulation, e is the absolute charge of an electron and n is the number of electrons required to break a C-Cl bond. In the rate of desorption, the one-electron process [95] can be written as:

$$\frac{dN_{des}}{dt} = k_{des} N_a \left(\frac{I}{e}\right), \tag{4.3}$$

where N_{des} is the number of desorption events and k_{des} is the desorption yield. The rate of thermal desorption can be ignored considering that it is smaller than the rate of desorption induced by the STM by a factor ~10^7 [95, 189]. The molecules lost via thermal desorption will be only considered in elevated temperature experiments. Because a manipulation scan can induce both dissociation and desorption, these two processes have to be coupled in the rate equations. To find n, a calculation involving both reaction rates is needed. Integrating the ratio of the rate of dissociation to the desorption and taking the natural logs gives:

$$\ln\left(\frac{N_{diss}}{N_{des}}\right) = \ln\left(\frac{k_{diss}}{k_{des}}\right) + (n-1)\ln\left(\frac{I}{e}\right). \tag{4.4}$$

This equation can be used to determine n easily.

Fig. 4.9 shows the log-log plot of the $\frac{N_{diss}}{N_{des}}$ as a function of $\frac{I}{e}$. Applying equation (4.4) to the data in Fig. 4.9, an n value of 1.4 ± 0.1 electrons is obtained. This result is less than 1.8 ± 0.3 electrons that were interpreted as two-electron dissociation process of chemisorbed chlorobenzene on the surface in previous study [94]. This suggests that the measured dissociation events are a mixture of one-electron and two-electron dissociation processes. A new mechanism of one-electron dissociation process on the surface was explored here. It is possible to decouple both processes depending on the temperature as shown in next section.

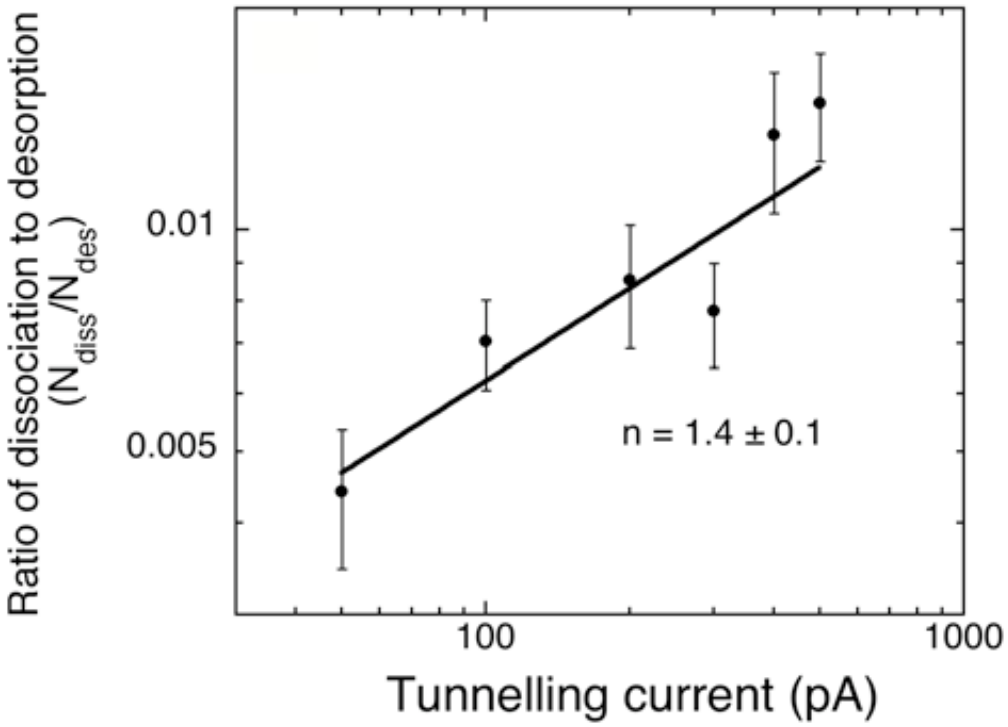

Figure 4.9. The ratio of dissociation to desorption as a function of the tunnelling current at room temperature for a manipulation voltage of +3.4 V. The average number of electrons required to break the C-Cl bond is 1.4 ± 0.1.

4.4 Temperature-dependence of chlorobenzene dissociation

Since the chlorine products from the one-electron and two-electron dissociation processes are indistinguishable – even thorough STM image analysis may identify the dissociation process – this is not within the scope of this study. Two assumptions are proposed: the two-electron process is temperature-independent and the one-electron process is temperature-dependent, which will be confirmed below. Therefore, it is possible to measure the one-electron process, which decouples from the two-electron process at elevated temperatures.

The same experimental routine as for the dissociation of chlorobenzene at room temperature was carried out at temperatures in the range 297 to 328 K. Thermally induced desorption starts to influence the population of molecules on the surface when the temperature is above 297 K. The molecule population on the surface is reduced through thermally induced desorption. To obtain the same coverage as in the thermal calibration experiments, a larger dose was applied. As was the case for displacement measurement, thermal desorption affects the population of molecules in the image because of the time spent scanning. A calibration can be performed in a similar fashion. Rate equation for thermal desorption is written in form:

$$\frac{dN}{dt} = -\alpha N, \tag{4.5}$$

where α is the rate of thermal desorption (s^{-1}). This desorption rate is shown in Arrhenius equation as

$$\alpha = A\exp\left(\frac{-E_{des}}{k_B T}\right), \tag{4.6}$$

where A is the pre-exponential factor (s^{-1}), E_{des} is the activation energy of the desorption, k_B is Botzmann's constant and T is the sample temperature. By integrating (4.5) and using initial condition of $N(t_0) = N_{before}$, the number of molecules before the manipulation, N_{before_man}, is calculated in:

$$N_{before\_man} = N_{before} \exp\left(-t_0 A \exp\left(\frac{-E_{des}}{k_B T}\right)\right)$$

Similar trend is applied to calculate the number of molecules after the manipulation (N_{after_man}) as

$$N_{after} = N_{after\_man} \exp\left(-t_0 A \exp\left\{\frac{-E_{des}}{k_B T}\right\}\right)$$

$$N_{after\_man} = N_{after} \exp\left(t_0 A \exp\left\{\frac{-E_{des}}{k_B T}\right\}\right)$$

where A (s^{-1}) and E_{des} (eV) are derived from pure thermal desorption as calculated later. Therefore, the number of desorption events in each experimental set can be written in the form,

$$N_{des} = N_{before\_man} - N_{after\_man}$$

$$N_{des} = N_{before} \exp\left(-t_0 A \exp\left\{-E_{des}/k_B T\right\}\right) - N_{after} \exp\left(t_0 A \exp\left\{-E_{des}/k_B T\right\}\right). \qquad (4.5)$$

Fig. 4.10 shows the results of the ratio of dissociation to desorption (N_{diss}/N_{des}) after correcting for thermal desorption. The increase in the ratio suggests the enhancement of the one-electron dissociation process by thermal energy, which is consistent with the assumptions above. To separate the (temperature-independent) two-electron from the (temperature-dependent) one-electron process, the rate of desorption (4.3) is rewritten as:

$$\frac{dN_{diss}}{dt} = k_{diss}^{1e} N_a \left(\frac{I}{e}\right) \exp\left(\frac{-E_{prom}}{k_B T}\right) + k_{diss}^{2e} N_a \left(\frac{I}{e}\right)^2, \qquad (4.6)$$

where E_{prom} is the energy barrier for one-electron dissociation, k_{diss}^{1e} is the dissociation yield for the one-electron process, k_{diss}^{2e} is the dissociation yield for the two-electron process, N_a, I and e are as before and k_B and T are as stated in the thermal calibration. At elevated temperatures, the rate of desorption also includes the thermal processes, not only electron-induced desorption terms. It can be written as:

$$\frac{dN_{des}}{dt} = k_{des} N_a \left(\frac{I}{e}\right) + AN_a \exp\left(\frac{-E_{des}}{k_B T}\right). \tag{4.7}$$

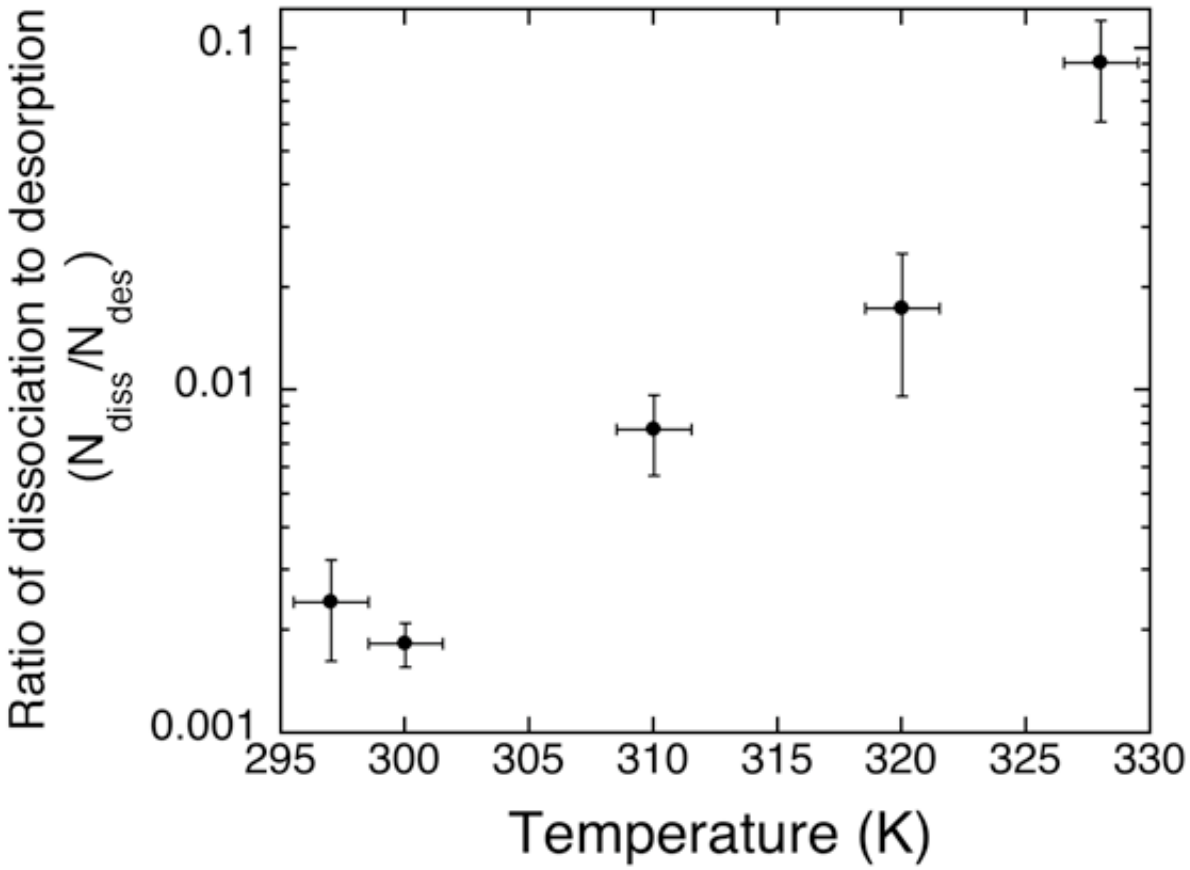

Figure 4.10. Temperature-dependence of the ratio of dissociation to desorption at +3.4 V. An exponential increase shows the enhancement of the one-electron dissociation process, which decouples from two-electron dissociation process at elevated temperature.

E_{prom} in equation (4.6) is important to determine the mechanism of the one-electron dissociation processes. E_{prom} can be derived by taking the ratio of the rates of dissociation to desorption, integrating and rearranging, which gives the rate of one-electron dissociation as:

$$k_{diss}^{1e}\left(\frac{I}{e}\right)\exp\left(\frac{-E_{prom}}{k_B T}\right) = \frac{N_{diss}}{N_{des}}\left[k_{des}\left(\frac{I}{e}\right) + A\exp\left(\frac{-E_{des}}{k_B T}\right)\right] - k_{diss}^{2e}\left(\frac{I}{e}\right)^2. \quad (4.8)$$

In equation (4.8), E_{des} and A are determined from the thermal desorption (as will be described later), k_{diss}^{2e} is derived from the data slope in Fig. 4.10 and k_{des} is inversely temperature-dependent. By using an exponential fit $k_{des} = \eta\exp(-\lambda T)$ to the STM-induced desorption with thermal correction data (shown later in Fig. 4.14), $\lambda = 0.0215$ K^{-1} is derived for a manipulation with +3 V. k_{des} = (2.64 ± 0.23) × 10^{-6} per electron was derived from desorption experiments with +3.5 V and 10-50 pA, which is consistent to the value in previous report as (2.01 ± 0.15) × 10^{-6} per electron [95]. If it is assumed that the decrease in STM-induced desorption from the thermal effect at +3.5 V has the same characteristic as +3 V (applying same λ), η (at +3.5 V) was calculated to be 1.55 × 10^{-3}. Finally, the desorption yield at +3.5 V results to be, k_{des} = 1.55 × 10^{-3}exp(–0.0215T).

Fig. 4.11 shows the temperature-dependent C-Cl dissociation data from Fig. 4.10 recast as the rate of one-electron dissociation, using equation (4.8), and shown as an Arrhenius plot. The exponential fit gives the energy barrier of a thermally promoted one-electron dissociation, the most important result of this work, of E_{prom} = 0.8 ± 0.2 eV. This activation energy is much lower than the C-Cl bond energy of 4 eV [93] and much higher than typical vibrational energies (~meV). Therefore, the activation energy does not associate with either the energy barrier of the C-Cl bond breaking or vibrational excitation which thermal energy above room temperature would enhance vibrational excitation of the C-Cl bending mode. This confirms our assumption that the two-electron dissociation process is temperature-independent. To find out what the energy barrier corresponds to, an understanding of the potential energy picture of chlorobenzene is required.

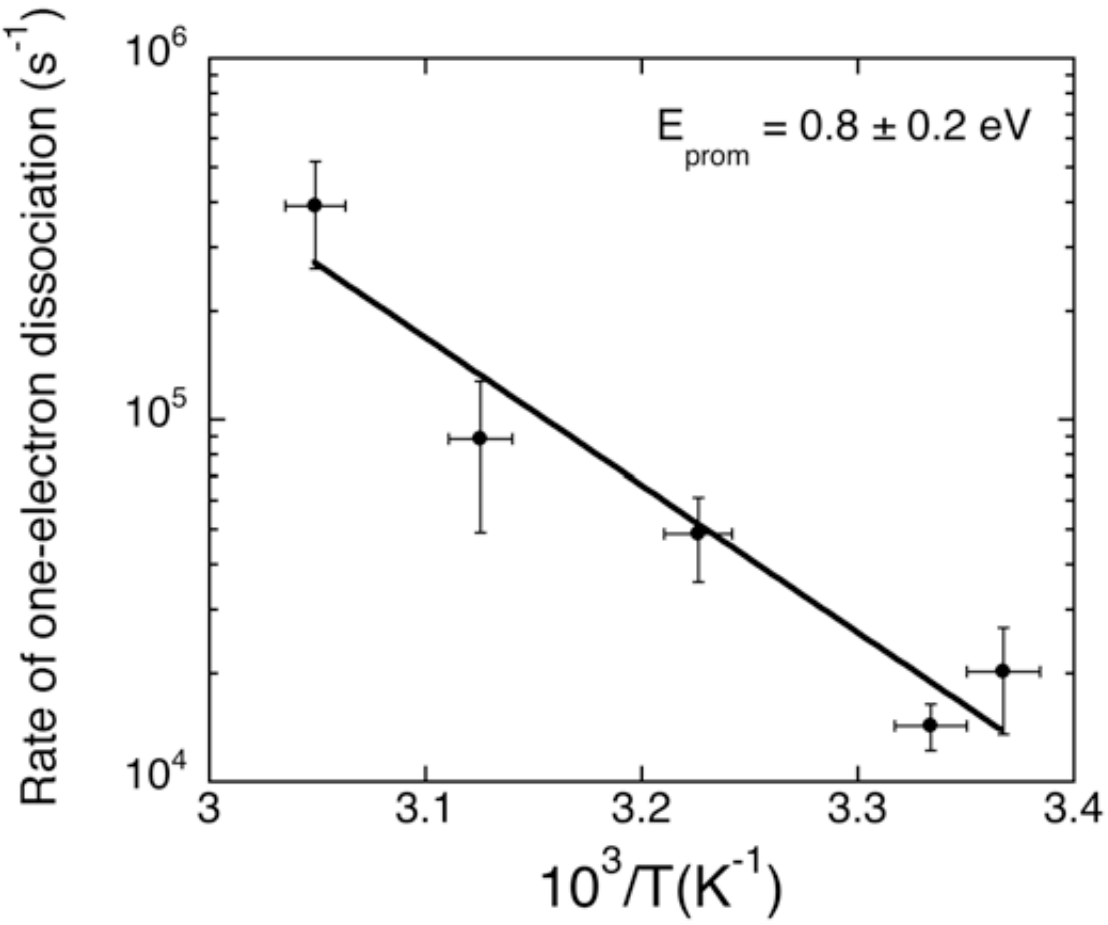

Figure 4.11. Arrhenius plot of the rate of one-electron dissociation. The data were recast from Fig 4.10. The fit gives the energy barrier for thermally promoted one-electron dissociation as 0.8 ± 0.2 eV. This energy range is lower than the energy of C-Cl bond (4 eV) but much more than the energy of C-Cl bending mode (~60 meV). To describe the one-electron dissociation, it is necessary to understand what physical excitation the energy corresponds to.

4.5 Calibration of thermal and STM-induced molecular dynamics on surface

The potential energy of chlorobenzene molecules on the Si(111)-7×7 surface can be determined from the process of thermally driven molecular dynamics on the surface. Thermal energy can lead to changes in the molecular adsorption sites: molecules hop to re-adsorb at newly occupied sites (as molecular diffusion) or by thermal excitation. Either molecules are desorbed to vacuum (as molecular desorption). The accumulation of these changes is called "molecular displacement". The results from the measurement of thermal molecular dynamics as a function of the sample temperature will now be discussed. The key part of this section, the thermal calibration of adsorbed molecules and STM-induced molecular displacement, will be described.

4.5.1 Experimental methods

The RHK 400 STM provides a tungsten filament underneath the sample stage that can connect to a DC power supply, via a feedthrough, to apply a current up to 3.5 A to heat the sample through a radiative heating process. The maximum applied current is limited by the bake temperature of the system at 488 K (145°C). Also, the sample temperature in experiments has to be low enough to keep adsorbed molecules on the surface as thermal desorption becomes stronger. It was found that there are no surviving adsorbed molecules on the surface when the sample temperature rises to 333 K. Larger doses have to be applied to have the same final coverage as before, e.g., 6 L at 310 K. Table 4.2 displays the relationships between the current applied on the filament and the corresponding sample temperature used in the experiments.

At elevated temperatures, thermally induced molecular dynamics such as displacement, diffusion and desorption, start to influence the adsorbed molecules to change their sites. This can reduce the population of adsorbed molecules observed in manipulation scanning because of desorbing during both passive and manipulation scanning. Moreover, the electron-induced desorption rate might be disturbed by the thermal energy above room temperature. To correct

$I_{filament}$ (A)	T_{sample} (K)
0*	289
0	297
0.5	300
0.8	303.5
1.1	310
1.3	314
1.4	320
1.5	328

Table 4.2. Temperature (Kelvin) of a silicon(111) sample as a function of the current through the filament (Ampere) in dissociation of the chlorobenzene experiment. *refers to the air conditioner working at 288 K, whereas normally it keeps the temperature in the lab at ~298 K.

these thermal coupling effects, measuring and calibration are performed. The important parameter to determine the reaction rate in the thermal excitation process is the barrier energy of the reaction. At a particular substrate temperature, a reaction measurement can be taken by recording a series of STM images at the same location. The activation energy of the reaction dynamics can be calculated from the rate equation:

$$\frac{dN}{dt} = -\alpha N, \tag{4.9}$$

where N is the population of adsorbed molecules, t is the measurement time and α is the rate of interested reaction. By integrating, we have:

$$N = N_0 \exp(-\alpha t), \tag{4.10}$$

where N_0 is initial population of molecules and α can be written in temperature-dependence form as:

$$\alpha = A\exp\left(\frac{-E_{Act}}{k_B T}\right), \tag{4.11}$$

where A is the attempt frequency (s^{-1})–the chance of molecules to overcome their barriers, E_{Act} is the activation energy of the reaction, k_B is Boltzmann's constant and T is the substance temperature. E_{Act} in equation (4.11) can be derived from an Arrhenius plot of the reaction rate. Results in this section were analysed by computer program written by Dr. Peter A. Sloan.

4.5.2 Results and discussion

4.5.2.1 Molecular diffusion

The diffusion rate of adsorbed molecules can be deduced by the comparison of individual molecule sites in sequential STM images taken at different times. Precisely the same surface area and same image data were used as previously in displacement measurement to determine the desorption barrier. Sites that were unoccupied in the initial image and then occupied in following image were accounted as a diffusion. Fig. 4.12 presents an Arrhenius plot of the rate of thermal excited molecular diffusion as a function of temperature. The fit provides an attempt frequency of $10^{10.8 \pm 1.3}$ s^{-1} and an energy barrier of 0.84 ± 0.08 eV. Two data points at high temperatures were omitted from this data set because at these temperatures molecules from outside the scanning range are able to diffuse into the scanning range and be counted, thereby interfering with the result. It is known that the diffusion of benzene molecules on the Si(111)-7×7 surface occurs via physisorbed states [190]. Chlorobenzene has the same di-σ bonding configuration on the Si(111)-7×7 as benzene; thus, the diffusion of chlorobenzene can occur in physisorbed states where the interactions between molecules are weak, which might be reflected in the reduction of the attempt frequency to 10^{13} s^{-1}. It can be concluded that the diffusion barrier is the barrier to overcome from the chemisorbed state, where molecules adsorb stably after dosed, to the physisorbed state.

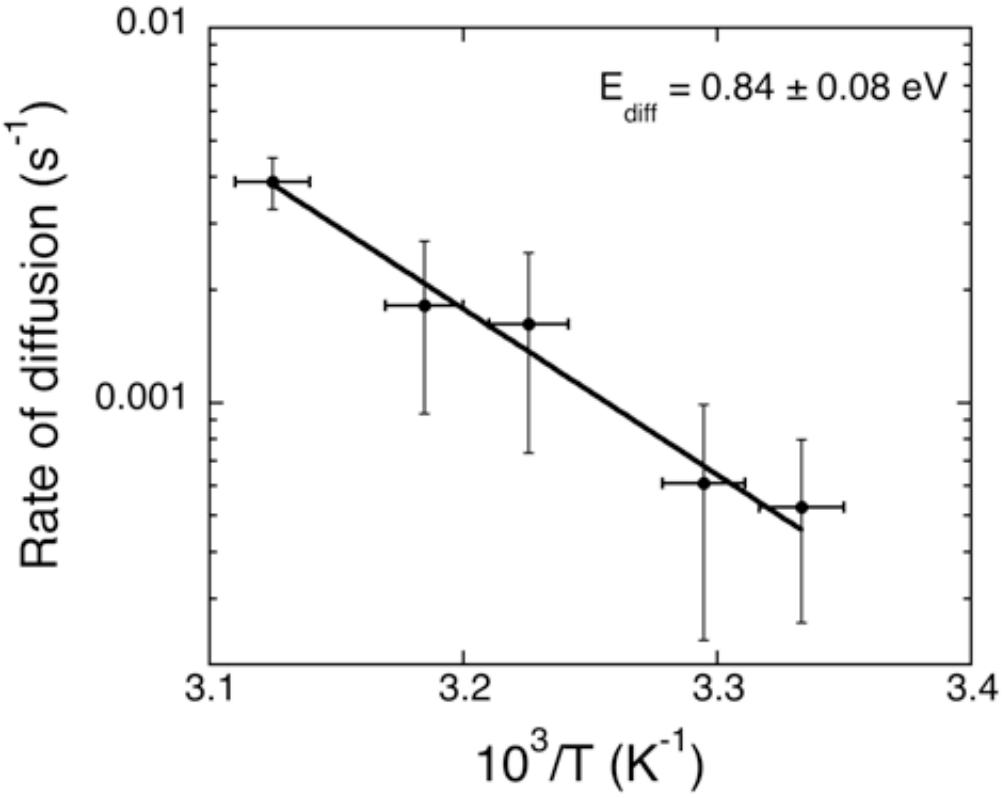

Figure 4.12. Arrhenius plot of the rate of thermal diffusion as a function of temperature measured by STM. The fit provides an energy barrier of 0.84 ± 0.08 eV and pre-exponential factor of $10^{10.8 \pm 1.3}$ s^{-1}. This barrier corresponds to the barrier from chemisorbed to physisorbed state.

4.5.2.2 Molecular desorption

The energy barrier of desorption is the barrier from the chemisorbed state to the unbound state in the gas phase. The desorption of molecules can be derived by excluding diffusing molecules from displacing molecules. The desorption rate can be measured by counting the population of adsorbed molecules in the same region as the time evolution. Fig. 4.13 (a) shows the total number of molecules decreasing as a function of time for different temperatures. From Fig. 4.13 (a), it can be seen that the rate of desorption increases with increasing temperature. Fig. 4.13 (b) displays an Arrhenius plot of the rates of desorption with an exponential fit providing an energy barrier to desorption of 0.98 ± 0.08 eV and a pre-exponential factor of $10^{12.69 \pm 1.37}$ s^{-1}.

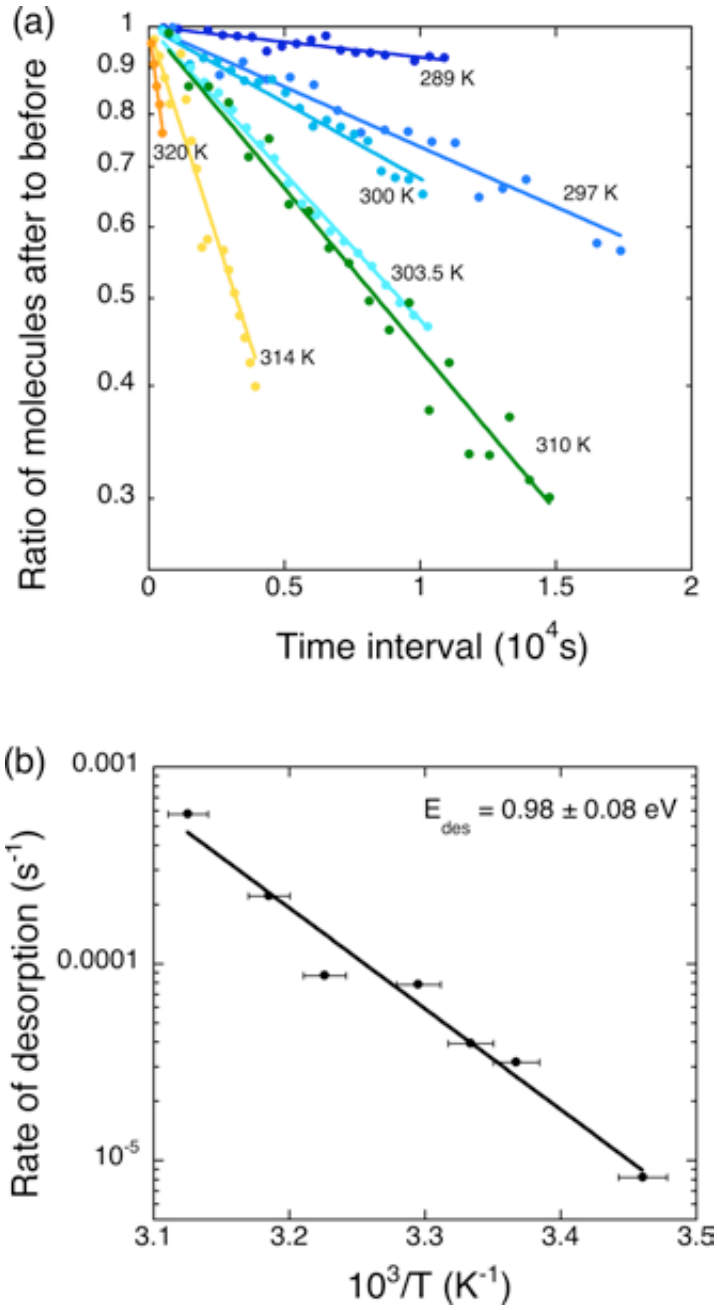

Figure 4.13. Thermal desorption rates of chlorobenzene from the Si(111)-7×7 as measured by STM. (a) Decreasing the population of molecules in consecutive STM images (+1 V, 100 pA, 600 Å × 600 Å) as a function of time at seven temperatures. (b) An Arrhenius plot of the rate of thermal desorption; the fit provides an energy barrier to desorption of 0.98 ± 0.08 eV with a pre-exponential factor $10^{12.69 \pm 1.37}$ s^{-1}.

This is in excellent agreement with results from temperature-programmed desorption experiments that provided E_{des} as 1.01 ± 0.09 eV, although this relied on the usual assumption of 10^{13} s^{-1} for the pre-exponential factor [174].

4.5.2.3 STM-induced molecular displacement

The rate of STM-induced molecular desorption can change as temperature rises above room temperature. This can disturb dissociation analyses at elevated temperatures since desorption and dissociation couple in equation (4.4). To calibrate this effect, STM-induced molecular displacement rates were measured at different temperatures. The calibration of desorption is performed by displacement (assuming no significant difference between the calibration of desorption and displacement). A similar analysis procedure of displacement is applied to determine the electron-induced displacement in the experiments. The difference in the experiments with respect to a purely thermal measurement is a manipulation scan at a +3 V sample bias and 50 pA carried out in between images. It is crucial to avoid applying a very high bias voltage because this can produce dissociation, which can perturb the desorption analysis.

Fig. 4.14 shows the thermal displacement yield with and without thermal correction. Because desorption is a one-electron-driven process, the displacement of molecules by STM-injected electrons can be written as:

$$\frac{dN}{dn_e} = -k_e N, \tag{4.12}$$

then solving (4.12) equation:

$$k_e = \frac{-\ln\left(\frac{N}{N_0}\right)}{n_e}, \tag{4.13}$$

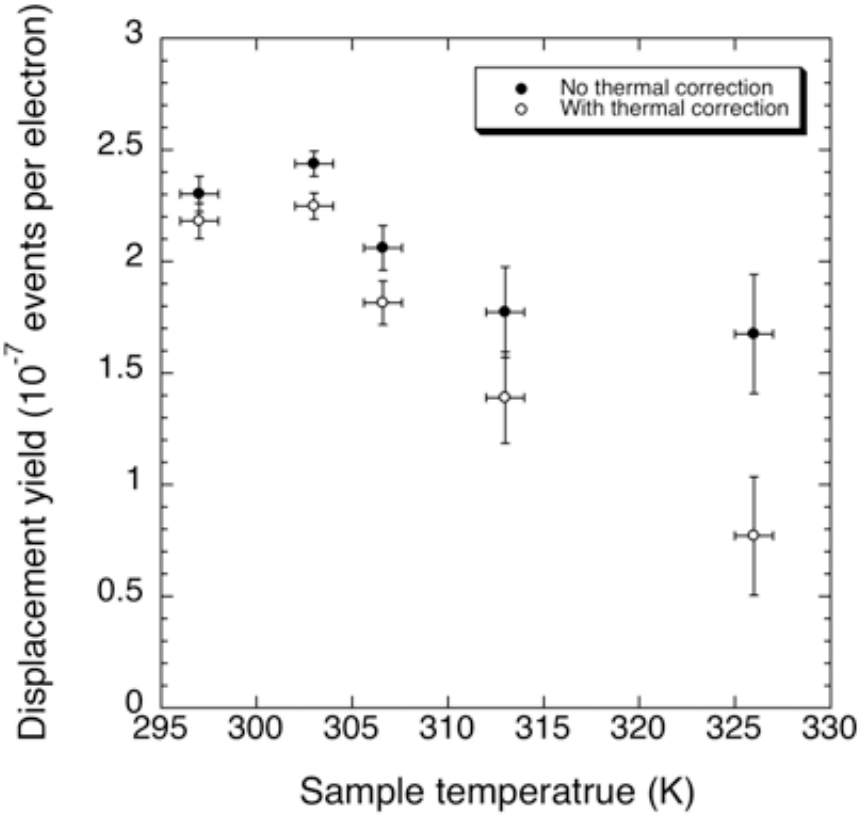

Figure 4.14. The temperature-dependence of STM-induced molecular displacement, with and without correction, for thermally induced displacement. The displacement yield with thermal correction shows the decrease of yields respect as a function of temperature to the one with no thermal correction.

, where k_e is the probability of displacement per electron, n_e is the number of electrons interacting with a single molecule, N is the number of molecules that remain in their original positions and N_0 is the number of molecules in the image before the manipulation scanning. The number of electrons scattering per molecule, n_e, is determined from the parameters used in the manipulation scan, in the form:

$$n_e = \frac{I_0 t_0 L_{mol}^2}{e L_{scan}^2} \tag{4.14}$$

, where e is the absolute charge on an electron, L_{scan} is the size of the manipulation image, I_0 is the tunnelling current, t_0 is the elapsed time for the STM image, L_{mol} is the size of one molecule (approximated as 5 Å). Therefore, the uncorrected thermal displacement yield can be written as:

$$k_e = \frac{-eL_{scan}^2 \ln\left(\frac{N}{N_0}\right)}{I_0 t_0 L_{mol}^2} \tag{4.15}$$

Owing to the time delay, t_0, between the first image and the manipulation, the number of molecules before manipulation, N_0, evolves as:

$$N_0 \exp\left(-t_0 A \exp\left\{-E_{disp}/k_B T\right\}\right).$$

By contrast, the proper number of remaining molecules after manipulation, N, is increased to:

$$N \exp\left(t_0 A \exp\left\{-E_{disp}/k_B T\right\}\right).$$

By applying the corrected number of molecules to (4.11), the exact displacement can be written as

$$k_e = \frac{-2eAL_{scan}^2 \exp\left(\frac{-E_{disp}}{k_B T}\right) \ln\left(\frac{N}{N_0}\right)}{I_0 L_{mol}^2}, \tag{4.16}$$

where A and E_{disp} are determined from the pure thermal displacement measurement as $10^{6.2 \pm 0.3}$ s^{-1} and 580 ± 20 meV respectively. The Fig. 4.14 displays the decrease of the displacement yield with rising sample temperature. The decrease of the yield observed in the corrected thermal results is much higher than in the uncorrected thermal results.

4.6 Potential energy and discussion

Table 4.3 shows the adsorption energy of chlorobenzene and benzene in the chemisorbed and physisorbed states from our experiments and previous reports [174,191-194]. Not only do both molecules have nearly identical molecular structures and chemisorbed configurations, but also their chemisorption and physisorption energies are comparable in each case. It was found that the diffusion of benzene proceeds through the physisorbed state [190], which was also applied for chlorobenzene as discussed in section 4.5.2.1. Therefore, the diffusion barrier is the energy barrier of the transition to a physisorbed state from a chemisorbed state. The energy barrier from the physisorbed to chemisorbed states ($E_{phys-chem}$) of chlorobenzene can be derived as 0.38 ± 0.13 eV. This parameter for chlorobenzene almost equals the direct experimental measurement of benzene [194]. Hence, it is in good agreement with the hypothesis of the diffusion process. Thus, the diffusion energy barrier (E_{diff}) of 0.84 ± 0.08 eV is the energy barrier for a transition from the chemisorbed to physisorbed states ($E_{chem-phys}$). All examined quantities are drawn as complete picture of potential energy in Fig. 4.15.

As elucidated previously, the dissociation of chlorobenzene in the gas phase requires the vibration of C-Cl in an out-of-plane bending mode to mix the π*-σ* orbitals in a "pre-dissociation state". This dissociation in the gas phase is a one-electron process. For this reason,

	Chlorobenzene	Benzene
Chemisorbed state	0.98 ± 0.08[a]	0.98 ± 0.06[b]
Physisorbed state	0.52 ± 0.06[c]	0.46 ± 0.01[d]
Physisorbed to chemisorbed state	0.38 ± 0.13[a,c]	0.30 ± 0.03[e]

Table 4.3. The adsorption energy (in eV) of the chlorobenzene and benzene molecules in the chemisorbed state, the physisorbed state and the energy barrier from the physisorbed state to the chemisorbed state. [a]This work. [b]Ref. [191,192]. [c]Ref. [174]. [d]Ref. [192,193]. [e]Ref. [193].

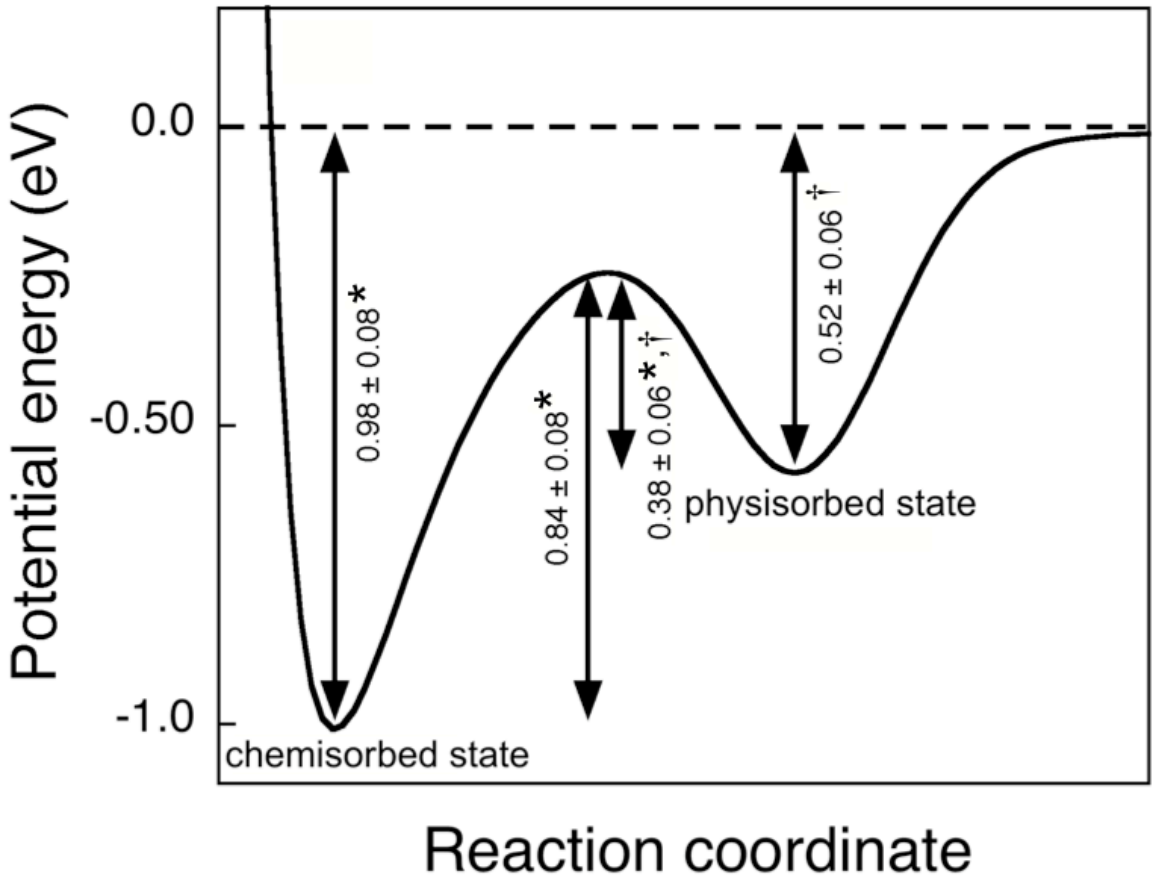

Figure 4.15. Schematic diagram of the potential energy of chlorobenzene on the Si(111)-7×7 showing both chemisorbed and physisorbed states with experimental energy barriers from this work* and from ref. [174]†.

the dissociation of molecules desorbed into the gas phase at the STM junction might be possible using a one-electron process. However, this is unlikely because the energy barrier of desorption E_{des} is higher than that of E_{prom} by 0.2 eV. A physisorbed molecule has less interaction with the substrate than does a chemisorbed one and can preserve the same electronic characteristics as in the gas phase [195-197]. Thus, it is reasonable to assume that the lifetime of the negative ions of molecules at this state is longer than in the chemisorbed state and, therefore, that a one-electron dissociation process as in the gas phase would be allowed. The barrier energy from the chemisorbed to physisorbed states $E_{chem-phys}$ matches the 0.8 ± 0.2 eV activation energy of the one-electron dissociation. A thermal excitation process could promote molecules from the

chemisorbed to the physisorbed state where one-electron dissociation by STM is more efficient than the two-electron process. The dissociation of chlorobenzene in the physisorbed state by STM has been reported at low temperatures [198]. This supports the existence of dissociation at the physisorbed state.

A physisorbed state for adsorbed molecules, which has weak interactions between adsorbates and substrates, can be accessed by dosing molecules at low temperatures, using thin films to decouple substrates from molecules [196,197] or promoting molecules from chemisorption to physisorption such as using thermal excitation in this work. The dissociation of the C-Cl bond in chlorobenzene molecules changes from a two-electron process for a chemisorbed state to a gas phase-like one-electron process for a physisorbed state. This weakly bounded state also preserves the electronic properties of unbounded molecules [196,197] and allows molecules to move freely in a limited range of the surface similar to the random motion of free molecules in the gas phase. This suggests that other dynamic reactions on the surface may evolve the same path as the reactions in the gas phase through the physisorbed state.

Furthermore, the studies of local and nonlocal dissociation of chlorobenzene on Si(111)-7×7 surface were conducted (see Appendix A), where STM tip was fixed at a specific position to inject electrons into particular sites. Nonlocal desorption was also noticed from the experiments. This result provoked extensive studies by our colleague. A detailed investigation has recently been published in Physical Review Letters (Appendix B).

4.7 Conclusions

Investigation of dissociation of PhCl induced by STM at room temperature showed the dissociation of chlorobenzene molecule at room temperature requires 1.4 ± 0.1 electrons. Based on previous work [94], this was interpreted as a mixture of a two-electron temperature independent and one-electron temperature dependent processes. At elevated temperature, the dissociation of molecules showed the enhancement of the one-electron process which is decoupled from the two-electron process. The thermal activation energy of the one-electron dissociation process of 0.8 ± 0.2 eV agrees with the activation barrier of molecular diffusion process of 0.84 ± 0.08 eV. It suggests that the thermally assisted one-electron dissociation process occurs in physisorbed state. This work suggests that other molecular dynamics on the surface may evolve the same path as the reactions in the gas phase through the physisorbed state.

Chapter 5
Molecular switching induced by the STM tip

The extended π-aromatic system 4,4′-dichlorobiphenyl (4,4′-PCB) molecule contains two rings of chlorobenzene which are connected via a C-C bond; it was expected that each ring would adsorb into different states on a Si(111)-7×7 surface, i.e. chemisorption and physisorption. As C-Cl bond dissociation in chlorobenzene can be induced by a two-electron process for molecules in the chemisorbed state and a one-electron process for molecules in the physisorbed state (chapter 4), experiments aiming to induce this dissociation by directly injecting currents at different adsorption states in the same molecules were suggested. Instead of C-Cl dissociation in the molecules, four distinct reactions were induced. One of these produced an unstable adsorbed molecular product, where molecular switching occurred between the two adsorption states. This molecular switching is of interest in relation to nanoelectronics and basic logic devices. In principle, an understanding of the molecular switching mechanism may allow this basic electronic unit to be controlled. Measuring the switching of molecules was conducted by positioning a tip along the molecular regions of that switch the molecules and detecting switching events from changes in the STM junction. Various tip sites and bias voltages were used for these measurements. The experimental results suggested that the switching process was driven by thermal excitation and that the interactions between the tip and the adsorbed molecules generated an attractive force which pulls the molecules to the tip. Molecular rotation was proposed to explain the switching between the two adsorption states.

5.1 Introduction

Polychlorinated biphenyls (PCBs) have a wide range of uses in industrial activities, for example as lubricating and hydraulic fluids, capacitors, insulating and impregnating agents, and as some types of transformers [199]. However, it was found that these chemicals are toxic to the environment and to living animals, including humans. They are thermodynamically stable, making them persistent in the natural environment, including in water and soils. Polychlorinated biphenyls can accumulate in bio-organisms, for example, fish, invertebrates, birds, and mammals [200]. These pollutant chemicals can become widely spread throughout the environment by incorrect disposal or accidents [201,202]. The two important factors which determine the toxicity of PCB congeners are the degree of chlorination and the barriers to rotation about the C-C central bond. Lower barriers (where it is easier to make the molecule coplanar) are related to greater toxicity. In contrast, a greater barrier (where it is more difficult to produce planarization) is related to lower toxicity [203]. Crucially, chlorination can lead to a lower toxicity in PCBs [205]. From the family of PCB molecules we chose 4,4´-dichlorobiphenyl (4,4´-PCB) (see Fig. 5.1 and Table 5.1) because of the symmetric geometry of this molecule. We studied its characteristics on a Si(111)-7×7 surface and its manipulation products after tunnelling a current from an STM tip.

Product name	4,4´-Dichlorobiphenyl
Formula	$C_{12}H_8Cl_2$
Molecular weight	223.1 AMU
Boiling point range	315-319 °C
Melting point range	142-145 °C

Table 5.1. General physical information of 4,4´-PCB [204].

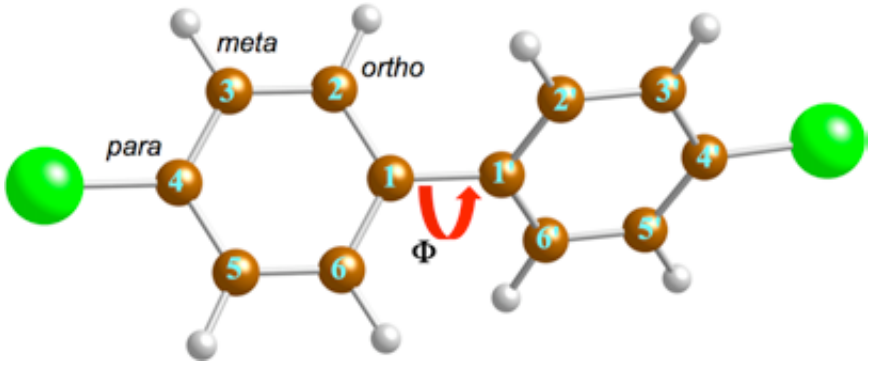

Figure 5.1. Ball and stick model showing the structure of a 4,4´-PCB molecule. The carbon atoms are numbered to indicate the coordinates of each carbon atom. Brown, grey and green balls correspond to carbon, hydrogen and chlorine atoms, respectively.

5.2 Experimental methods

At room temperature, 4,4´-PCB is a solid powder; therefore, it was necessary to evaporate the molecules into the gaseous phase. Initially, 100 mg of the PCB from Sigma-Aldrich was put inside a glass tube of the near ambient temperature effusion cell (NATC) which was attached to the lock-load chamber. Next, we ensured that the molecules and the chamber were both clean from environmental contaminants by outgassing both the doser and the chamber at up to ~ 80-100 °C for several hours until the pressure in the load-lock dropped in range of 5×10^{-7} -1×10^{-6} Torr. It is important to note that the baking time should not be too long since 4,4´-PCB molecules normally escape from the chamber via the pumping process and eventually the whole sample would evaporate. To dose the molecules, firstly the thermostat was set to heat the molecules up to 40-50 °C. As the temperature in the effusion cell rises, the pressure in the load-lock should be less than 5×10^{-6} Torr. Experiments with single molecules required a molecular coverage on the surface of less than 1 monolayer. From trial and error with various dosing parameters it was found that a coverage of 0.015 L produces good conditions for experiments with individual molecules. To create 0.015 L of molecular coverage, the preparation chamber/load-lock valve was opened for 3 seconds at a preparation chamber pressure of 5×10^{-9} Torr during dosing.

5.3 Results and discussion

5.3.1 4,4´-PCB molecules on a Si(111)-7×7 surface

Fig. 5.2 (a) shows various 4,4´-PCB adsorption features on the Si(111)-7×7 surface. Three types of features were observed on the surface: first, there was a stable bright-dark feature (adsorption state-1 or S_1), marked by green circle. The bright lobe in this feature appears brighter at +2 V in Fig. 5.2 (b). Second, the blue circle indicates a stable single dark spot (adsorption state-2 or S_2). Third, the white circle indicates unstable adsorption (adsorption state-3 or S_3) at the bright lobe, implying that this lobe moved very fast. However, this disappears at +2 V in Fig. 5.2 (b). Scanning at the bias voltage of +2 V may desorb some of the features of S_1. Normally, unstable adsorption in both bright and dark lobes can be observed in images (not shown here) after molecular dosing. Due to the stability and the possibility of two rings of adsorption to the surface of the S_1 feature, electron injection experiments were only performed on S_1 features.

5.3.2 Bias dependence of the S_1 feature

The unfilled state of 4,4´-PCB molecules adsorbed on the surface under various positive bias voltages are shown in STM images at a high resolution (image size of 3.5 nm × 3.5 nm) in Fig. 5.3. The blue lines linking two of the middle adatoms mark the location of molecular adsorption. Bright lobes and dark lobes were observed at the two ends of these lines. The bright lobes appeared to be brighter when the bias voltage was increased. On other hand, there was no significant change observed in the appearance of the dark lobes as the voltage varied. The bias voltage was restricted to +1.5 V since scanning at +2.0 V or above can cause molecular desorption.

Fig. 5.4 shows the unfilled states of the S_1 adsorption feature with a positive bias voltage and a negative bias voltage. In the negative bias voltage images, (c)-(d), the filled states of the adsorbate, i.e. π-state, were revealed. The bright appearance of the molecule in the positive bias

voltage slightly darkened in the middle adatom. In contrast, there was no significant difference in the dark spots for both polarities.

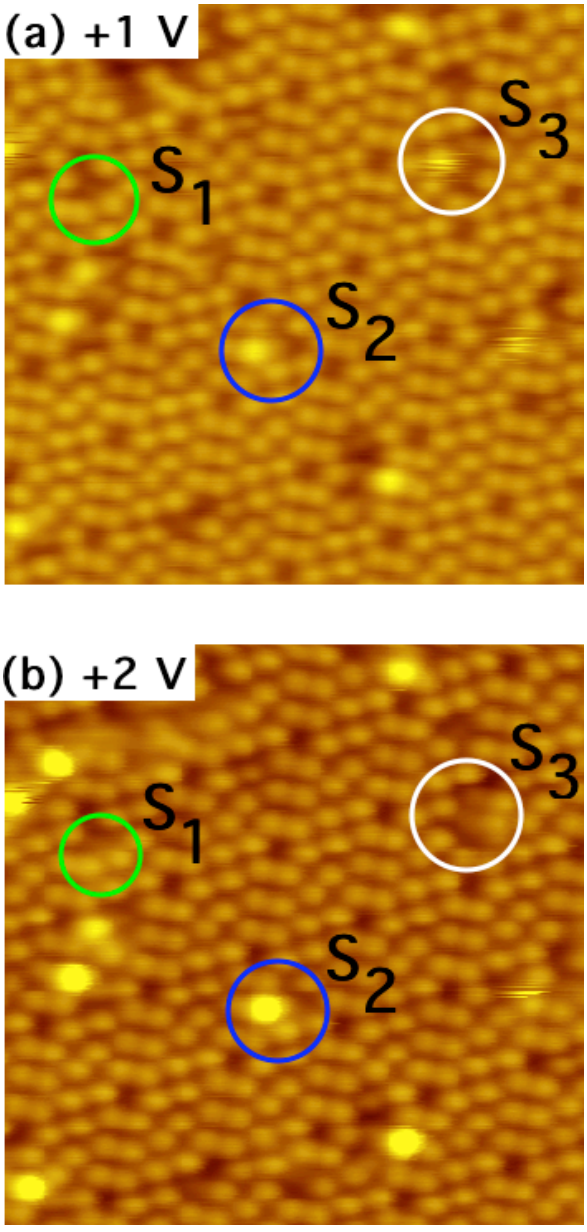

Figure 5.2. STM images after exposing 4,4′-PCB molecules to a Si(111)-7×7 surface, taken with (a) +1 V and (b) +2 V, 100 pA, image size 12 nm × 12 nm. Blue, green and white circles mark the locations of a bright-dark feature (S_1), a single dark feature (S_2) and an unstable feature (S_3).

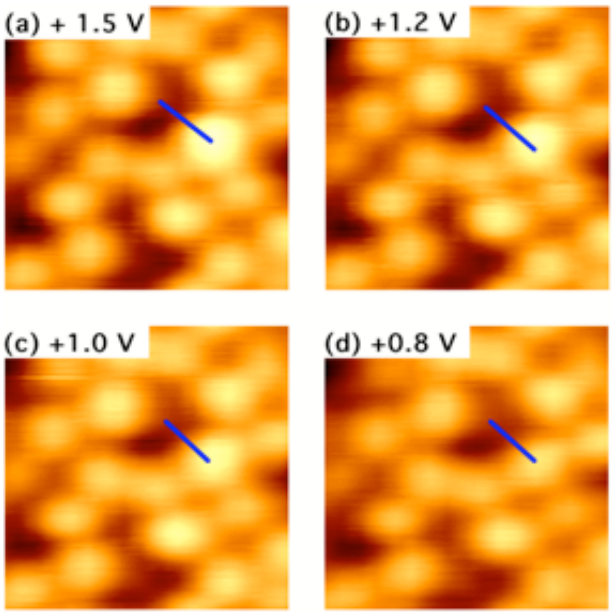

Figure 5.3. The S_1 adsorption feature of 4,4′-PCB on the Si(111)-7×7 surface at various positive bias voltages (a) to (d) (+1.5 V to +0.8 V) with 80 pA and an image size of 3.5 nm × 3.5 nm. The blue lines mark the locations of a molecule aligning on the surface.

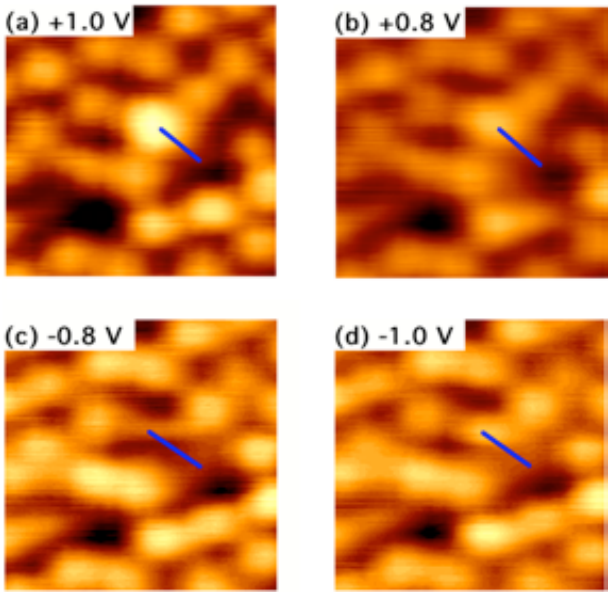

Figure 5.4. The S_1 adsorption feature of 4,4′-PCB on the Si(111)-7×7 surface at positive, (a) +1.0 V and (b) +0.8 V, and negative bias voltages, (c) -0.8 V and (d) -1.0 V, with 80 pA and an image size of 3.5 nm × 3.5 nm. The blue lines mark the locations of a molecule aligning on the surface.

5.3.3 Molecular adsorption configuration of the S_1 feature

There have been no experiments or calculations on the adsorption configuration of PCB molecules on the Si(111)-7×7 surface. However, based on our positive bias STM images a possible molecular adsorption model can be proposed. Fig. 5.5 (a) shows a high resolution STM image of the S_1 adsorption feature on a clean silicon surface. The appearance of the dark lobe, resembling a missing adatom, is possibly due to a ring of molecules, similar to chlorobenzene molecules (called "chemisorption"), bonding to a silicon adatom and resulting in saturation of the dangling bond. This was also observed in the adsorption of benzene [206] and chlorobenze [174] on the Si(111)-7×7 surface. The rest atoms near the saturated middle adatom may be involved in molecular adsorption similar to chlorobenze/Si(111)-7×7 adsorption [174]. However, from the voltage dependence images there is no evidence of the rest atoms bonding with the adsorbed molecules. The bright lobed feature of the molecule is possibly another half of this molecule. Since it is bright, this suggests that this part of the molecule does not bond with the surface adatoms (called "physisorption", which may be similar to benzene physisorption [194]). This bright lobe feature may come from chlorine atom locating in physisorption, which is absent for chemisorbed chlorobenzene. A proposed configuration of the adsorption of 4,4′-PCB molecules is shown in Fig. 5.5 (b). This shows that the dark lobe is a chemisorbed ring attached to the middle adatom and the rest atom around it, anchoring the whole molecule to the substrate, whereas the bright lobe is a physisorbed ring. Many experiments and calculations have been performed to investigate the structure of the 4,4′-PCBs molecule [205,207-219]. Table 5.2 displays bond lengths and torsion angles with respect to PCB in Fig. 5.1.

Given that the distance between the carbon atom (4-carbon atom) at the end of one side of the molecule to the other end (4′-carbon atom) is ~ 6 Å and the distance between adjacent adatoms is approximately 7.7 Å, our proposed geometric adsorption structure seems to agree with the appearance of the molecular adsorption shown in the STM images. Although the carbon atoms at positions 4 and 4′ do not attach to the middle adatoms, the STM images reflect molecular orbitals at the molecular adsorption sites which take up more space than the schematic picture of the 4,4′-PCB molecule.

	Experimetal[a]	B3LYP/6-311+G(d,p)[b]
C_1-$C_{1'}$	1.494	1.484
C_1-C_6	1.405	1.402
C_6-C_5	1.385	1.392
C_5-C_4	1.401	1.391
C-Cl	1.736	1.758
$\Phi(C_6\text{-}C_1\text{-}C_{1'}\text{-}C_{6'})$	45.2 ± 1.5	40.4

Table 5.2. Experimental and calculated geometries of the 4,4′-PCB molecule (bond distances in Å, angles in degrees °). The atom numbering corresponds to Fig. 5.1. [a]Ref. [205], [b]Ref. [219].

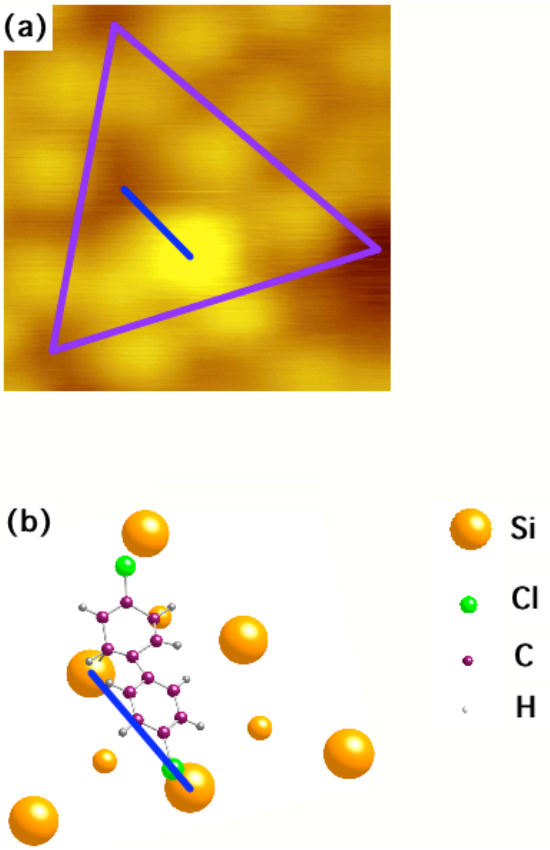

Figure 5.5. (a) STM image of the S_1 adsorption feature of the 4,4′-PCB molecule, taken with +1.5 V and 100 pA, with an image size of 3.24 nm × 3.24 nm. (b) Schematic adsorption configuration of the 4,4′-PCB molecule corresponding to half of a cell unit in (a). The large silicon atoms represent adatoms. The small silicon atoms show rest atoms. The blue line marks the location of the molecule between a pair of middle atoms.

5.3.4 Molecular reactions induced by STM current injection

As was found during normal STM imaging, the S_1 adsorption feature of 4,4´-PCB can be modified when imaged above a bias voltage of +2 V. To investigate this molecular manipulation induced via STM, pulses of electron injections from the STM tip were applied at a precise position inside the S_1 feature in attempt to dissociate the molecules and the outcomes were recorded. Two specific sites inside the PCB molecule were targeted for electron injection, i.e. the bright and dark lobes. In these experiments, the current was injected into the centre of the chosen lobe for a certain period of time (2 to 5 seconds) and at a constant current. Changes in adsorbate configuration underneath the STM tip can be monitored via changes in the topography as a function of time. However, almost all of the reactions occurred during voltage ramping to the set point. Thus, no changes were found in the time tracing of the topography after ramping. Current injections into the bright and dark lobes of single molecules were performed at bias voltages of 3.2 to 4.0 V for the bright lobe and 3.0 to 4.0 V for the dark lobe as these are above threshold voltage of C-Cl bond dissociation in chlorobenzene [93], and a tunnelling current of 80-150 pA was applied for 3 seconds.

The results from the electron injections into the physisorbed and chemisorbed rings were classified into four types:

Type I S_1 desorption: Injecting the pulse of current through the bright lobe induced desorption of the molecule (marked by green dot in Fig. 5.6 (a)). This phenomenon can be observed as a disappearance of the S_1 feature after manipulation, revealing a clean silicon surface such as the one shown in Fig. 5.6 (b). The molecule directly underneath the tip was desorbed and a few dark lobes at a distance from the injection point were also desorbed. This may suggest non-local processes affecting molecules at a distance from the injection site (described in more detail in Appendix A). Desorption was also found when a current was injected into the dark lobe (Fig. 5.7 (b)).

Type II Bright-dark (S_1) to dark-dark (S_4): By injecting electrons into the bright lobe of the molecule in Fig. 5.6 (c). The bright lobe of the molecule, considered to reflect physisorbed adsorption, was converted to a dark lobe neighbouring to the chemisorbed ring on the surface shown in Fig. 5.6 (d). This S_4 feature is very stable since efforts with a current pulse to induce the molecule to desorb, diffuse or convert back to S_1 feature again failed. Therefore, the dark-dark feature is probably the most stable adsorption configuration of this molecule. Again, this reaction also occurred with injections into the dark lobe (Fig. 5.7 (c) and (d)).

Type III Bright-dark (S_1) to single-dark spot (S_2): Fig. 5.6 (e) and (f) show electron injections into the bright lobes of the molecule resulting in the disappearance of these bright lobes. This was also observed with injections into the dark lobes (Fig 5.7 (e) and (f)).

Type IV Bright-dark (S_1) to dark-bright (S_5): The bright lobe was converted to a dark lobe whereas the dark lobe converted to a bright lobe by injections into the bright lobes, as shown in Fig. 5.6 (g) and (h). The dark-bright product is not stable. The bright lobe can change adsorption sites from one middle adatom to another and vice versa while the dark lobe is fixed.

There were four distinct reactions after electrons were injected into the molecules. No C-Cl dissociation was observed in any of the experiments. As the induced PCB reactions (I to IV) from the S_1 feature only occurred when the voltage of the current injection applied was above 1.5 V, the threshold voltage for these reactions is above 1.5 V. The existence of a voltage threshold suggests that these PCB reactions are driven by electronic excitation, similar to results reported in previous works such as the desorption of benzene on Si(100)-2×1 [92], the dissociation of oxygen on Pt(111) [91] and the dissociation and desorption of chlorobenzene on Si(111)-7×7 [94,95]. The desorption mechanism of PCB (Type I) may resemble that of benzene desorption [92], where the energy of the bending mode of the benzene ring transfers to the stretching vibrational mode of the molecule-surface bond (C-Si). Excitation in other vibrational modes would lead to different reactions (Types II to IV). For example, in the S_4 feature (in Type II), two rings of PCB molecules possibly chemisorb to the silicon surface equally, and both rings are planar to each

other. This planarity of the 4,4′-PCB molecule is consistent with the calculated negative ion structure of biphenyl molecules in the gaseous phase [211]. According to our proposed S_1 adsorption feature, the physisorbed ring (bright lobe) needs to be twisted around the centre inter C-C bond to be in same plane as the chemisorbed ring ($\Phi = 0°$). In the gaseous phase, the torsion barrier height of the 4,4′-PCB molecule from the optimized torsion angle (~ 40°) to zero torsion angle is ~ 85-92 meV [205,209-210,214]. Dissipated energy in inelastic tunnelling electrons via vibrational excitation in particular modes could be enough to overcome the energy of this torsion barrier. In Type III, the S_2 feature may come from breaking of the centre inter C-C bond by vibrational excitation of this bond. This bond dissociation can generate adangling bond at the carbon atom on the chemisorbed ring, causing it to be unstable. As this chemisorbed ring has a dangling bond from the C-C bond breaking, this chemisorbed ring would become more stable if this dangling bond was saturated by bonding with the silicon atom, and the whole ring would stand perpendicular to the surface plane. Another possible configuration is the bright lobe changing its orientation from adsorbing parallel to the surface to standing vertically on the surface, like in the azobenzene molecule induced by electrons [134]. Most of the induced reactions were Type I to IV reactions. The two flat rings adsorbed onto the surface (S_4 feature) from the Type II reaction are a perfect candidate for exciting vibrational modes in the molecular dissociation. However, this dark-dark feature was very stable. Although current pulses were injected into the dark lobe product, no change from the S_4 features was observed.

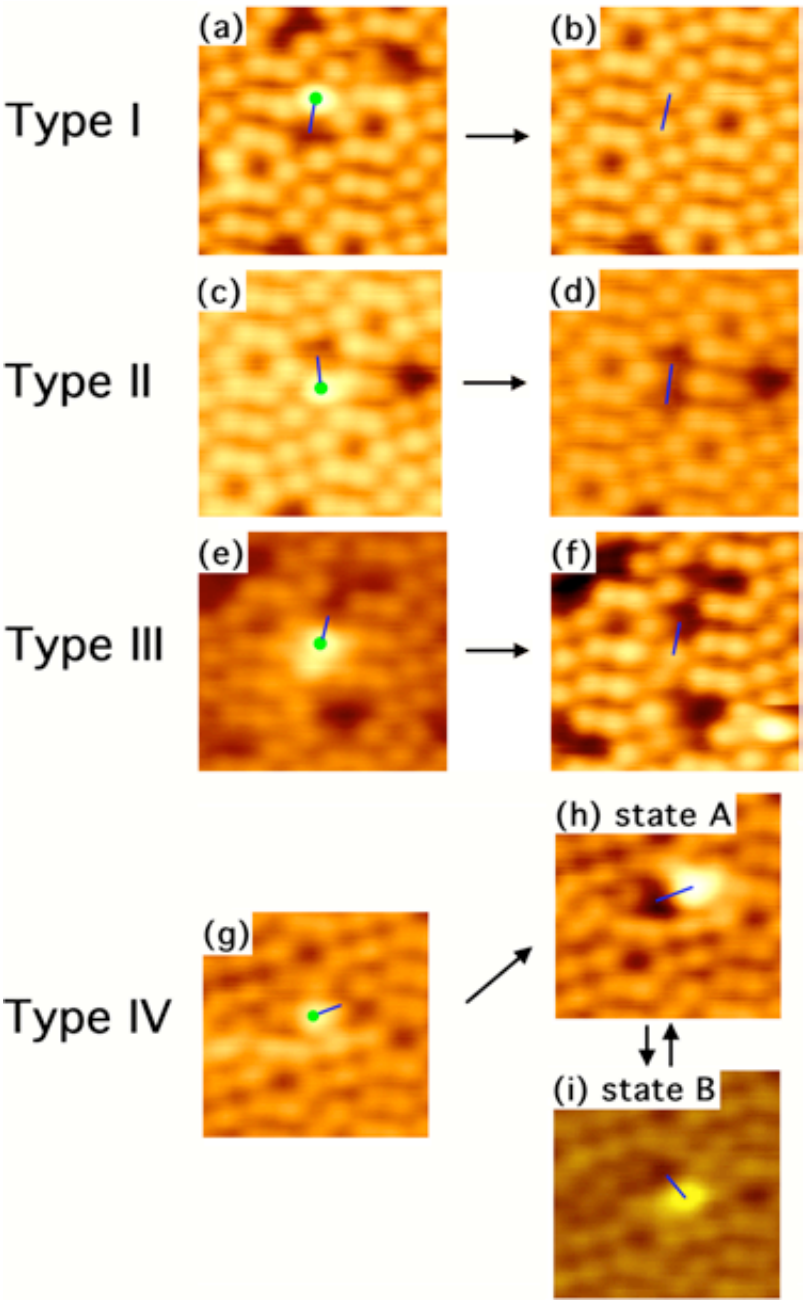

Figure 5.6. STM-induced molecular reactions by electron injection into the bright lobe of the 4,4′-PCB molecules. (a), (c), (e) and (g) were taken before injection, and (b), (d), (f), (h) and (i) were taken after injection, corresponding to the induced reactions of Types I-IV. The green dots represent the injection positions into the bright parts of the molecules. The blue lines mark the location of molecule adsorption. (a)-(i) Images taken at +1 V, 80 pA, (a)-(f) images with a scanning size of 5.5 nm × 5.5 nm, (g)-(i) images with a scanning size of 5 nm × 5 nm.

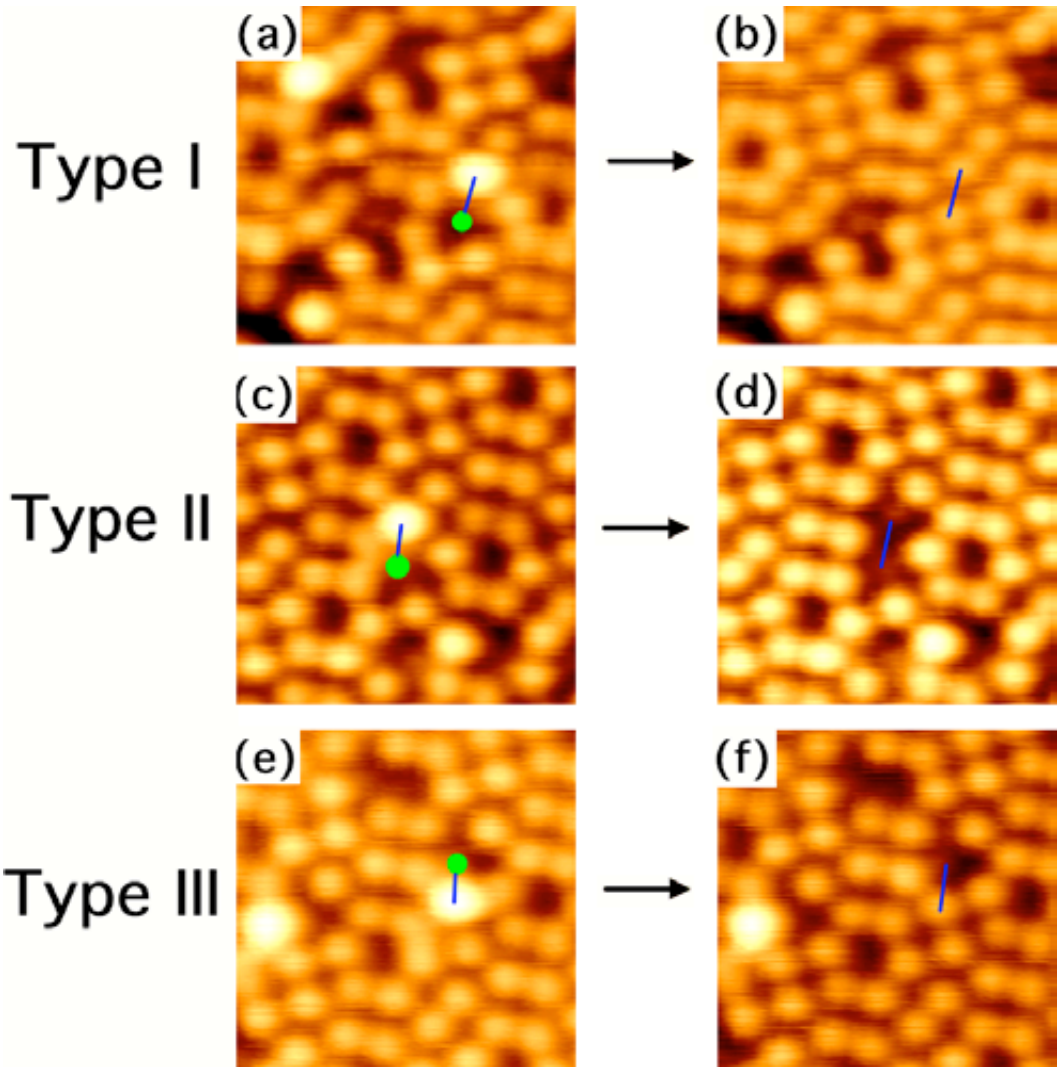

Figure 5.7. STM-induced molecular reactions by injections into the dark lobes of the 4,4′-PCB molecules; (a), (c), and (e) are images taken before injection, and (b), (d) and (f) are images taken after injection, corresponding to the induced reactions of Type (I)-(III). The green dots represent the injection positions into the dark lobes of the molecules. The blue lines mark the location of molecular adsorption. Each image was taken at +1 V and 80 pA with a scanning size of 5.5 nm × 5.5 nm.

5.3.5 STM-tip induced molecule switching

The reversible processes of isolated molecules and molecular self-assembly, mostly azobenzene derivatives [135,138,220-225] on solid surfaces, including, isomerisation and conformational changing, as triggered by electrons [135,138,220-223], light [224] and electric fields [136,225], have used STM as a prototype of molecular electronic devices [9,11,226]. Understanding the switching mechanism is important for control over these atomic scale switching processes. From four possible STM-induced reactions, we chose to study the bi-stable adsorption of 4,4′-PCB on a Si(111)-7×7 surface (Type IV reaction) to gain a greater understanding of the switching mechanism. This main part of the chapter will focus on atomic manipulation in the preparation of the bi-stable molecular switch, measurements of molecular switching at various tip sites and discussions about the STM tip effect on the molecule switching mechanism.

5.3.5.1 Bistable adsorbed molecule preparation

Generally when molecules from the gaseous phase land on a surface they search for the most favourable adsorption sites. The molecules stay in a pre-cursor state before finding a stable adsorption site. Hence, it is rare to observe meta-stable molecules on the surface. It was found that biphenyl (BP) molecules exhibit bi-stable adsorption on a Si(100)-2×1 surface at room temperature [96]. Thermal excitation was suggested as driving the molecule to switch between the two adsorption sites. Biphenyl is therefore stable at a low temperature (5 K). At this low temperature, STM induced these BP molecules to switch their adsorption sites [104]. As the geometric structure of BP resembles PCB, 4,4′-PCB molecules may inherit the bi-stable adsorption characteristics of the BP molecule, even on a different silicon surface. Unlike BP, 4,4′-PCB only adsorbs in a stable configuration at room temperature; however, it can be manipulated into a bi-stable state with the resulting thermal drive inducing tip-dependent switching. This bi-stable molecule adsorption state can be induced during either scanning or direct current injection.

Method I Scanning

This process does not always result in bi-stable state molecules in the same position as the original stable molecules. After scanning, the adsorbed molecules sometimes diffuse a few unit cells from their initial positions and then undergo bi-stable adsorption at a new, clean site. Fig. 5.8 shows consecutive scanning images of two states of a bi-stable adsorption molecule. The molecule flips from site A to site B and vice versa during scanning with a range of imaging parameters (+1 to + 2 V, 80 pA).

Method II Current injection at fixed position

The principle behind this technique of injecting into the bright lobe is that it can induce a see-sawing of the adsorption state (Type IV reaction). For a better chance of creating unstable switching molecules and to avoid inducing other kinds of reactions, a bias voltage above +2.0 V and a short injection time of ~ 0.5 seconds were repeatedly applied to the bright lobe until it triggered new molecular states. Some of these were in the bi-stable state, appearing as switching molecules in the series of STM images. The ring that was “physisorbed” became “chemisorbed” and the “chemisorbed” ring became “physisorbed”, exactly like a rocker light switch. It is at this new adsorption configuration, superficially similar to the pre-manipulation configuration, that we observed bi-stability. The site of the new chemisorbed ring is located in the same position of the previous physisorbed ring and the new physisorbed ring hops between the two adsorption sites (see Fig. 5.6 (g)-(i)). Movement of the new physisorbed ring is a reversible process which can be observed in sequential scanning images, like the molecules induced by the scanning process.

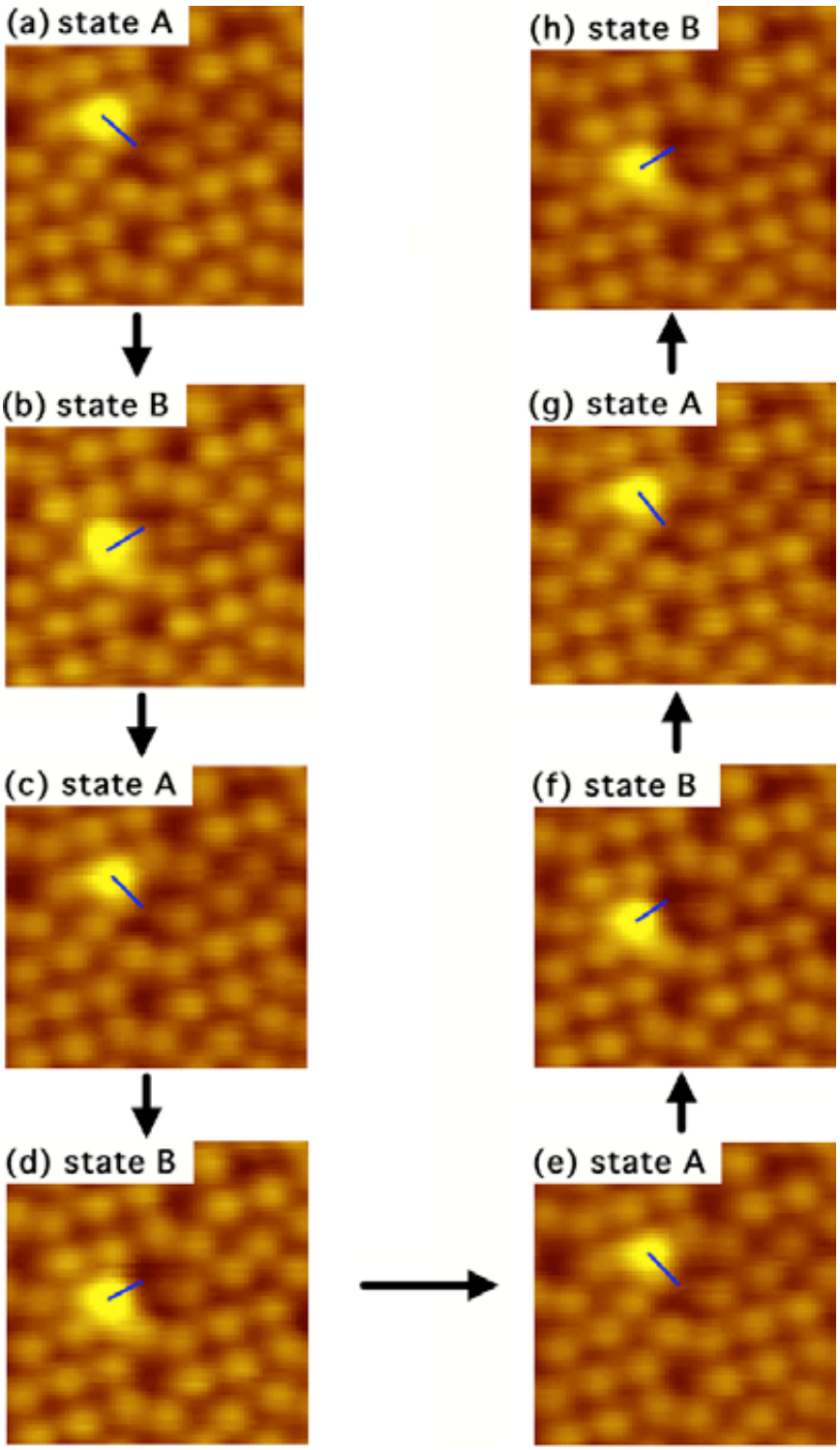

Figure 5.8. Series of consecutive scanning images showing molecular switching between two adsorption states (state A and state B). Each image was taken at +1.5 V and 80 pA with a size of 5 nm × 5 nm.

5.3.5.2 Tip-dependent molecular switching

It is important to understand which mechanism activates the molecules to switch as this may allow us to control the switching. Investigations of switching can be performed by employing electron injections at a specific site. Electron tunnelling was used to track the time molecules spent in particular states in order to calculate the switching rate. Two parameters in this time-tracking measurement, bias voltage and injection site, were varied to observe the relationship between the two factors in switching, for example the threshold of switching. For this measurement, bias voltages of 1.0 V to 2.2 V were applied. The maximum bias voltage was limited at 2.2 V. Injections into the bright lobe site after 2.3 V usually transformed a molecule into an S_4 species. Eight points aligned in the same line across middle of the bright lobe of two states, as shown in one measurement set in Fig. 5.9 (a) were selected. Fig. 5.9 (b) shows the measurement results acquired from two sites, site 3 and 6. At site 3 the tip is on the middle of the bright lobe of the A state. No change in Z-height, the topography height at the measured point, occurred, as displayed in the constant blue line in (b). This indicates that no switching event occurred, which corresponds to the lack of changes in the STM image before the tip scanning approach to the site and after tip scanning passed the site (scanning from top to bottom). The bright lobe of the molecule was always underneath the tip during measurement. When the tip took measurements at site 6, there was a sharp increase in Z-height, as shown by the red curve in (b). The sharp increase in Z-height indicates the point at which switching occurred. Physically, increasing the height implies that the tip moves further away from the surface. This means that the bright lobe was moved from another adsorbed site (site 1 to 4 i.e. state A) to the site underneath the tip (site 5 to 8 i.e. state B). This sudden change also can be seen in the scanning line at site 6. By collecting the times that the bright lobe spent in each state at each tip site, the switching rate at each tip site can be calculated. The analysis program used here was written by Dr. Peter A. Sloan.

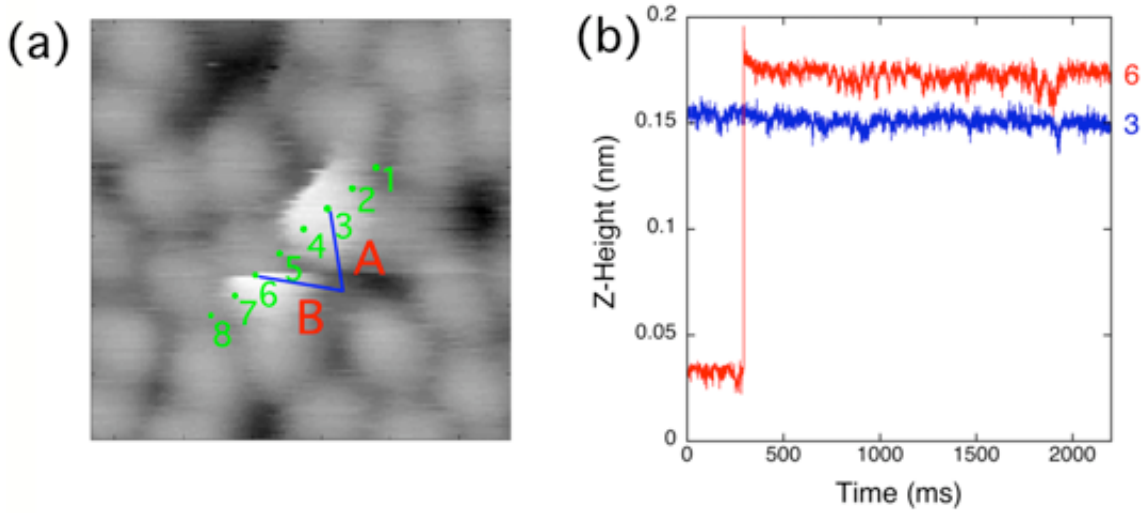

Figure 5.9. (a) Eight sites of switching rate measurements across two molecular adsorption states. The blue lines show the molecule adsorption alignment of states A and B. (b) The two measured Z-heights acquired at points 3 and 6. Switching of the molecule was detected in a sharp changing curve when the tip was at point 6, corresponding to the shifting of the molecule from the tip-allocated sites 1 to 4 (state A) to sites 5 to 8 (state B). No change in the Z-height measurement was observed when the tip was at site 3, corresponding to no movement of the molecule.

There were two directions of switching: state A to B and state B to A. Calculating the switching rates in both directions gave interesting insights into the influence of the tip on the switching process, such as preference of switching direction. For molecules switching from state A to B, the molecule was initially at state A, then it switched to state B. The switching rate from A to B (R_{AB}) was calculated from:

$$R_{AB} = \frac{n_{AB}}{t_A} \tag{5.1}$$

where n_{AB} is the number of switches from A to B and t_A is the total time of the molecule in state A. Fig. 5.10 (a) shows a 3D diagram of the switching rate from A to B dependent on voltage and tip site. When the tip was at site A (sites 1 to 4) i.e. the same site as the molecule, there was no

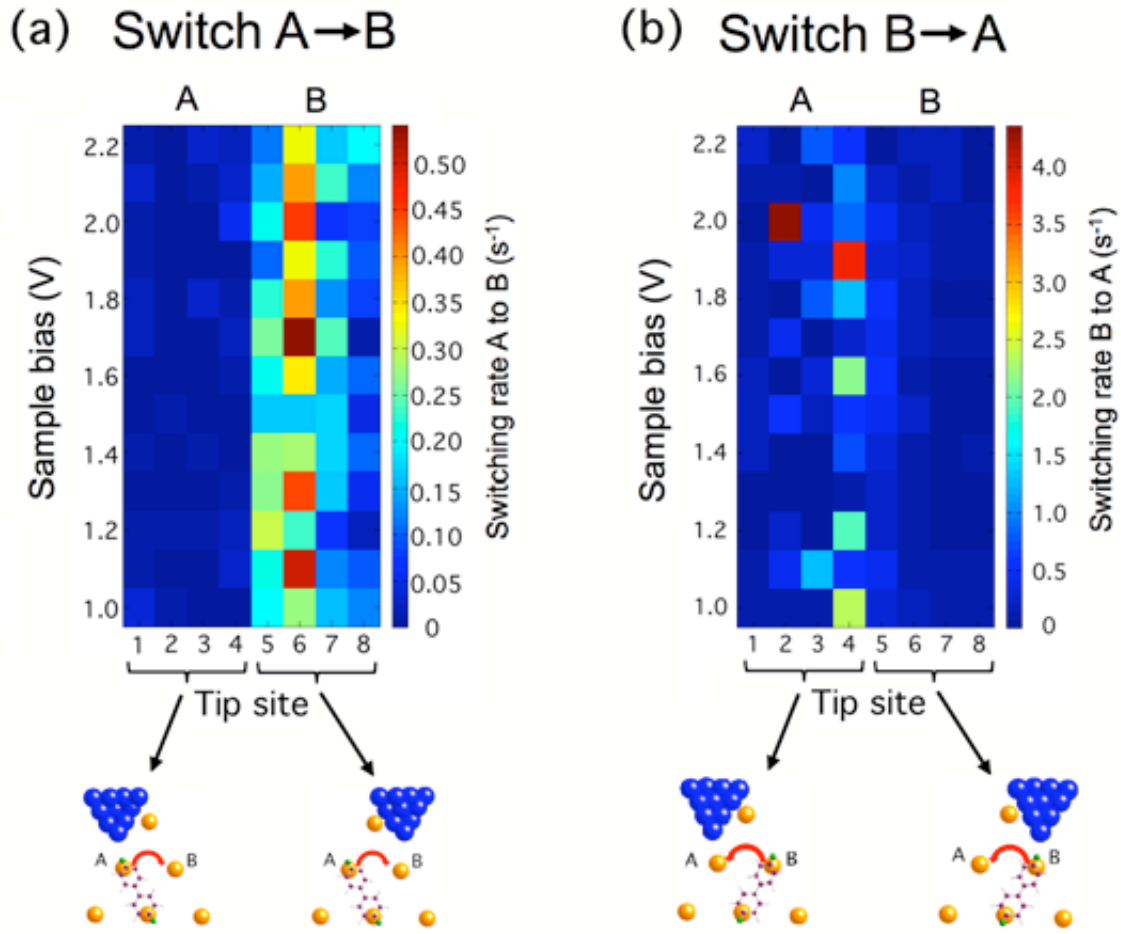

Figure 5.10. Three-dimensional diagram showing voltage and tip site dependent switching rates from (a) state A to state B and (b) state B to state A. Eight sites for tip measurements were determined, as shown in Fig. 5.9 (a).

switching of the molecule from A to B. In contrast, when the tip moved to state B (sites 5 to 8) while the molecule was still in state A, switching of the adsorption site of the molecule from A to B was observed. The highest switching rate occurred when the tip was at site 6, located in the centre of the bright lobe of the molecule. A similar trend was observed for the molecule when switching from state B to A, as shown in switching rate from B to A (R_{BA}) in Fig. 5.10 (b). In this case, switching only occurred when the tip was at state A, especially when the tip was at sites 2 and 4. The switching rate from B to A (R_{BA}) was higher than from A to B (R_{AB}) by a factor of

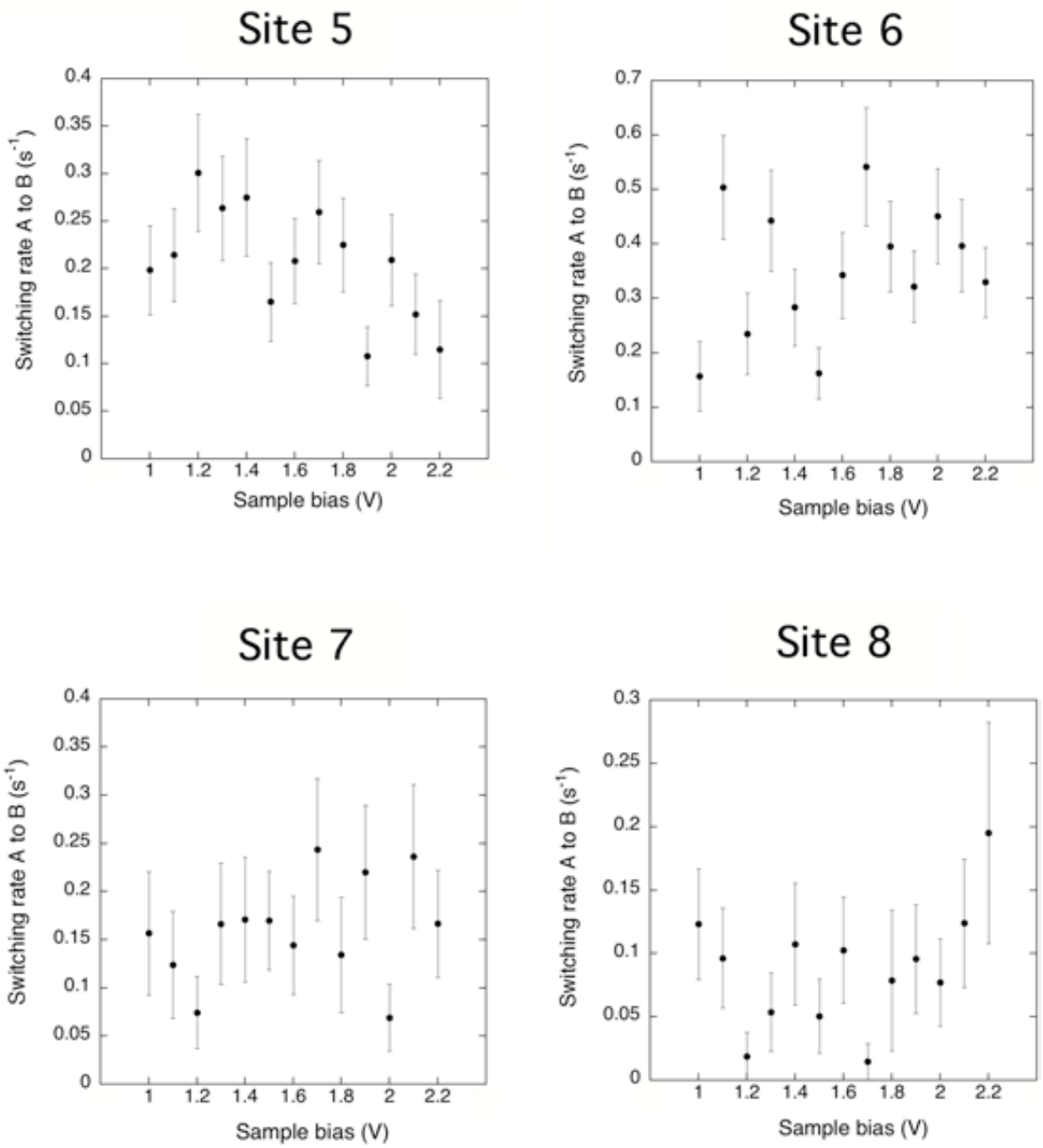

Figure 5.11. Switching rate from state A to state B from measurements at unoccupied molecule site 5 to site 8. There is no voltage threshold or voltage dependence from tip sites. 40 measurements were performed at each sample bias voltage. Error bars were determined from Poisson distribution.

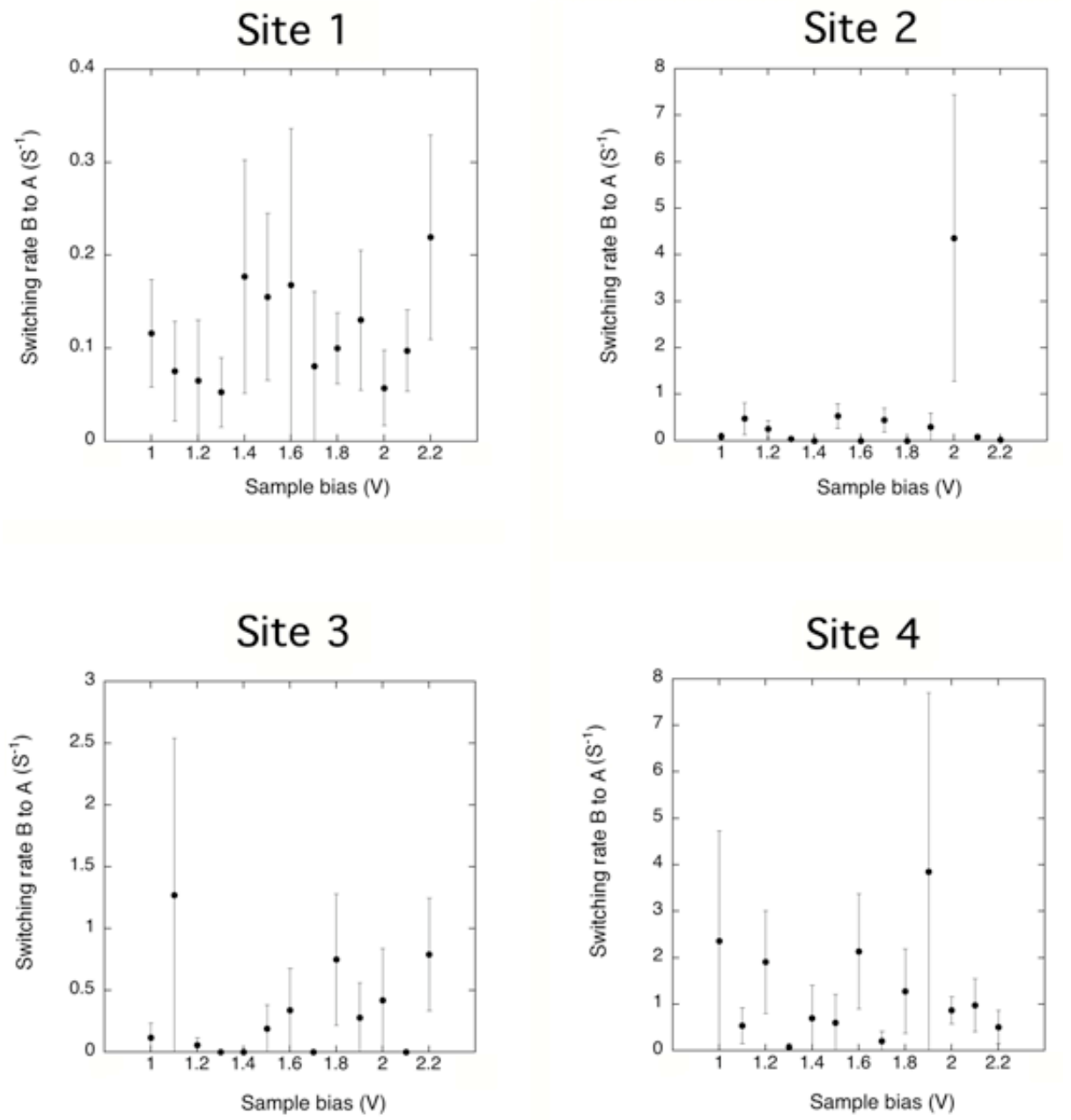

Figure 5.12. Switching rate from state B to state A from measurements at unoccupied molecule site 1 to site 4. There is no voltage threshold or voltage dependence from tip sites. 40 measurements were performed at each sample bias voltage. Error bars were determined from Poisson distribution.

10. Fig 5.11 shows switching rates from state A to state B at specific tip sites from the data shown in Fig 5.10 (a) at tip site 5 to 8, unoccupied molecule sites, where the molecule prefers to switch. Fig 5.12 presents switching rates from state B to state A from the data shown in Fig 5.10 (b) at the unoccupied molecule site 1 to 4. No voltage threshold and no voltage dependence were observed in either switching direction.

As there was no bias voltage dependence of switching, switching could possibly be driven by thermal excitation at room temperature. The energy barrier ($E_{barrier}$) of switching at a particular tip site can be calculated from the Arrhenius equation:

$$R = v_0 \exp\left(\frac{-E_{barrier}}{k_B T}\right) \tag{5.2}$$

where R is an averaged switching rate at particular tip site calculated from all experiments of particular voltages in one direction (s^{-1}), v_0 is the attempt frequency, assumed to be 10^{13} s^{-1}, k_B is the Boltzmann constant and T is the temperature of a substrate at room temperature. Thus, the switching barrier ($E_{barrier} = -k_B T \ln\left(\frac{R}{v_0}\right)$) can be plotted according to tip site dependence, as displayed in Fig. 5.13 (a) for the switching from state A to state B and Fig. 5.13 (b) for switching from state B to state A. The barrier energy of switching from state A to state B was ~ 80-95 meV and from state B to state A it was ~ 75-85 meV. The asymmetry of the switching barrier indicates that there was a preferred adsorption site of the molecules, which was state A with lower energy of ~ 5-10 meV with respect to state B. The attempt frequency at both states may not be equal to 10^{13} s^{-1} and not need to be identical. The unbalance of the attempt frequency seems consistent with our proposed asymmetric switching adsorption configuration at the end. However, we considered only the case of equality on both states of attempt frequency of 10^{13} s^{-1}.

Here, the energy barrier by varying tip position is considered. For switching from state A to state B, the molecule was initially at state A, occupying the space for the measurement of tip sites 1 to 4. The energy barrier at tip sites 1 to 4 (molecule underneath the tip) was ~ 90 meV, whereas it decreased to ~ 80 meV for the tip measurements on sites 5 to 8 (no molecule

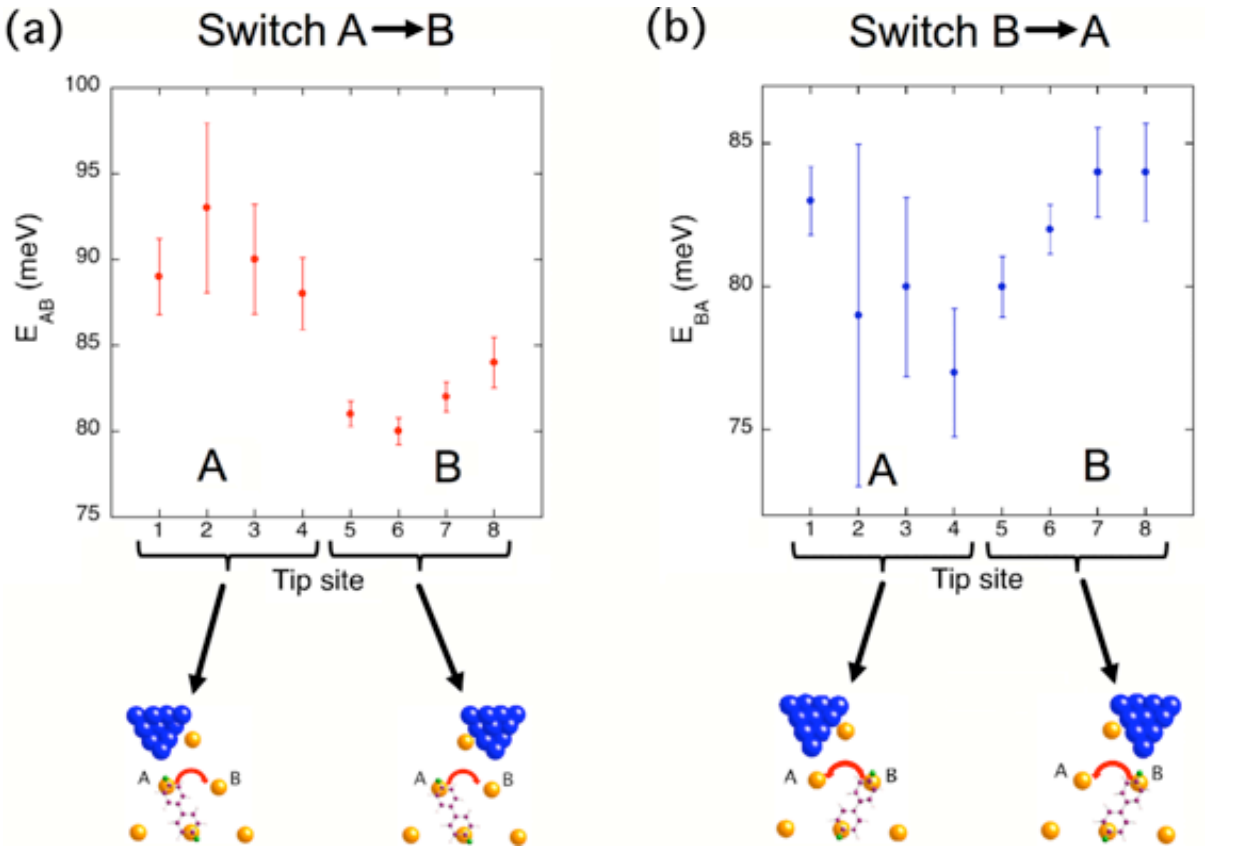

Figure 5.13. Energy barriers for molecular switching (a) state A to state B (E_{AB}) and (b) state B to state A (E_{BA}) at each tip site.

underneath the tip). The same trend of the decreasing energy barrier was seen for switching from state B to state A, where the most of energy barriers for the tip site 1 to 4 is less than site 5 to 8. It can be seen that the molecule followed the tip as switching occurred only when the tip was on an unoccupied site. This suggests that there was attractive force, such as an electric field, and molecule-tip interactions, pulling the molecule to the tip. According to the dipole moment of the C-Cl bond on the moving ring and the negative voltage applied to the tip, the electric field was likely to be the main force governing the switching direction by lowering the potential barrier. This was found to be the case for guiding the hopping direction of CH_3S molecules on a Cu(111) surface [150], where the hopping was induced via a vibrational excitation process. However, there is no voltage dependence in PCB switching rate. This suggests that the electric field may

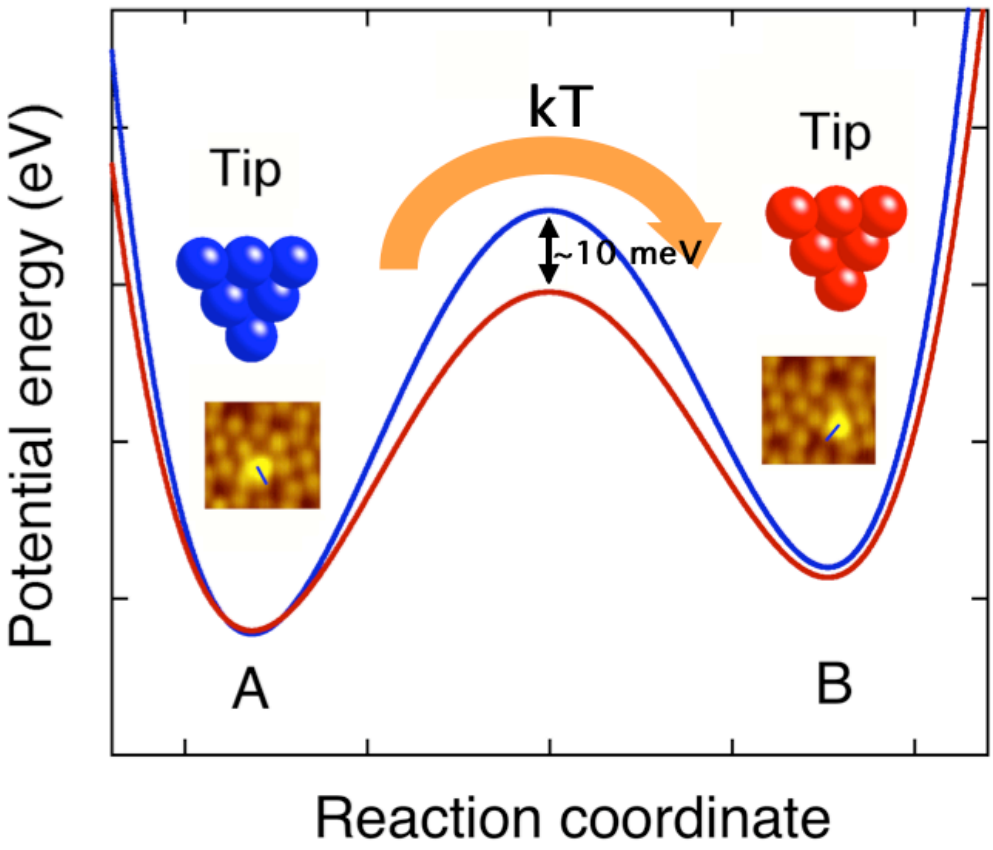

Figure 5.14. Schematic of the potential energy curves present at the STM tip which reduced the energy barrier of the molecule switching from state A to state B. The blue curve shows the potential energy of switching when the tip (site A) was presented with the blue tip and the molecule was in same state (site A). The red curve shows is potential energy of switching when the tip (site B) was presented with the red tip and the molecule was not in same state (site A), resulting in the molecule changing state underneath the tip (site B).

not be the main force to govern switching. Thus the tip-molecule interactions possibly play a major role for controlling molecule switching.

Fig. 5.14 shows a schematic diagram of the reduction in energy for potential switching from state A to state B. When the tip was on same site as the molecule (blue tip), the energy barrier of switching to state B, E_{AB} (blue curve) was still high, making it difficult to induce switching. When the tip was moved to the opposite site on the molecule (red tip), E_{AB} was

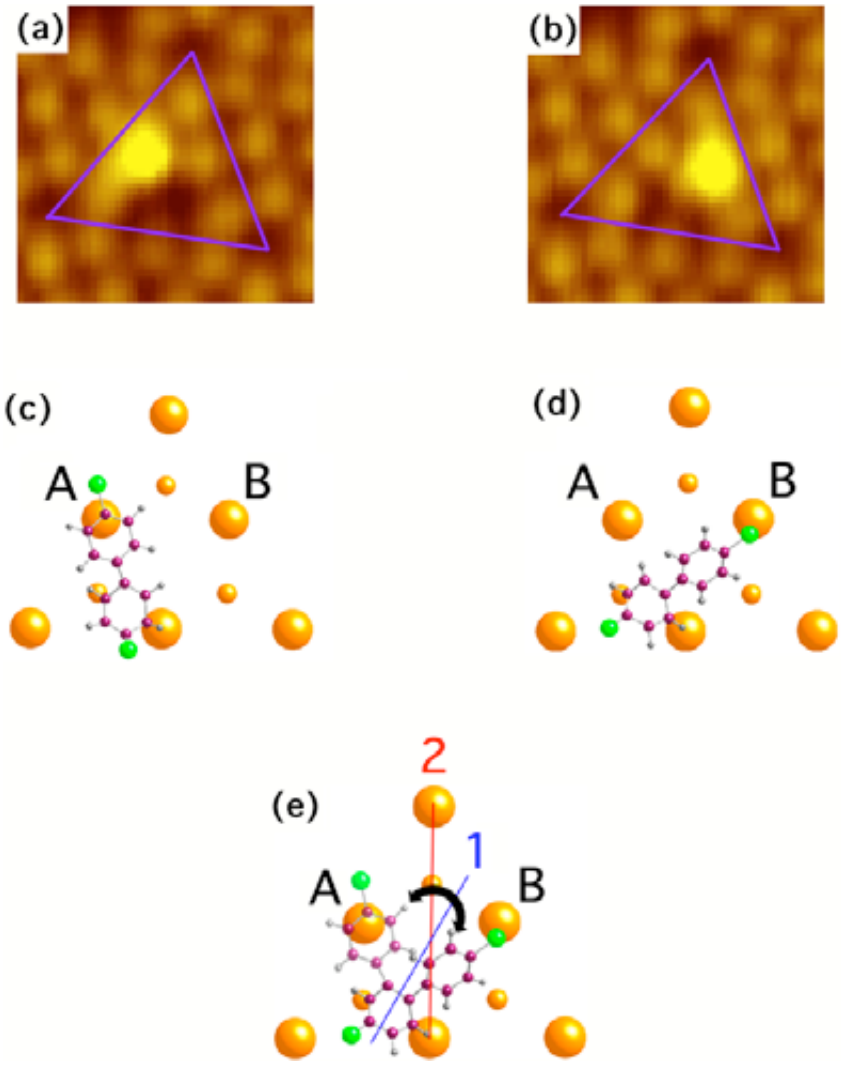

Figure 5.15. Molecular rotation model. The STM images of a molecule at state (a) A and (b) B. Purple triangle locates a half unit cell. (c) Molecule adsorption at state A. The chemisorbed ring bonds to adjacent adatoms and rest adatoms while the physisorbed ring is unbound. (d) Molecule adsorption at state B. The molecule rotates ~60° from state A, resulting in the physisorbed ring moving to weakly adsorb neighbouring middle adatoms at state B. (e) Movement of the physisorbed ring between the two states, only showing the changing position of the physisorbed rings. The transparent model displays the physisorbed ring on state A. The solid model displays the physisorbed ring on state B. The blue line (1) represents the axis of the symmetry of switching between states A and B. The red line (2) represents one of the symmetry axes of a half unit cell.

reduced by ~ 10 meV (red curve), leading to increase in switching rate by thermal excitation at room temperature. The well at state A was deeper than at state B by ~ 5-10 meV, making state A the preferred state for the molecule.

Although the dynamics of the molecular configuration during switching is unknown, we considered a possible adsorption structure model. It was noticed that the molecular adsorption at state A (Fig. 5.6 (h)) was not symmetrical to the adsorption at state B (Fig. 5.6 (i)). There is a protruding part of the bright lobe of molecule at state A, slightly out of half unit cell, positioned above the dimer rows, whereas the bright lobe of the molecule at state B did not protrude.

This may mean that state B had a weaker interaction with the surface atoms than state A. It would also explain the greater stability of state A with respect to state B. Based on our adsorption configuration of the molecule for S_1 in the previous section, we suggest that the adsorption configuration of the molecule at both states was similar to S_1. The adsorption configurations of state A and state B, as found in our observations, are shown in the schematic diagram in Fig. 5.15 (c) and (d) corresponding to STM images in Fig. 5.15 (a) and (b). A fixed chemisorbed ring was attached to a pair of adjacent middle adatoms and rest atoms by 2,5 di-σ bonds, the same as chlorobenzene chemisorption on the Si(111)-7×7 surface [174], whereas the other ring was not bound. The molecular adsorption at state B had a molecule axis angle of ~ 60° with respect to that of state A (see Fig. 5.15 (e)). We propose a "molecular rotation" model to elucidate the movement from state A to state B. There are three possible steps in the rotational dynamics of this model: first, the C-Si bonds of the chemisorbed ring anchoring the molecule to the surface have to be broken ($E_{desorb} \approx 1$ eV), making the molecule unbound. Second, the molecule rotates around the chemisorbed ring to align with state B. Finally, a new pair of C atoms in the chemisorbed ring bonds to the same pair of silicon rest atoms and the adatom surface. In a previous study of chlorobenzene adsorption on Si(111)-7×7 [137], it was reported that the C atom connecting to the Cl atom is not involved in bonding to the silicon atom. We suggest that the same bonding characteristics can be applied to the chemisorbed ring of PCB in both adsorption states. This model agrees with this bonding characteristic as rotation of the pair of carbon atoms in the chemisorbed ring by 60° can avoid the C-Cl bond which is involved in bonding with the surface.

5.4 Conclusion

The manipulation of PCB induced by electron injection from STM produces four distinct products: desorption, double dark feature, single dark feature and a bi-stable adsorbed PCB switching. Measurement of switching was conducted on prepared bi-stable switching molecules. Voltage independence of switching was observed. Therefore, the molecular switching process was driven by thermal excitation at room temperature. By using attempt frequency of 10^{13} s^{-1}, the energy barrier of switching from state A to state B was ~ 80-95 meV and from state B to state A to was ~ 75-85 meV. The injection tip-site dependence of PCB switching was found where the molecule prefers to switch under the tip. The tip lowering the barrier of switching by ~ 5-10 meV when it is an unoccupied molecule site was proposed to explain the site dependence switching. Results also show there is a preference site to switching. These suggest that the tip can be used to control the direction of thermal switching. Molecular rotation was proposed to explain configuration change of bi-stable adsorbed PCB switching.

Chapter 6
Theoretical study of naphthalene 1,8-disulfide

The disulfide bond is interesting since S-S bonds are important structurally for protein stability. Naphthalene 1,8-disulfide was studied to investigate the energies and structures of various charged states by performing the density functional theory calculations using the B3LYP functional with 6-31G* and 6-31+G* basis sets. The disulfide bond has been predicted to be the most affected component when adding/removing electrons to/from the neutral molecule. The dihedral angle, S-C-C-S, was found to be bent out of the naphthalene plane for the dianion state with the 6-31G* basis set, but remains in the plane with the 6-31+G* basis set. The anion state was found to be stable as the calculated electron affinity is positive, whereas other charged states are unstable. Therefore the disulfide bond is a strong candidate to undergo vibrational excitation due to nonadiabatic short lived ionic molecules created by charge injection from an STM tip.

6.1 Background

S-S bonds play an important role in the conformational stability of proteins [31], such as disulfide links between cysteine amino acids to form cystine, which is the most basic cross-linkage in proteins. Recent studies of pathways for disulfide bond formation have shown that disulfide formation is activated by electron transport [227]. In Escherichia coli, the expression of antioxidant genes is driven by the OxyR transcription factor. There is evidence that the formation

of the disulfide bond can stimulate OxyR production [228]. For the photosynthesis procedure, light generates reducing equivalents in chloroplasts that are used for regulation of the mechanism of chloroplast enzymes by reduction of regulatory disulfides [229]. The disulfide radical anion was observed to decay by different pathways through intramolecular or intermolecular routes, including bond breaking, disproportionation, protein-protein cross-linking and electron transfer [230]. Dissociation of the disulfide bonds has been studied by tandem mass spectrometry on proteins after low energy electron capture [231]. Such research indicates how it is crucial to study disulfide bond behaviour in small molecules.

For understanding the structure and reaction mechanisms of individual molecules, microscopy techniques may be used. STM is an efficient way to image and manipulate atoms and molecules on a surface [232-234]. However, images from STM alone might not be enough to explain adsorption features or assign the electronic state of an adsorbate. Fortunately, a parallel method, molecular modeling, has been developed. One of the most successful and popular methods is density functional theory (DFT). This was confirmed by the award of a Nobel Prize in Chemistry in 1998 to its inventors, Walter Kohn and John A. Pople for developing theoretical methods in quantum chemistry [235,236]. Thus, combining both approaches is highly beneficial for understanding interactions between molecules and surfaces [206,237-239].

This chapter reports a study of the disulfide bonds in the naphthalene 1,8-disulfide (NDS) or naphtho-[1,8-cd][1,2]dithiole for the five NDS^q species [q= –2, –1, 0, +1, +2] in the gas phase using DFT. It is divided into three parts: i.) molecular structure ii.) molecular charge analysis iii.) molecular charge distribution. We have focused on the S-S bond distance and S-C-C-S torsion angle. We are mainly interested in investigating which regions of the molecule are most affected when one or two electrons are attached to, or removed from, the neutral NDS molecule. These calculations are relevant to experiments on STM-induced electron transfer and S-S bond fission.

6.2 Computational reviews and methodology

6.2.1 Density functional theory

DFT represents an alternative way to describe the electronic structures of atoms and molecules by using single-electron functions of electron density, as a function of position, which is a realistic picture of atomic scale objects. This idea first appeared in the Thomas-Fermi method [240,241] in the 1920's, relating the total energy of an electronic system to the electron density. A significant development was repeated in a paper by Hohenberg and Kohn in 1964 [242] which showed that the ground state energy can be calculated from the electron density:

$$E = E[\rho] \tag{6.1}$$

where ρ is the electron density at a particular position r : $\rho = \rho(r)$.

However, they did not propose how to solve the equation. Then, in 1965 Kohn and Sham pointed out the minimum energy state of a system can be accessed by a self-consistent method and in addition they showed that the total electronic energy can be represented in the form:

$$E[\rho] = -\frac{1}{2}\sum_{i=1}^{N}\int\psi_i(r)\nabla^2\psi_i(r)dr + \frac{1}{2}\int\int\frac{\rho(r_1)\rho(r_2)}{r_{12}}dr_1dr_2 - \sum_{A=1}^{M}\frac{Z_A}{r_{A1}}\rho(r_1)dr_1 + E_{XC}[p] \tag{6.2}$$

where the electron density is the summation of the orbital densities at a particular location:

$$\rho(r) = \sum_{i=1}^{N}|\psi_i(r)|^2 . \tag{6.3}$$

Equation (6.2) contains several terms: the kinetic energy of electrons, electron-electron repulsion, electron-nuclear attraction and exchange-correlation (E_{xc}) [243]. The latter term, exchange-correlation, is a very important part of DFT that makes accurate calculations possible. The

simplest way to calculate this value is by applying the local density approximation (LDA) based on the uniform electron gas model. From this model, the exchange-correlation energy can be determined by:

$$E_{XC}(\rho(r)) = \int \rho(r)\varepsilon_{XC}(\rho(r))dr \tag{6.4}$$

where $\varepsilon_{XC}(\rho(r))$ is the exchange-correlation energy per electron function. It assumes a small volume in each position in space (r) has a constant electron density $\rho(r)$. Equation (6.2) can be represented in another way by applying equation (6.3). This gives the one-electron Kohn-Sham equations:

$$\left\{-\frac{1}{2}\nabla_1^2 - \sum_{A=1}^{M}\frac{Z_A}{r_{1A}} + \int\frac{\rho(r_2)}{r_{12}}dr_2 + V_{XC}[r_1]\right\}\psi_i(r_1) = \varepsilon_i\psi_i(r_1) \tag{6.5}$$

where $\psi_i(r_1)$ is called a Kohn-Sham orbital.

On the left hand side of equation (6.5), $V_{XC}[r_1]$ is the exchange-correlation functional that can be calculated from:

$$V_{XC}[r] = \left(\frac{\delta E_{XC}[\rho(r)]}{\delta\rho(r)}\right). \tag{6.6}$$

From equation (6.5), it suggested that we can apply a self-consistent approach as in the Hartree-Fock equation. The procedure begins, initially, by guessing $\rho(r)$, next solving equation (6.5) and calculating $V_{XC}[r]$, then the Kohn-Sham orbitals are known. Finally, the new wave functions are used to improve $\rho(r)$. The process is repeated in the next iteration until it convergences.

6.2.2 Hybrid functional

There have been attempts to exploit an advantage of Hartree-Fock theory which has a good result on the molecular scale and local density-functional correlation approximations which can be performed conveniently in terms of electron density. This leads to a half-and-half combination of the exact exchange energy from Hartree-Fock and the exchange-correlation energy from DFT. The successful work comes from Becke in 1993 [244,245] when he represented the exchange-correlation energy as a linear combination:

$$E_{XC} = E_{XC}^{LSDA} + a_0\left(E_X^{exact} - E_X^{LSDA}\right) + a_X\Delta E_X^{B88} + a_C\Delta E_C^{PW91} \tag{6.7}$$

where E_X^{exact} is the exact exchange energy, E_X^{LSDA} is the exchange energy based on the local spin density approximation, ΔE_X^{B88} is the gradient correction to the exchange part [246] and ΔE_C^{PW91} is the gradient correction to the correlation part. The parameters, a_0, a_X, a_C, are determined by matching with experimental data. There are many ways to combine the exchange and correlation functionals together. One famous hybrid functional is the B3LYP functional, which involves Becke's gradient correction to LDA exchange, the Lee-Yang-Parr correlation functional and Vosko, Wilk and Nusair's standard local correlation functional [247] through three parameters in the functional:

$$E_{XC}^{B3LYP} = \left(1-a_0\right)E_X^{LSDA} + a_0E_X^{HF} + a_X\Delta E_X^{B88} + a_CE_C^{LYP} + \left(1-a_C\right)E_C^{VWN}. \tag{6.8}$$

6.2.3 Basis sets

Basis sets are sets of functions used to represent molecular orbitals, which are expanded in terms of linear combinations of atomic orbitals:

$$\psi_i = \sum_{\mu=1}^{n} c_{\mu i}\phi_\mu \tag{6.9}$$

where ψ_i is the i-th molecular orbital, $c_{\mu i}$ are the coefficients of linear combination, ϕ_μ is the μ-th atomic orbital, and n is the number of atomic orbitals. In general, atomic orbital functions are Slater type orbitals, but these are not convenient for calculation. Thus, normally these are replaced by linear combinations of Gaussian functions. There are many types of basis sets, for example, the minimal basis sets, STO-nG. In practice, the choice of basis set depends on the size of the system of interest. The basis sets used in this work are those developed by Pople and co-workers [248-250]. Their basis sets are represented by a notation based on the split valence nature of these sets i.e. n-ijG or n-ijkG: where n is the number of Gaussian primitives for the inner shells, ij or ijk are the number of Gaussian primitives for contractions in the valence shell, such as 6-31G. These sets can be extended by adding d type polarization functions on each non-hydrogen atom, indicated by n-ijG* or n-ijkG*, e.g. 6-31G*, which is suitable for systems with non-isotropic charge distributions. In addition, when anions and molecules containing lone pairs are considered, diffuse functions can be applied to the basis set: a diffuse s-type and p-type Gaussian functions are added to a standard basis set on non-hydrogen atoms. This is represented by n-ij+G or n-ijk+G, such as 6-31+G.

6.3 Computational methods

DFT calculations, using the B3LYP functional and 6-31G* [244,245] and 6-31+G* basis sets [249], have been employed to determine the lowest energy configurations of the five species, NDS^q, q = –2, –1, 0, +1, +2. These calculations were performed using the Gaussian 03 quantum chemistry package [251]. Variations of S-S and C-C bond lengths, S-C-C and C-S-S bond angles, S-C-C-C and S-C-C-S dihedral angles have been determined. The frontier molecular orbitals (MOs) and their energies have also been recorded, as well as the localization of electronic charge as a function of the charge on the molecule, and changes in charge localization accompanying reduction or oxidation.

6.4 Results and discussion

6.4.1 Molecular structure

The ground state of neutral NDS has C_{2v} symmetry, where its line of symmetry is same as mirror plane with 2-fold rotation. The dihedral angle is zero, so the S-S bond is in the same plane as the naphthalene as shown in Fig. 6.1 (a). The S-S bond distance is the 2.13 (2.14) Å from B3LYP calculations with 6-31G* (6-31+G*) basis sets, which is a bit longer than the 2.09 Å of the molecule in crystal structure [252]. The C-S-S and S-C-C angles and the C-S bond length from crystal structure and calculations are in excellent agreement, with 95.6°, 115.0° and 1.76 Å from crystal structure [252] and 95.0°, 115.4° and 1.78 Å from calculations. For negatively charged molecules, as more spaces are required for an extra electron, the S-S bond length is extended by 0.61 Å and S-C-C angles increase to 122º when one electron is attached, forming $NDS^–$. These increasing effects are more evident in $NDS^{2–}$, which has a disulfide bond distance of 3.46 Å. The C-S bonds do not relax, almost preserving the same value as in neutral NDS, 1.78 Å. In a negatively charged molecular system, the extra electrons have less coupling to the

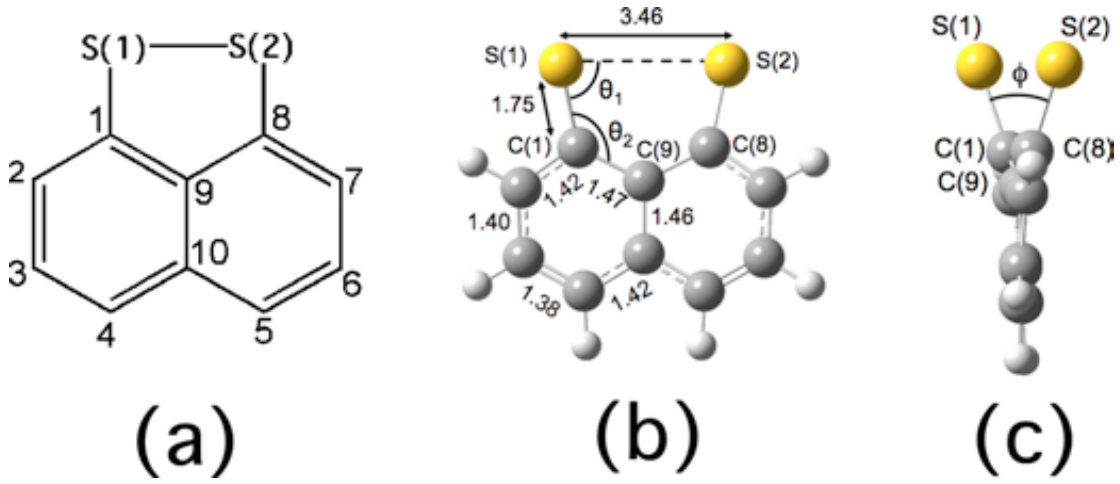

Figure 6.1. (a) Structure of the NDS molecule. (b) Bond lengths (in Å) calculated for NDS^{2-}: the S-S distance is extended to 3.46 Å. (c) Side view of NDS^{2-} shows that the sulfur atoms lie out of the naphthalene plane, with a S-C-C-S dihedral angle of 32.3˚. The NDS^{2-} structure is calculated with the B3LYP functional and 6-31G* basis set. Sulfur and carbon atoms are shown in yellow and grey, respectively.

nucleus, thus it is more feasible to use diffuse orbital basis set functions (e.g. 6-31+G*) to describe these molecules [253]. Using 6-31G*, the S-C-C-S dihedral angle for NDS^{2-} has a non-zero value (32.3°) as seen in Fig. 6.1 (b) and (c). Therefore, the disulfide bond is out of plane with the naphthalene causing the whole molecule to lose planarity and C_{2v} symmetry. This distortion is not observed when using 6-31+G*. There is evidence of a non-zero S-C-C-C angle of –8.9° (Table 6.1) from 1,8-bis(methylthio)naphthalene [254], which is like NDS^{2-} with two extra electrons on sulfur atoms via covalent bonding to methyl groups. This means sulfur atoms are out of the naphthalene plane, which is consistent with results from 6-31G* basis set. The disulfide region carries most of the charge (from molecular orbital calculations mentioned later), thus electrostatic S-S repulsion leads to greater distortion from planarity of neutral configuration.

For positively charged molecules, the S-S bond is slightly contracted by 0.04 (0.07) Å when one electron (two electrons) is removed from NDS molecule. No distortion of other bond lengths and angles was found for NDS^{+} and NDS^{2+}. Both positively charged molecules are unstable due to their very high energy respective to the neutral molecule.

	Calculation					experiment	
	NDS^{2-}	NDS^{-}	NDS	NDS^{+}	NDS^{2+}	NDS [252]	MTNS [254]
$d(S_1\text{-}S_2)$/Å	3.46 (3.32)	2.74 (2.73)	2.13 (2.14)	2.09 (2.09)	2.06 (2.06)	2.09	–
$d(C_1\text{-}S_1)$/Å	1.75 (1.76)	1.76 (1.76)	1.78 (1.78)	1.75 (1.75)	1.72 (1.72)	1.76	1.785
$d(C_8\text{-}S_2)$/Å	1.75 (1.76)	1.76 (1.76)	1.78 (1.78)	1.75 (1.75)	1.72 (1.72)	1.76	1.78
$<C_1S_1S_2$/°	74.4 (78.8)	86.4 (86.7)	95.0 (95.0)	95.6 (95.6)	95.9 (95.6)	95.6	–
$<C_8S_2S_1$/°	74.4 (78.7)	86.4 (86.6)	95.0 (95.0)	95.6 (95.6)	95.9 (95.9)	95.6	–
$<S_1C_1C_9$/°	127.3 (128.1)	122.4 (122.2)	115.4 (115.4)	115.2 (115.2)	115.2 (115.2)	115.0	122.5
$<S_2C_8C_9$/°	127.3 (128.1)	122.4 (122.2)	115.4 (115.4)	115.2 (115.2)	115.2 (115.2)	115.1	121.1
$\Phi(S_1C_1C_9C_8)$	–20.0 (0.0)	0.0 (0.0)	0.0 (0.0)	0.0 (0.0)	0.0 (0.0)	–	–8.3
$\Phi(S_2C_8C_9C_1)$	–20.0 (0.0)	0.0 (0.0)	0.0 (0.0)	0.0 (0.0)	0.0 (0.0)	–	–8.9
$\Phi(S_1C_1C_8S_2)$	32.3 (0.0)	0.0 (0.0)	0.0 (0.0)	0.0 (0.0)	0.0 (0.0)	–	–
E_r (eV)	1.67 (0.77)	–1.27 (–1.56)	0.000 (0.000)	6.79 (6.96)	18.56 (18.79)	–	–

Table 6.1. Selected bond lengths, angles and dihedral angles of five NDS^q species, q = –2, –1, 0, 1, 2, at the B3LYP/6-31G* and (in parentheses) B3LYP/6-31+G* level of theory. The atom numbering follows that shown in Fig. 1 (a). Φ is dihedral angle. Total relative energies (E_r) are calculated relative to the neutral NDS molecule. The NDS experimental values are taken from the X-ray crystal structure of neutral NDS [252], while experimental MTNS values are taken from the X-ray crystal structure of 1,8-bis(methylthio)naphthalene [254].

6.4.2 Molecular orbital analysis

Fig. 6.2 shows that the LUMO of neutral NDS has almost S-S σ* character from B3LYP/6-31G* and 6-31+G* calculations while most benzene derivatives has π* character for LUMO [255]. This result is in agreement with previous studies of the diphenyl disulfide molecule at the B3LYP/6-31G* and MP2/6-31G* levels [256]. However, our calculated LUMO is distinct (in terms of the electron density distribution) from the results of previous work on the NDS molecule [257]. Compared to the LUMO, the HOMO is more evenly distributed between the disulfide unit, where it has π* character, and the ring system. This π* character on the S-S bond explains the contraction of the calculated S-S bond when the NDS molecule is ionized. A similar shortening of both S-S bonds (from 2.097 Å to 2.085 Å) has been reported upon ionization of tetrathionapthalene (TTN) [258], which is related to NDS, having two disulfide groups, which bridge carbons 4 and 5, as well as 1 and 8 (coordinates mentioned in Fig 6.1 (a)). The two HOMOs of TTN have also been calculated to possess S-S π* character [258].

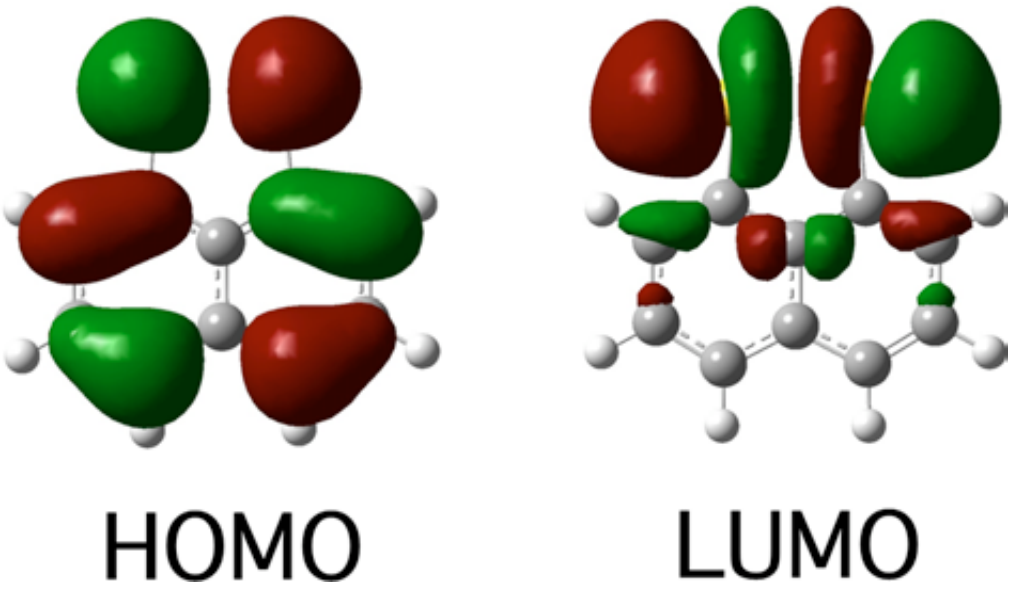

Figure 6.2. The HOMO and LUMO of the neutral NDS molecule. The HOMO has π* character and the LUMO has σ* character on the disulfide unit.

For the open shell NDS^- ion, unrestricted Hartree-Fock calculations were performed. This results in the splitting of the MOs into up-spin and down-spin manifolds. The singly occupied molecular orbital (SOMO) for NDS^- is the up-spin S-S σ* orbital. In the NDS^{2-} dianion, the energy levels are destablilized. The HOMO has a S-S σ* antibonding character and the LUMO has a C-C π bonding character. Considering cationic NDS^+, the SOMO has up-spin S-S π* character. Further lowering of the electronic energy levels is observed for NDS^{2+}.

6.4.3 Molecular charge distribution

Using the Mulliken population analysis approach [259], the charge localization for the five optimized NDS species was calculated at the DFT level, using both the 6-31G* and 6-31G+* basis sets. (In the following discussion, the first numbers given are from calculations using the 6-31G* basis set, with those in parentheses being for the 6-31G+* basis.) For neutral NDS, for both basis sets, the disulfide unit carries a positive charge: +0.19 (+0.22), with the carbon atoms having negative charges. Fig. 6.3 shows the electron localization for the ions, NDS^q, q = –2, –1, 1, 2 relative to the neutral molecule, for the 6-31G* basis. In NDS^-, it is found that the excess electron is mainly associated with the S-S bond: 0.34e per sulfur atom (0.37e), so the S-S unit gains 0.69e (0.74e). When one more electron is added, to generate NDS^{2-}, the S-S unit contains twice the excess electron localization compared to NDS^-: i.e. 0.69e (0.76e) localizes on each sulfur atom and the total electron localization in the S-S unit is 1.38e (1.51e). These results are consistent with the LUMO of neutral NDS being mainly localized on the disulfide unit (fig. 6.2). Comparing the two basis sets, we see that the more diffuse (6-31G+*) orbitals leads to the localisation of slightly more negative charge on the disulfide unit for the neutral and anionic molecules. This can be explained because diffuse orbitals afford more space for the excess electron(s).

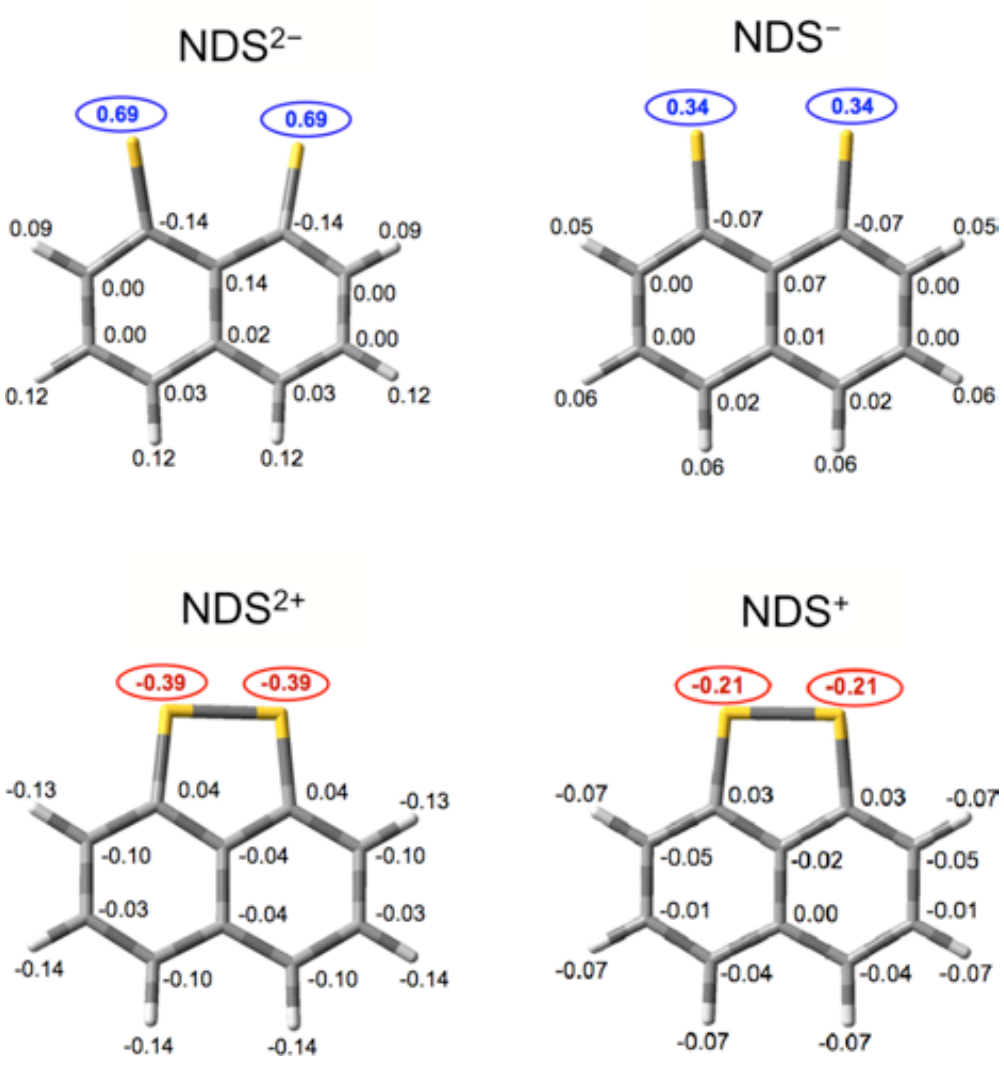

Figure 6.3. Localization of excess electrons (relative to neutral NDS), calculated with the B3LYP functional and the 6-31G* basis set, for charged NDSq molecules (Negative numbers represent a decrease in electron density).

On the other hand, when an electron is removed from neutral NDS, to generate NDS^{+}, nearly half an electron, 0.42e (0.38e) is lost from the S-S unit. In NDS^{2+}, the electron loss from the S-S unit is not quite doubled, being 0.78e (0.69e), compared to NDS^{+}. The fact that the disulfide unit loses less electron density on going to the cationic states than it gains when going to the anionic states is consistent with the more S-S localized nature of the LUMO, compared to the HOMO. However, it is evident that, for both oxidation and reduction, the S-S bond is the region of the NDS molecule which is redox active.

Our calculations reveal NDS^- is stable as it has a negative electron affinity. However, in the gas phase NDS^{2-} is unstable, as it has a positive electron affinity, partly due to the fact that the naphthalene backbone constrains the negatively charged sulfur atoms to remain in relatively close proximity. Minimization of S-S electrostatic repulsion in the gas phase explains the non-planar nature of NDS^{2-} with the 6-31G* basis set. For the 6-31+G* basis set, although the molecule remains planar, the S_1-C_1-C_9 and S_2-C_8-C_9 angles increase significantly, thereby increasing the non-bonding S-S distance. Of course, the interaction of the molecule with a substrate will affect the relative stabilities of the neutral and charged NDS molecules, so that STM-induced S-S fission of surface-supported NDS remains of interest [93-95]. Other electronic properties of interest for future study include quantifying the aromaticity of the C_3S_2 ring, as a function of the charge on the NDS molecule. It has been suggested that in the neutral NDS molecule, if the S π-lone pairs are delocalized over the entire molecule, then NDS should gain π-aromaticity, having 14 π electrons [260].

Our calculations of the HOMO and LUMO electron density distributions of NDS and $NDS^{\pm}$ are in good agreement with the ESR measurements reported by Zweig and Hoffmann [257] and consistent with photoelectron spectra for HOMO of NDS molecule [261]. Our calculations, however, give better agreement with experiment for NDS+ than the SCF calculations of Zweig and Hoffmann, having higher electron density on carbons 4,5 and 2,7 than on carbons 3,6. Also, our calculations reveal that the LUMO for neutral NDS (i.e. the SOMO for NDS^-) is predominantly localized on the sulfur atoms, in agreement with the extremely narrow ESR signal (indicating low coupling with carbon) observed for NDS^-, in contrast to the SCF calculations of Zweig and Hoffmann [257].

6.5 Conclusion

Ab initio calculations predict the disulfide bond is the most changing component in the ionic molecules compared to the neutral molecule. The disulfide bond length increases when the molecule gains an electron, whereas it decreases when the molecule loses an electron. Moreover, two electrons addition or removal has more effect on the molecular geometry and MOs than one electron. Most geometric parameters, e.g. S-S and C-S bond lengths, calculated using the two basis sets, are consistent. Disagreement between the 6-31G* and 6-31+G* basis sets for the calculated dihedral angle (S-C-C-S) in NDS^{2-} has been explored. A non-zero dihedral angle of 32.3° is suggested using the 6-31G* basis set, but this is not found for the 6-31+G* basis set. Localization in the neutral and charged molecules allows investigation of electron transfer phenomena on adding or removing electrons. The predominant localization of the HOMO and LUMO of neutral NDS on the S-S unit are confirmed by the changes in atomic charges upon adding or removing one or two electrons. This explains the sensitivity of the S-S bond to the gain/loss of electrons. The total energy of NDS^{-} is lower than NDS for both basis sets, while for NDS^{2-}, NDS^{+} and NDS^{2+}, the molecular energies are higher than for the neutral molecule. Thus the calculations suggest that NDS^{-} is stable, while NDS^{2-} and other positively charged molecules are unstable in the gas phase. Our results have also been shown to be consistent with previous ESR measurements on the radical species NDS^{+} and NDS^{-} [257]. The sensitivity of the disulfide bond for adding/removing electrons promotes the disulfide bond to be a strong candidate to undergo vibrational excitation due to nonadiabatic short lived ionic molecules created by charge injection from an STM tip.

Chapter 7
Summary and future work

7.1 Summary

In this thesis, the molecular manipulation of PhCl dissociation and PCB switching by STM on Si(111)-7×7 surface were presented. The first principles calculations of the bond in the NDS molecule were also shown.

Investigation of dissociation of PhCl induced by STM at room temperature showed the dissociation of the chlorobenzene molecule at room temperature requires 1.4 ± 0.1 electrons. This was interpreted as a mixture of a two-electron temperature independent and one-electron temperature dependent processes. The thermal activation energy of the one-electron dissociation process of 0.8 ± 0.2 eV agrees with the activation barrier for molecular diffusion of 0.84 ± 0.08 eV. This suggests that the thermally assisted one-electron dissociation occurs in the physisorbed state which is a transient state for diffusion of molecules. This thermally promoted dissociation process bring together two distinct processes of surface science, i.e. molecular diffusion and dissociation of molecules.

The manipulation of PCB induced by electron injection from STM produces four distinct products: desorption, a double dark feature, a single dark feature and bi-stable adsorbed PCB switching. Measurement of switching was conducted on prepared bi-stable switching molecules. Voltage independence of switching was observed, meaning that molecular switching process was driven by thermal excitation at room temperature. Injection tip-site dependence of PCB switching was found. Attractive chemical tip-molecule interactions possibly play an important role in

governing switching. Molecular rotation was proposed to explain configurational changes in bi-stable adsorbed PCB switching.

The study of the disulfide bond in the NDS molecule in various charged states was investigated by DFT calculations. The disulfide bond has been predicted to be the most affected component when adding/removing electrons to/from the neutral molecule. A dihedral angle of the disulfide bond of 32.3° was found in the dianion state with the 6-31G* basis set but not for the 6-31+G* basis set. The extension of the S-S bond distance was calculated for negative ions.

Results of the thesis have applications to molecular devices and protein dynamics. The work of thermally assisted dissociation presented in chapter 4 gives insight on how thermal energy leads to molecular dissociation on solid surfaces. This would have impact on the fundamental understanding of nanostructure fabrication and creating prototype nanomachines and nano-scale devices. The achievement of molecular switching was shown in chapter 5. This molecular switch has the advantage of being controlled at room temperature and can be prepared with well-established methods. This makes this type of molecular switch one contender for a future basic logic unit, a key element of organic electronics. Simulation of the NDS molecule in chapter 6 contributes to understanding the structure of the disulfide bond and its electronic distribution. The calculations motivate experiments to manipulate the disulfide bond in the NDS molecule by STM. Such experimental results are relevant to improving understanding of the role of disulfide bonds in protein folding.

7.2 Future work

The results of thermally assisted dissociation in chapter 4 suggest the following interesting experiments. As there is very little thermal energy at low temperature, room temperature one-electron and two-electron dissociation process may be separated at low temperature. Chemisorbed molecules can be prepared by dosing molecules on to surfaces at room temperature before cooling the samples down to low temperature. Observation of the two-electron dissociation process is expected for pure chemisorbed chlorobenzene molecules. In contrast, physisorbed molecules can be prepared by dosing molecules onto surfaces at low

temperature. Experiments to confirm the one-electron dissociation process of the physisorbed state can be performed without assistance from thermal excitation.

Some extensive experiments for PCB switching are suggested based on the results in chapter 5. The role of the electric field in PCB switching is still not clear. To investigate this effect, the same measurement procedure of molecule switching should be conducted either changing the sample bias polarity to negative or the magnitude of the electric field. If the electric field has an important role for activating switching, locating the tip above the bright ring with negative bias on the sample would cause the ring to switch to another site. The magnitude of the electric field in the STM junction can be varied by sample-tip distance via tuning tunnelling current. Therefore, the role of the electric field PCB switching can be tested from measurement of switching rate as a function of tunnelling current. Moreover, reaction yields for type I to IV can be measured as a function of voltage for injection on both adsorption sites (dark and bright). This would give the threshold of each reaction if electronic excitation is driving the reaction.

As DFT calculations show the S-S bond in NDS molecule is the most sensitive bond when adding electrons, the disulfide bond is very likely to be vibrationally excited in charged molecules, resulting in bond dissociation. These temporary charged molecules can be created by charge injection from an STM tip. Other molecules containing a disulfide bond, such as diphenyl disulfide and dimethyl disulfide, would also be worth investigating.

Appendix A
Nonlocal dissociation by electron injection

The STM tip was used as a source to provide electron pulses aiming to induce dissociation of the C-Cl bond of single chlorobenzene molecules on a Si(111)-7×7 surface. Dissociation and desorption of chlorobenzene were measured as function of distance from injection sites. However, most of the induced nonlocal reactions were molecular desorption events, which was studied more by my colleague. These experiments suggest that electrons emerging from an area localised under the tip caused nonlocal reactions.

A.1 Local dissociation experiments

A.1.1 Experimental methods

Dissociation of chlorobenzene molecules by STM was reported by exposing the whole image of the chlorobenzene/Si(111)-7×7 surface with electrons from a STM tip [80,81]. Each chlorobenzene molecule interacts with a certain number of electrons when the STM tip scans above the molecules. Besocke-style STM [146] provides enough stability to place an STM tip on specific position, even at room temperature, for 30 seconds. Here, current pulses of electron injection from STM tip were performed above individual chlorobenzene molecules on a Si(111)-7×7 surface to induce C-Cl bond breaking on specific molecules. As molecules bind to pairs of

adatoms and rest atoms, injection sites were conducted on middle adatoms and rest atoms with molecules adsorbing on faulted and unfaulted sites. Dissociation as site dependence also was conducted, where injection sites were varied around adsorbed molecules. The tunnelling current was kept constant while electrons were injected. Changes in the tunnelling junction can be detected by monitoring the z-piezo voltage. Voltages applied during injection were above the C-Cl dissociation threshold of 3.0 V [80,173]. 45 experiments were done on molecules adsorbing on faulted sites with current pulses of 200-350 pA, 3.1-4.0 V for 120 ms on middle adatoms where molecules were bound. 26 experiments were carried out on molecules adsorbing on unfaulted sites with current pulses of 200-400 pA, 3.1-3.6 V for 120 ms.

A.1.2 Results and discussion

All these experiments gave desorption of adsorbed molecules as molecules left the surface and clean silicon adatoms appeared, as shown in Fig. A.1. None of the dissociation events were observed from images taken at +2 V before and after injection, in which dissociated chlorine atoms appear dark at +1 V and bright at +2 V [80, 81]. Dissociation of molecules was not observed even when injecting current pulses at sites between a middle adatom-rest atom pair where chlorobenzene ring bridging occurs. Therefore, injection sites around molecules, which may have more coupling with molecule adsorbates via the p-orbital of tip states [173], were investigated. Fig. A.2 shows results from pulse injection as site dependence. The positions (marked with triangles) on the unit cell present where tip-injected electrons with a current pulse of 330 pA with (a) +3.75 V and (b) +3.5 V for 120 ms. Numbered triangles correspond to the number of experiments on particular sites. Only desorption of molecules was observed, the desorption of neighbour molecules can often be observed. This suggests that the dissociation process was overshadowed by desorption and that the leaking of electrons localised in the proximity of the tip caused desorption of molecules at a far distance.

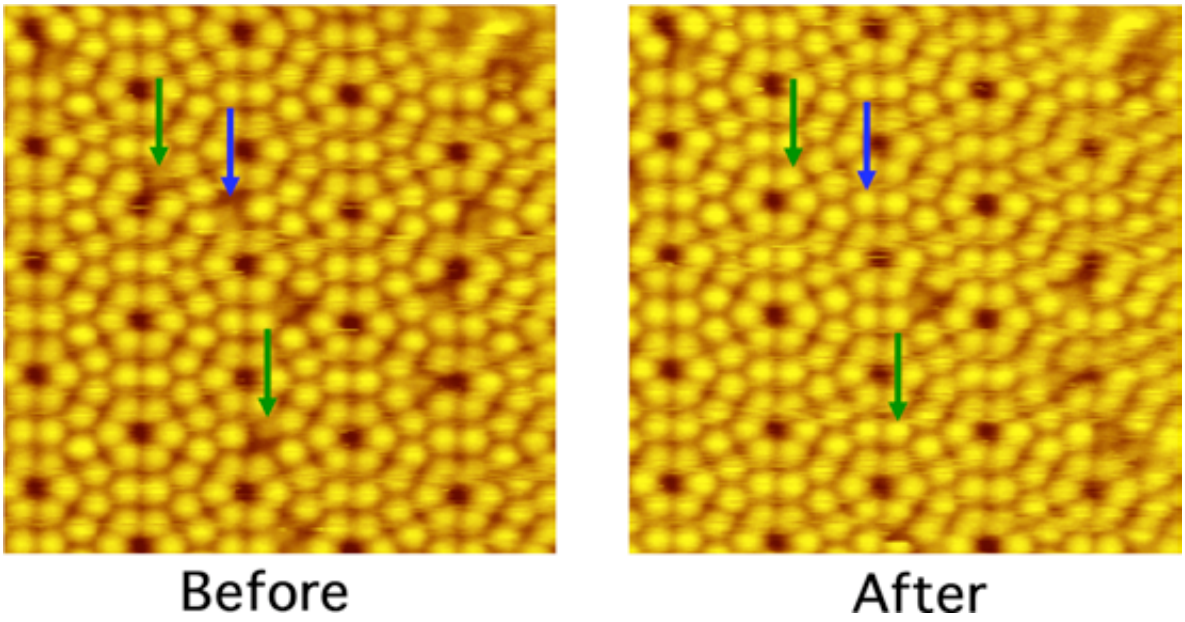

Figure A.1. Current pulse was injected into the molecule (marked with a blue arrow) with +3.75 V, 330 pA for 100 ms. Desorption also was found on molecules absorbed far from the injection site (marked with green arrows). Noise from the images is due to the effect of tip apex instability.

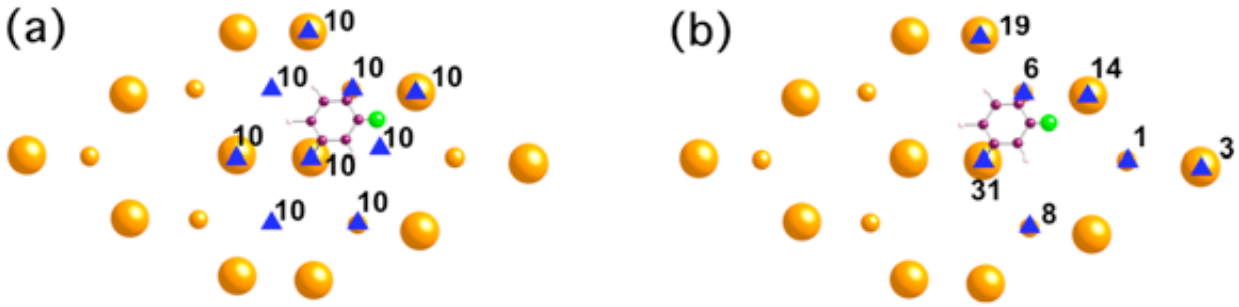

Figure A.2. Current injection pulse of 330 pA, (a) +3.75 V and (b) +3.5 V for 120 ms at the positions (marked with blue triangles) near the molecule adsorption site. Numbers represent the number of experiments on the same site.

A.2 Nonlocal dissociation experiments

A.2.1 Experimental methods

To investigate the observed nonlocal phenomena, experiments were conducted by injecting electrons from an STM tip at the middle of the image to maximise the observable region in the image. Chlorobenzene coverage was generated by exposing 0.8 L of chlorobenzene to the silicon sample. Current pulse injection parameters of +3.75 V, 40 pA and 80 pA for 30 seconds were applied. Fig. A.3 shows passive STM images with +1.0 V and 50 pA before (a) and after (b) current injection. Dark spots are chlorobenzene molecules. Defects on this surface, such as missing adatoms, can also have the same dark feature. However, this represents less than 1% of all defects, thus their effects on the observed population of adsorbed molecules are ignored. Molecule desorption can be measured by comparing +1 V before and after injection pulses are operated, as shown in Fig. A.3 (a) and (b). Molecules disappearing from adsorption sites in (a) and clean silicon adatoms revealed in (b) were indicated and counted as desorption events. Dissociation of molecules can be indentified from images taken at +2 V before and after current injection. Investigating the molecular reactions as a function of distance away from the injection point could reveal their non-localised character. To analyse these results, dissociated molecules were counted from the annulus of increasing radii from the injection site. This manual counting technique provided good insight into the nonlocal effect. Subsequently, a computer programme was written by Dr. Wolfgang Theis to transform the STM image into a more accessible format, i.e. a matrix of molecule coordinates in a unit cell of the surface. This program was used in initial phase of analysis for nonlocal desorption, then developed by Dr. Peter A. Sloan. Fig. A.4 displays an example of a computer programme-analysed image on a selected location in Fig. A.3. Molecule positions were marked with red circles relative to the unit cell indicated by a yellow grid. Computer analysis was found to give faster and higher resolution.

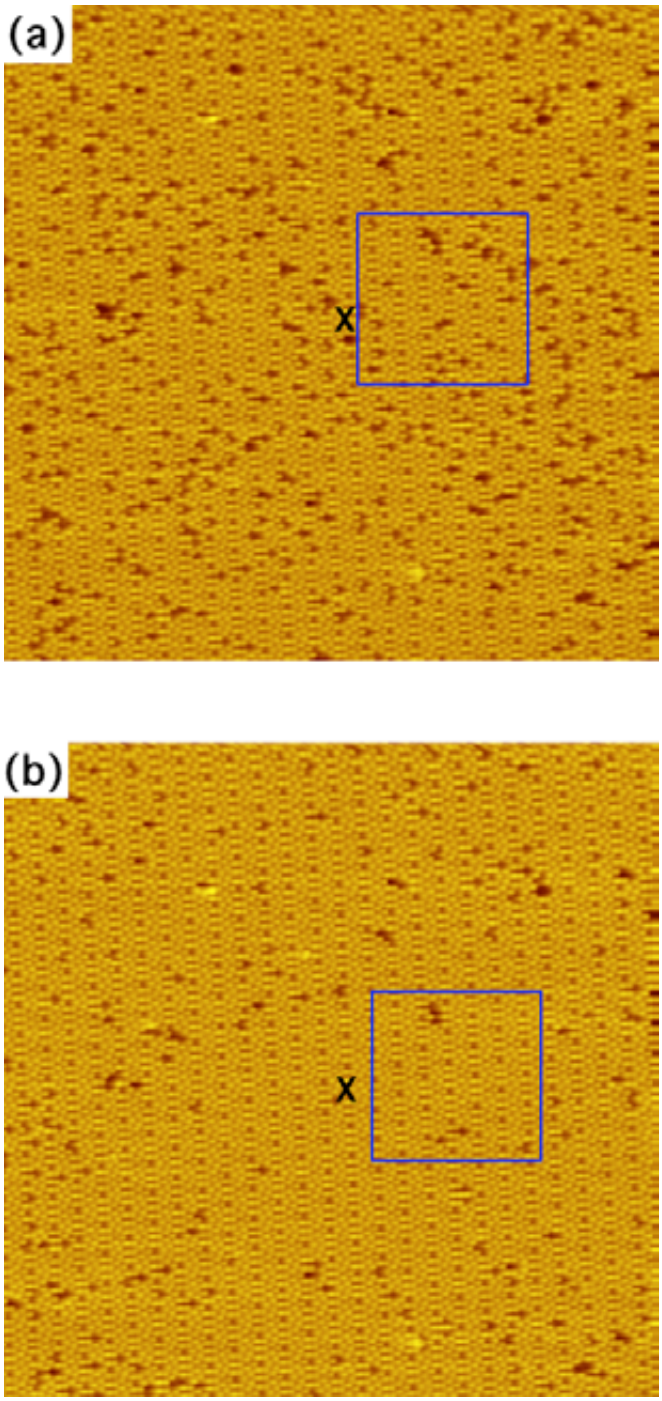

Figure A.3. Current injection at the middle of the image with +3.75 V, 330 pA for 30 seconds. (a) STM image before injection at the marked point, "X". (b) STM image after injection. Nonlocal desorption from injection site can be seen even 100 Å away from the site. Both images were taken at +1 V, 50 pA with an area size of 600 Å × 600 Å.

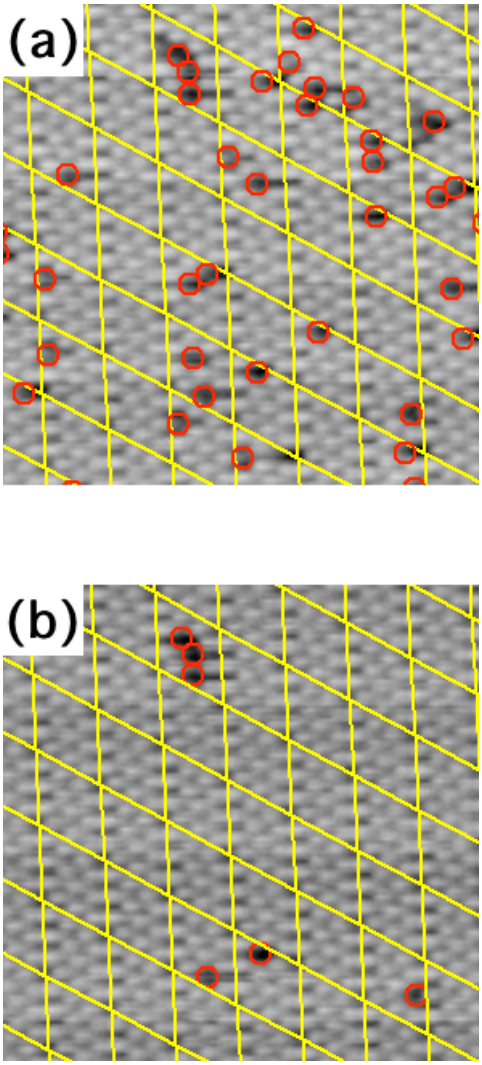

Figure A.4. Analysed STM images (a) before and (b) after current injection from a selected area of 176 Å x 176 Å taken from the previous figure (blue rectangle). Yellow grids represent the unit cell of Si(111)-7×7 and red circles indicate chlorobenzene adsorption sites.

A.2.2.1 Results and discussion

Nonlocal dissociation of chlorobenzene was infrequently observed in this experiment. Since we observed a small population of dissociation events, it is not possible to draw strong conclusion from these results. Fig. A.5 displays the number of molecule dissociation events as a function of distance from the injection site. Since it is difficult to induce dissociation with this method, further analysis was not carried out. However, the data demonstrate that dissociation can be induced nonlocally from the electron injection site. Nonlocal desorption also was observed. This result provoke extensively by my college to further study (Appendix B in Physical Review Letters).

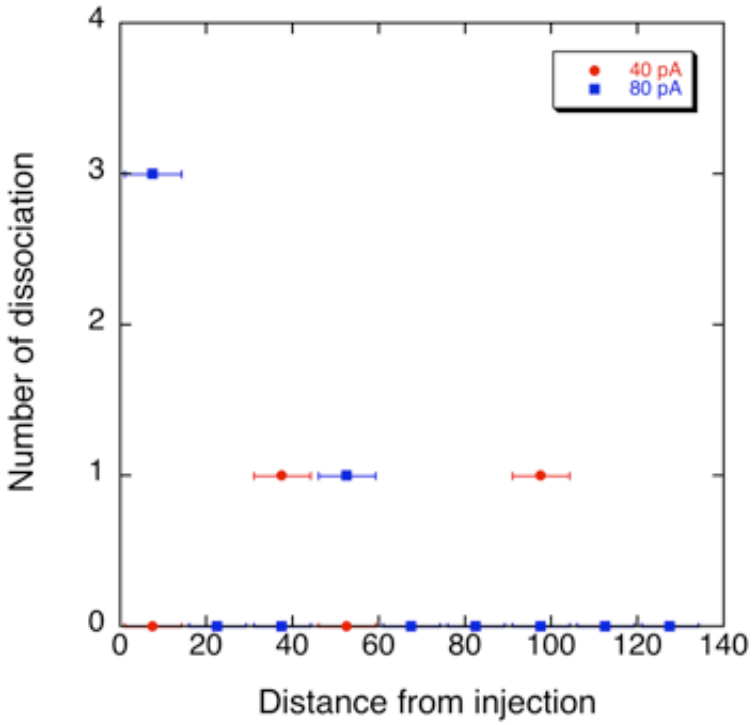

Figure A.5. Number of dissociations as a radial distribution from the injection site with current pulses of +3.75 V, 40 and 80 pA for 30 seconds. Error bars on the y-axis were omitted due to the low number of dissociations.

Appendix B

List of published papers

Sakulsermsuk, S., Sloan, P. A. and Palmer, R. E. A new mechanism of atomic manipulation: bond-selective molecular dissociation via thermally activated electron attachment. Accepted in ACS Nano. DOI: 10.1021/nn101468e

Sakulsermsuk, S., Sloan, P. A. and Palmer, R. E. Calibrating thermal and scanning tunnelling microscope induced desorption and diffusion for the chemisorbed chlorobenzene/Si(111)7×7 system. *J. Phys.: Condens. Matter* **22**, 084002 (2010).

Sloan, P. A., **Sakulsermsuk, S.** and Palmer, R. E. Nonlocal desorption of chlorobenzene molecules form the Si(111)-(7×7) surface by charge injection from the tip of a scanning tunneling microscope: remote control of atomic manipulation. *Phys. Rev. Lett* **105**, 048301 (2010).

References

[1] Feynman, R. P. There's plenty of room at the bottom. *J. Microelectromech. Syst.* **1**, 60-66 (1992).

[2] Binnig, G., Rohrer, H., Gerber, Ch. and Weibel, E. Tunneling through a controllable vacuum gap. *Appl. Phys. Lett.* **40**, 178-180 (1982).

[3] Binnig, G., Rohrer, H., Gerber, Ch. and Weibel, E. Surface studies by scanning tunneling microscopy. *Phys. Rev. Lett.* **49**, 57-61 (1982).

[4] Binnig, G., Quate, C. F. and Gerber, Ch. Atomic force microscope. *Phys. Rev. Lett.* **56**, 930-933 (1986).

[5] Eigler, D. M. and Schweizer, E. K. Positioning single atoms with a scanning tunneling microscope. *Nature* **344**, 524-526 (1990).

[6] Gimzewski, J. K. and Joachim, C. Nanoscale science of single molecules using local probes. *Science* **283**, 1683-1688 (1999).

[7] Joachim, C. and Plévert, L. Nanoscience: The invisible revolution. (World scientific, Singapore. 2008).

[8] Joachim, C., Gimzewski, J. K. and Aviram, A. Electronics using hybrid–molecular and mono–molecular devices. *Nature* **408**, 541-548 (2000).

[9] Joachim, C and Ratner, M. A. Molecular electronics: Some views on transport junctions and beyond. *Proc. Natl. Acad. Sci. USA* **102**, 8801-8808 (2005).

[10] Mayne, A. J., Dujardin, G., Comtet, G. and Riedel, D. Electronic control of single–molecule dynamics. *Chem. Rev.* **106**, 4355-4378 (2006).

[11] Avouris, Ph. Manipulation of matter at the atomic and molecular levels. *Acc. Chem. Res.* **28**, 95-102 (1995).

[12] Binnig, G. and Rohrer, H. In touch with atoms. *Rev. Mod. Phys.* **59**, 615-625 (1987).

[13] Clark, K., Hassanien, A., Khan, S., Braun, K.-F., Tanaka, H. and Hla, S.-W. Superconductivity in just four pairs of $(BETS)_2GaCl_4$ molecules. *Nature Nanotech.* **5**, 261-265 (2010).

[14] Heinrich, A. J., Gupta, J. A., Lutz, C. P. and Eigler, D. M. Single–atom spin–flip spectroscopy. *Science* **306**, 466-469 (2004).

[15] Hirjibehedin, C. F., Lutz, C. P. and Heinrich, A. J. Spin coupling in engineered atomic structures. *Science* **312**, 1021-1024 (2006).

[16] Hirjibehedin, C. F., Lin, C.-Y., Otte, A. F., Ternes, M., Lutz, C. P., Jones, B. A., Heinrich, A. J. Large magnetic anisotropy of a single atomic spin embedded in a surface molecular network. *Science* **317**, 1199-1203 (2007).

[17] Serrate, D., Ferriani, P., Yoshida, Y., Hla, S.-W., Menzel, M., Bergmann, K. v., Heinze, S., Kubetzka, A. and Wiesendanger, R. Imaging and manipulating the spin direction of individual atoms. *Nature Nanotech.* **5**, 350-353 (2010).

[18] Feynman, R. P. in: H.D. Gilbert (Ed.), Miniaturization, Reinhold, New York, 1961.

[19] Tao, F., Bernasek, S. L. and Xu, G.-Q. Electronic and structural factors in modification and functionalization of clean and passivated semiconducor surfaces with aromatic systems. *Chem. Rev.* **109**, 3991-4024 (2009).

[20] Wolkow, R. A. Controlled molecular adsorption on silicon: Laying a foundation for molecular devices. *Annu. Rev. Phys. Chem.* **50**, 413-441 (1999).

[21] Nakayama, K., Aldao, C. M. and Weaver, J. H. Vacancy-assisted halogen reactions on Si(100)-(2×1). *Phys. Rev. Lett.* **82**, 568-571 (1999).

[22] Saavedra, H. M., Mullen, T. J., Zhang, P., Dewey, D. C., Claridge, S. A. and Weiss, P. S. Hybrid strategies in nanolithography. *Rep. Prog. Phys.* **73**, 036501 (2010).

[23] Henderson, M. A. The interaction of water with solid surfaces: Fundamental aspects revisited. *Surf. Sci. Rep.* **46**, 1-308 (2002).

[24] Shin, H.-J., Jung, J., Motobayashi, K., Yanagisawa, S., Morikawa, Y., Kim, Y. and Kawai, M. State-selective dissociation of a single water molecule on an ultrathin MgO film. *Nature Mat.* **9**, 442-447 (2010).

[25] Joachim, C., Gimzewski and Aviram, A. Electronics using hybrid-molecular and mono-molecular devices. *Nature* **408**, 541-547 (2000).

[26] Crone, B., Dodabalapur, A., Lin, Y.-Y., Filas, R. W., Bao, Z., LaDuca, A., Sarpeshkar, R., Katz, H. E. and Li, W. Large-scale complementary integrated circuits based on organic transistors. *Nature* **403**, 521- 523 (2000).

[27] Crooks, R. M. and Ricco, A. J. New organic materials suitable for use in chemical sensor arrays. *Acc. Chem. Res.* **31**, 219-227 (1998).

[28] Kane, B. E. A silicon-based nuclear spin quantum computer. *Nature* **393**, 133-137 (1998).

[29] Lu, Y., Liu, M. and Lent, C. Molecular quantum-dot celluar automata: From molecular structure to circuit dynamics. *J. Appl. Phys.* **102**, 034311 (2007).

[30] Haider, M. B., Pitters, J. L., DiLabio, G. A., Livadaru, L., Mutus, J. Y. and Wolkow, R. A. Controlled coupling and occupation of silicon atomic quantum dots at room temperature. *Phys. Rev. Lett.* **102**, 046805 (2009).

[31] Chen, J., Song, J.-L., Zhang, S., Wang, Y., Cui, D.-f. and Wang, C.-C. Chaperone activity of DsbC. *J. Biol. Chem.* **274**, 19601-19605 (1999).

[32] Young, R., Ward, J. and Scive, F. Observation of metal–vacuum–metal tunneling, field emission, and the transition region. *Phys. Rev. Lett.* **27**, 922-924 (1971).

[33] Stroscio, J. A., Feenstra, R. M. and Fein, A. P. Electronic structure of the Si(111) 2×1 surface by scanning–tunneling microscopy. *Phys. Rev. Lett.* **57**, 2579-2582 (1986).

[34] http://www.almaden.ibm.com/vis/stm/gallery.html

[35] Bartels, L., Meyer, G. and Rieder, K.-H. Basic steps of lateral manipulation of single atoms and diatomic lusters with a scanning tunneling microscope tip. *Phys. Rev. Lett.* **79**, 697-700 (1997).

[36] Keeling, D. L., Humphry, M. J., Fawcett, R. H. J., Beton, P. H., Hobbs, C. and Kantorovich, L. Bond breaking coupled with translation in rolling of covalently bound molecules. *Phys. Rev. Lett.* **94**, 146104 (2005).

[37] Grill, L., Rieder, K.-H., Moresco, F., Rapenne, Stojkovic, S., Bouju, X. and Joachim, C. Rolling a single molecular wheel at the atomic scale. *Nature Nanotech.* **2**, 95-98 (2007).

[38] Crommie, M. F., Lutz, C. P. and Eigler, D. M. Confinement of electrons to quantum corrals on a metal surface. *Nature* **262**, 218-220 (1993).

[39] Heller, E. J., Crommie, M. F., Lutz, C. P. and Eigler, D. M. Scattering and absorption of surface electron waves in quantum corrals. *Nature* **369**, 464-466 (1994).

[40] Manoharan, H. C., Lutz, C. P. and Eigler, D. M. Quantum mirages formed by coherent projection of electronic structure. *Nature* **403**, 512-515 (2000).

[41] Moon, C. R., Lutz, C. P. and Manoharan, H. C. Single–atom gating of quantum–state superpositions. *Nature Phys.* **4**, 454-458 (2008).

[42] Braun, K.-F. and Rieder, K.-H. Engineering electronic lifetimes in artificial atomic structures. *Phys. Rev. Lett.* **88**, 096801 (2002).

[43] Moon, C. R., Mattos, L. S., Foster, B. K., Zeltzer, G., Ko, W. and Manoharan, H. C. Quantum phase extraction in isospectral electronic nanostructures. *Science* **319**, 782-787 (2008).

[44] Moon, C. R., Mattos, L. S., Foster, B. K., Zeltzer, G. and Manoharan, H. C. Quantum holographic encoding in a two–dimensional electron gas. *Nature Nanotech.* **4**, 167-172 (2009).

[45] Wallis, T. M., Nilius, N. and Ho, W. Electronic density oscillations in gold atomic chains assembled atom by atom. *Phys. Rev. Lett.* **89**, 236802 (2002).

[46] Nilius, N., Wallis, T. M. and Ho, W. Localized molecular constraint on electron delocalization in a metallic chain. *Phys. Rev. Lett.* **90**, 186102 (2003).

[47] Nazin, G. V., Qiu, X. H. and Ho, W. Visualization and spectroscopy of a metal–molecule–metal bridge. *Science* **302**, 77-81 (2003).

[48] Mills, G., Wang, B., Ho, W. and Metiu, H. Electronic states of linear Au clusters supported on metal surfaces: Why are they like those of a particle in a box? *J. Chem. Phys.* **120**, 7738-7740 (2004).

[49] Bowler, D. R. Atomic−scale nanowires: Physical and electronic structure. *J. Phys.: Condens. Matter* **16** R721-R754 (2004).

[50] Persson, M. Computational study of electron states in Au chains on NiAl(110). *Phys. Rev. B* **70**, 205420 (2004).

[51] Oncel, N., Houselt, A. v., Huijben, J., Hallbäck, Gurlu, O., Zandvliet, H. J. W. and Poelsema, B. Quantum confinement between self–organized Pt nanowires on Ge(001). *Phys. Rev. Lett.* **95**, 116801 (2005).

[52] Nilius, N., Wallis, T. M. and Ho, W. Realization of a particle–in–a–box: Electron in an atomic Pd chain. *J. Phys. Chem. B* **109**, 20657-20660 (2005).

[53] Matsui, T., Meyer, Chr., Sacharow, L., Wiebe, J. and Wiesendanger, R. Electronic states of Fe atoms and chains on InAs(110) from scanning tunneling spectroscopy. *Phys. Rev. B* **75**, 165405 (2007).

[54] Zhou, P. H., Moras, P., Ferrari, L., Bihlmayer, G., Blügel and Carbone, C. One–dimensional 3d electronic bands of monatomic Cu chains. *Phys. Rev. Lett.* **101**, 036807 (2008).

[55] Crain, J. N. and Pierce, D. T. End states in one–dimensional atom chains. *Science* **307**, 703-706 (2005).

[56] Oncel, N. Atomic chains on surfaces. *J. Phys.: Condens. Matter* **20**, 393001 (2008).

[57] Díaz-Tendero, S., Fölsch, S., Olsson, F. E., Borisov, A. G. and Gauyacq, J.-P. Electron propagation along Cu nanowires supported on a Cu(111) surface. *Nano Lett.* **8**, 2712-2717 (2008).

[58] Díaz-Tendero, Borisov, A. G. and Gauyacq, J.-P. Extraordinary electron propagation length in a metallic double chain supported on a metal surface. *Phys. Rev. Lett.* **102**, 166807 (2009).

[59] Díaz-Tendero, Olsson, F. E., Borisov, A. G. and Gauyacq, J.-P. Excited electron dynamics in Cu nanowires supported on a Cu(111) surface. *Phys. Rev. B* **79**, 115438 (2009).

[60] Nilius, N., Ganduglia-Pirovano, M. V., Brázdová, Kulawik, M., Sauer, J. and Freund, H-J. Electronic properties and charge state of gold monomers and chains adsorbed on alumina thin films on NiAl(110). *Phys. Rev. B* **81**, 045422 (2010).

[61] Heinrich, A. J., Lutz, C. P., Gupta, J. A. and Eigler, D. M. Molecule cascades. *Science* **298**, 1381-1387 (2002).

[62] Eigler, D. M., Lutz, C. P., Crommie, M. F., Manoharan, H. C., Heinrich, A. J. and Gupta, J. A. Information transport and computation in nanometre–scale structures. *Phil. Trans. R. Soc. Lond. A* **362**, 1135-1147 (2004).

[63] Ternes, M., Lutz, C. P., Hirjibehedin, C. F., Giessibl, F. J. and Heinrich, A. J. The force needed to move an atoms on a surface. *Science* **319**, 1066-1069 (2008).

[64] Naydenov, B., Ryan, P., Teague, L. C. and Bolnad, J. J. Measuring the force of interaction between a metallic probe and a single molecule. *Phys. Rev. Lett.* **97**, 098304 (2006).

[65] Ryan, P.M., Teague, L. C., Naydenov, B., Borland, D. and Boland, J. J. Emergence and visualization of an interface during contact formation with a single molecule. *Phys. Rev. Lett.* **101**, 096801 (2008).

[66] Naydenov, B., Teague, L. C., Ryan, P. and Boland, J. J. Contact formation dynamics: Mapping chemical bond formation between a molecule and a metallic probe. *Nano Lett.* **6**, 1752-1756 (2006).

[67] Berndt, R., Kröger, J., Néel and Schull, G. Controlled single atom and single molecule contacts. *Phys. Chem. Chem. Phys.* **12**, 1022-1032 (2010).

[68] Whitman, L. J., Stroscio, J. A., Dragoset, R. A., Celotta, R. J. Manipulation of adsorbed atoms and creation of new structures on room–temperature surfaces with a scanning tunneling microscope. *Science* **251**, 1206-1210 (1991).

[69] Lyo, I.-W. and Avouris, Ph. Field–induced nanometer– to atomic–scale manipulation of silicon surfaces with the STM. *Science* **253**, 173-176 (1991).

[70] Kobayashi A., Grey, F., Williams, R. S. and Aono, M. Formation of nanometer–scale grooves in silicon with a scanning tunneling microscope. *Science* **259**, 1724-1726 (1993).

[71] Uchida, H., Huang, D., Grey, F. and Aono, M. Site–specific measurement of adatom binding energy differenes by atom extraction with the STM. *Phys. Rev. Lett.* **70**, 2040-2043 (1993).

[72] Dujardin, G., Mayne, A., Robert, O., Rose, F., Joachim, C. and Tang, H. Vertical manipulation of individual atoms by a direct STM tip–surface contact on Ge(111). *Phys. Rev. Lett.* **80**, 3085-3088 (1998).

[73] Bartels, L., Meyer, G. and Rieder, K.-H. Controlled vertical manipulation of single CO molecules with the scanning tunneling microscope: A route to chemical contrast. *Appl. Phys. Lett.* **71**, 213-215 (1997).

[74] Bartels, L., Meyer, G., Rieder, K.-H., Velic, D., Knoesel, E., Hotzel, A., Wolf, M. and Ertl, G. Dynamics of electron–induced manipulation of individual CO molecules on Cu(111). *Phys. Rev. Lett.* **80**, 2004-2007 (1998).

[75] Hahn, J. R. and Ho, W. Single molecule imaging and vibrational spectroscopy with a chemically modified tip of a scanning tunneling microscope. *Phys. Rev. Lett.* **87**, 196102 (2001).

[76] Rezaei, M. A., Stipe, B. C. and Ho, W. Atomically resolved adsorption and scanning tunneling microscope induced desorption on a semiconductor: NO on Si(111)-(7×7). *J. Chem. Phys.* **110**, 4891-4896 (1999).

[77] Tsong, T. T. Effects of an electric field in atomic manipulations. *Phys. Rev. B* **44**, 13703 (1991).

[78] Salling, C. T. and Lagally, M. G. Fabrication of atomic–scale structures on Si(001) surfaces. *Science* **265**, 502-506 (1994).

[79] Gao, S. Quantum kinetic theory of vibrational heating and bond breaking by hot electrons. *Phys. Rev. B* **55**, 1876-1886 (1997).

[80] Gao, S., Busch, D. G. and Ho, W. Femtosecond dynamics of electron–vibrational heating and desorption. *Surf. Sci. Lett.* **344**, L1252-L1258 (1995).

[81] Menzel, D. and Gomer, R. Desorption from metal surfaces by low–energy electrons. *J. Chem. Phys.* **41**, 3311-3328 (1964).

[82] Redhead, P. A. Interaction of slow electrons with chemisorbed oxygen. *Can. J. Phys.* **42**, 886 (1964).

[83] Avouris, Ph. and Walkup, R. E. Fundamental mechanisms of desorption and fragmentation induced by electronic transitions at surfaces. *Annu. Rev. Phys. Chem.* **40**, 173-206 (1989).

[84] Misewich, J. A., Heinz, T. F. and Newns, D. M. Desorption induced by multiple electronic transitions. *Phys. Rev. Lett.* **68**, 3737-3740 (1992).

[85] Shen, T.-C., Wang, C., Abeln, G. C., Tucker, J. R., Lyding, J. W., Avouris, Ph. and Walkup, R. E. Atomic–scale desorption through electronic and vibrational exciation mechanisms. *Science* **268**, 1590-1592 (1995).

[86] Prybyla, J. A., Heinz, T. F., Misewich, J. A., Loy, M. M. T. and Glownia, J. H. Desorption induced by femtosecond laser pulses. *Phys. Rev. Lett.* **64**, 1537-1540 (1990).

[87] Soukiassian, L., Mayne, A. J., Carbone, M. and Dujardin, G. Atomic–scale desorption of H atoms from the Si(100)-2×1:H surface: Inelastic electron interactions. *Phys. Rev. B* **68**, 035303 (2003).

[88] Gao, S, Persson, M. and Lundqvist, B. I. Theory of atom transfer with a scanning tunneling microscope. *Phys. Rev. B* **55**, 4825-4836 (1997).

[89] Salam, G. P., Persson, M. and Palmer, R. E. Possibility of coherent multiple excitation in atom transfer with a scanning tunneling microscope. *Phys. Rev. B* **49**, 10655-10662 (1994).

[90] Sokbro, K., Thirstrup, C., Sakurai, M., Quaade, U., Hu, B. Y.-K., Perez-Murano, F. and Grey, F. STM–induced hydrogen desorption via a hole resonance. *Phys. Rev. Lett.* **80**, 2618-2621 (1998).

[91] Stipe, B. C., Rezaei, M. A., Ho, W., Gao, S., Persson, M. and Lundqvist, B. I. Single–molecule dissociation by tunneling electrons. *Phys. Rev. Lett.* **78**, 4410-4413 (1997).

[92] Alavi, S., Rousseau, Patitsas, S. N.,Lopinski, G. P., Wolkow, R. A. and Seideman, T. Inducing desorption of organic molecules with a scanning tunneling microscope: Theory and experiments. *Phys. Rev. Lett.* **85**, 5372-5275 (2000).

[93] Lu, P. H., Polanyi, J. C. and Rogers, D. Electron–induced "localized atomic reaction" (LAR): Chlorobenzene adsorbed on Si(111)-7×7. *J. Chem. Phys.* **111**, 9905-9907 (1999).

[94] Sloan, P. A. and Palmer, R. E. Two–electron dissociation of single molecules by atomic manipulation at room temperature. *Nature* **434**, 367-371 (2005).

[95] Sloan, P. A., Hedouin, M. F. G., Palmer, R. E. and Persson, M. Mechanisms of molecular manipulation with the scanning tunneling microscope at room temperature: Chlorobenzene/Si(111)-7×7. *Phys. Rev. Lett.* **91**, 118301 (2003).

[96] Mayne, A. J., Lastapis, M., Baffou, G., Soukiassian, L., Comtet, G., Hellner, L. and Dujardin, G. Chemisorbed bistable molecule: Biphenyl on Si(100)-2×1. *Phys. Rev. B* **69**, 045409 (2004).

[97] Cranney, M., Mayne, A. J., Laikhtman, A., Comtet, G. and Dujardin, G. STM excitation of individual biphenyl molecules on Si(100) surface: DIET or DIEF? *Surf. Sci.* **593**, 139-146 (2005).

[98] Lastapis, M., Martin, M., Riedel, D. and Dujardin, G. Role of the dopant in silicon on the dynamics of a single adsorbed molecule. *Phys. Rev. B* **77**, 125316 (2008).

[99] Cranney, M., Comtet, G., Dujardin, G., Kim, J. W., Kampen, T. U., Horn, K., Mamatkulov, M., Stauffer, L. and Sonnet, Ph. Electronic structure of biphenyl on Si(100). *Phys. Rev. B* **76**, 075324 (2007).

[100] Martin, M., Lastapis, M., Riedel, D., Dujardin, G., Mamatkulov, M., Stauffer, L. and Sonnet, Ph. Mastering the molecular dynamics of a bistable molecule by single atom manipulation. *Phys. Rev. Lett.* **97**, 216103 (2006).

[101] Mamatkulov, M., Stauffer, L., Minot, C. and Sonnet, Ph. *Ab initio* study of biphenyl chemisorption on Si(001): Configurational stability. *Phys. Rev. B* **73**, 035321 (2006).

[102] Riedel, D., Bocquet, M.-L., Lesnard, H., Lastapis, M., Lorente, N., Sonnet, Ph. and Dujardin, G. Selective scanning tunnelling microscope electron–induced reactions of single biphenyl molecules on a Si(100) surface. *J. Am. Chem. Soc.* **131**, 7344-7352 (2009).

[103] Mayne, A. J., Soukiassian, L., Commaux, N., Comtet, G. and Dujardin, G. Molecular molds. *App. Phys. Lett.* **85**, 5379-5381 (2004).

[104] Lastapis, M., Martin, M., Riedel, D., Hellner, L., Comtet, G. and Dujardin, G. Picometer–scale electronic control of molecular dynamics inside a single molecule. *Science* **308**, 1000-1003 (2005).

[105] Comtet, G., Dujardin, G., Mayne, A. J. and Riedel, D. Principles of operating molecular nanomachines by electronic excitation. *J. Phys.: Condens. Matter* **18**, S1927-S1934 (2006).

[106] Foley, E. T., Kam, A. F. and Lyding, J. W. Cryogenic and Avouris, Ph. UHV–STM study of hydrogen and deuterium desorption from Si(100). *Phys. Rev. Lett.* **80**, 1336-1339 (1998).

[107] Cavar, E., Blüm, M.-C., Pivetta, M., Patthey, F., Chergui, M. and Schneider, W.-D. Fluorescence and phosphorescence from individual C_{60} molecules excited by local electron tunneling. *Phys. Rev. Lett.* **95**, 196102 (2005).

[108] Stipe, B. C., Rezaei, M. A. and Ho, W. Single–molecule vibrational spectroscopy and microscopy. *Science* **280**, 1732-1735 (1998).

[109] Ho, W. Single–molecule chemistry. *J. Chem. Phys.* **117**, 11033-11061 (2002).

[110] Pascual, J. I., Lorente, N., Song, Z., Conrad, H. and Rust, H.-P. Selectivity in vibrationally mediated single−molecule chemistry. *Nature* **423**, 525-528 (2003).

[111] Komeda, T., Kim, Y., Kawai, M., Persson, B. N. J. and Ueba, H. Lateral hopping of molecules induced by excitation of internal vibration mode. *Science* **295**, 2055-2058 (2002).

[112] Simic-Milosevic, V., Mehlhorn, M., Rieder, K.-H., Meyer, J. and Morgenstern, K. Electron induced ortho–meta isomerisation of single molecules. *Phys. Rev. Lett.* **98**, 116102 (2007).

[113] Morgenstern, K. Isomerization reactions on single adsorbed molecules. *Acc.Chem. Res.* **42**, 213-223 (2010).

[114] Simic-Milosevic, V., Meyer, J. and Morgenstern, K. Chirality change of chloronitrobenzene on Au(111) induced by inelastic electron tunneling. *Angew. Chem. Int. Edn* **48**, 4061-4064 (2009).

[115] Kim, Y., Komeda, T. and Kawai, M. Single–molecule reaction and characterization by vibrational excitation. *Phys. Rev. Lett.* **89**, 126104 (2002).

[116] Kawai, M., Komeda, T., Kim, Y., Sainoo, Y. and Katano, S. Single–molecule reactions and spectroscopy via vibrational excitation. *Phil. Trans. R. Soc. Lond. A* **362**, 1163-1171 (2004).

[117] Sainoo, Y. and Kim, Y., Okawa, T., Komeda, T., Shigekawa, H. and Kawai, M. Excitation of molecular vibrational modes with inelastic scanning tunneling microscopy processes: Examination through action spectra of cis–2–Butene on Pd(110). *Phys. Rev. Lett.* **95**, 246102 (2005).

[118] Motobayashi, K., Kim, Y., Ueba, H. and Kawai, M. Insight into action spectroscopy for single molecule motion and reactions through inelastic electron tunneling. *Phys. Rev. Lett.* **105**, 076101 (2010).

[119] Lauhon, L. J. and Ho, W. Control and characterization of a multistep unimolecular reaction. *Phys. Rev. Lett.* **84**, 1527-1530 (2000).

[120] Ohara, M., Kim, Y., Yanagisawa, S., Morikawa, Y. and Kawai, M. Role of molecular orbitals near the Fermi level in the excitation of vibrational modes of a single molecule at a scanning tunneling microscope junction. *Phys. Rev. Lett.* **100**, 136104 (2008).

[121] Eigler, D. M., Lutz, C. P. and Rudge, W. E. An atomic switch realized with the scanning tunnelling microscope. *Nature* **352**, 600-603 (1991).

[122] Gross, L., Mohn, F., Moll, N., Lilijeroth, P. and Meyer, G. The chemical structure of a molecule resolved by atomic force microscopy. *Science* **325**, 1110-1114 (2009).

[123] Repp, J., Meyer, G., Stojkovic, Gourdon, A and Joachim, C. Molecules on insulating films: Scanning–tunneling microscopy imaging of individual molecular orbitals. *Phys. Rev. Lett.* **94**, 026803 (2005).

[124] Repp, J., Meyer, G., Paavilainen, S., Olsson, F. E. and Persson, M. Imaging bond formation between a gold atom and pentacene on an insulating surface. *Science* **312**, 1196-1199 (2006).

[125] Liljeroth, P., Repp, J. and Meyer, G. Current–induced hydrogen tautomerization and conductance switching of naphthalocyanine molecules. *Science* **317**, 1203-1201206 (2007).

[126] Olsson, F. E., Paavilainen, S., Persson, M., Repp, J. and Meyer, G. Multiple charge states of Ag atoms on ultrathin NaCl films. *Phys. Rev. Lett.* **98**,176803 (2007).

[127] Repp, J., Meyer, G., Olsson, F. E. and Persson, M. Controlling the charge state of individual gold adatoms. *Science* **305**, 493-495 (2004).

[128] Gross, L., Mohn, F., Liljeroth, P., Repp, J., Giessibl, F. J., Meyer, G. Measuring the charge of an adatom with noncontact atomic force microscopy. *Science* **324**, 1428-1431 (2009).

[129] Mikaelian, G., Ogawa, N., Tu, X. W. and Ho, W. Atomic scale control of single molecule charging. *J. Chem. Phys.* **124**, 1311101 (2006).

[130] Repp, J., Meyer, G., Paavilainen, S., Olsson, F. E. and Persson, M. Scanning tunneling spectroscopy of Cl vacancies in NaCl films: Strong electron–phonon coupling in double–barrier tunneling junctions. *Phys. Rev. Lett.* **95**, 225503 (2005).

[131] Heath. J. R. and Ratner, M. A. Molecular electronics. *Physics Today* **56**, 43-49 (2003).

[132] Molen, S. J. v. d. and Liljeroth, P. Charge transport through molecular switches. *J. Phys.: Condens. Matter* **22**, 133001 (2010).

[133] Choi, B.-Y., Kahna, S.-J., Kim, S., Kim. H. and Kim, H. W. Conformational molecular switch of the azobenzene molecule: A scanning tunneling microscopy study. *Phys. Rev. Lett.* **96**, 156106 (2006).

[134] Henzl, J., Bredow, T. and Morgenstern, K. Irreversible isomerisation of the azobenzene derivate methyl orange on Au(111). *Chem. Phys. Lett.* **435**, 278-282 (2007).

[135] Henze, J., Mehlhorn, M., Gawronski, H., Rieder, K.-H. and Morgenstern, K. Reversible cis–trans isomerisation of a single azobenzene molecule. *Angew. Chem. Int. Ed.* **45**, 603-606 (2006).

[136] Alemani, M., Peters, M. V., Hecht, S., Rieder, K.-H., Moresco, F. and Grill, L. Electric field–induced isomerisation of azobenzene by STM. *J. Am. Chem. Soc.* **128**, 14446-14447 (2006).

[137] Lancu, V. and Hla, S.-W. Realization of a four−step molecular switch in scanning tunneling microscope manipulation of single chlorophyll–a molecules. *Proc. Natl. Acad. Sci.* **103**, 13718-13721 (2006).

[138] Parschau, M., Passerone, D., Rieder, K.-H., Hug, H. J. and Ernst, K.-H. Switching the chirality of single adsorbate complexes. *Angew. Chem. Int. Ed.* **48**, 4065-4068 (2009).

[139] Qiu, X. H., Nazin, G. V. and Ho, W. Mechanisms of reversible conformational transitions in a single molecules. *Phys. Rev. Lett.* **93**, 196806 (2004).

[140] Donhauser, Z. J., Mantooth, B. A., Kelly, K. F., Bumm, Monnell, J. D., Stapleton, J. J., Price, D. W. Jr., Rawlett, A. M., Allara, D. L,, Tour, J. M. and Weiss, P. S. Conductance switching in single molecules through conformational changes. *Science* **292**, 2303-2307 (2001).

[141] Nacci, C, Lagoute, J., Liu, X. and Fölsch, S. Conformational switching of single 1,5–cyclooctadiene molecules on Si(001) induced by inelastic electron tunneling. *Phys. Rev. B* **77**, 121405(R) (2008).

[142] Nacci, C., Fölsch, S., Zenichowski, K., Dokic, Klamroth, T. and Saalfrank, P. Current versus temperature–induced switching in a single–molecule tunnel junction: 1,5–cyclooctadiene on Si(001). *Nano Lett.* **9**, 2996-3000 (2009).

[143] Quaade, U. J., Stokbro, K., Lin, R. and Grey, F. Single–atom reversible recording at room temperature. *Nanotechnology* **12**, 265-272 (2001).

[144] Quaade, U. J., Stokbro, Thirstrup, C. and Grey, F. Mechanism of single atom switch on silicon. *Surf. Sci.* **415**, L1037-L1045 (1998).

[145] Mayne, A. J., Lastapis, M., Baffou, G., Soukiassian, L., Comtet, G., Hellner, L. and Dujardin, G. Chemisorbed bistable molecule: Biphenyl on Si(100)-2×1. *Phys. Rev. B* **69**, 045409 (2004).

[146] Lastapis, M., Martin, M., Riedel, D., Hellner, L., Comtet, G. and Dujardin, G. Picometer–scale electronic control of molecular dynamics inside a single molecule. *Science* **308**, 1000-1003 (2005).

[147] Sagisaka, K., Luce, A. and Fujita, D. Silicon adatom switching and manipulation on Si(111)-7×7. *Nanotechnology* **21**, 045707 (2010).

[148] Hata, K., Sainoo, Y. and Shigekawa, H. Atomically resolved local variation of the barrier height of the flip–flop motion of single buckled dimmers of Si(100). *Phys. Rev. Lett.* **86**, 3084-3087 (2001).

[149] Wu, S. W., Ogawa, N., Nazin, G. V. and Ho, W. Conductance hysteresis and switching in a single–molecule junction. *J. Phys. Chem. C* **112**, 5241-5244 (2008).

[150] Ohara, M., Kim, Y. and Kawai, M. Electric field response of a vibrationally excited molecule in an STM junction. *Phys. Rev. B* **78**, 201405(R) (2008).

[151] Moresco, F., Meyer, G., Rieder, K.-H., Tang, H., Gourdon, A. and Joachim, C. Conformational changes of single molecules induced by scanning tunneling microscopy manipulation: A route to molecular switching. *Phys. Rev. Lett.* **86**, 672-675 (2001).

[152] Moresco, F., Meyer, G., Rieder, K.-H., Ping, J., Tang, H. and Joachim, C. TBPP molecules on copper surfaces: A low temperature scanning tunneling microscope investigation. *Surf. Sci.* **499**, 94-102 (2002).

[153] Loppacher, Ch., Guggisberg, M., Pfeiffer, O., Meyer, E., Bammerlin, M., Lüthi, R., Schlittler, R., Gimzewski, J. K., Tang, H. and Joachim, C. Direct determination of the energy required to operate a single molecule switch. *Phys. Rev. Lett.* **90**, 066107 (2003).

[154] Moresco, F., Meyer, G., Rieder, K.-H., Tang, H., Gourdon, A. and Joachim, C. Recording intramolecular mechanics during the manipulation of a large molecule. *Phys. Rev. Lett.* **87**, 088302 (2001).

[155] Grill, L., Moresco, F., Jiang, P., Joachim, C., Gourdon, A. and Rieder, K.-H. Controlled manipulation of a single molecular wire along a copper atomic nanostructure. *Phys. Rev. B* **69**, 035416 (2004).

[156] Kuntze, J., Berndt, R., Jiang, P., Tang, H., Gourdon, A. and Joachim, C. Conformations of a molecular wire adsorbed on a metal surface. *Phys. Rev. B* **65**, 233405 (2002).

[157] Hla, S.-W., Bartels, L., Meyer, G. and Rieder, K.-H. Inducing all steps of a chemical reaction with the scanning tunneling microscope tip: Towards single molecule engineering. *Phys. Rev. Lett.* **85**, 2777 (2000).

[158] Rieder, K.-H., Meyer, G., Moresco, G., Morgenstern, K., Hla, S.-W., Repp, J., Alemani, M., Grill, L., Gross, L., Mehlhorn, M., Gawronski, H., Simic-Milosevich, V., Henzl, J., Braun, K. F., Foelsch, S. and Bartels, L. Force induced and electron stimulated STM manipulations: Routes to artificial nanostructures as well as to molecular contacts, engines and switches. *J. Phys.: Conf. Series* **19**, 175-181 (2005).

[159] Besocke, K. An easily operable scanning tunneling microscope. *Surf. Sci.* **181**, 145-153 (1987).

[160] Frohn, J., Wolf, J. F., Besocke, K. and Teske, M. Coarse tip distance adjustment and positioner for a scanning tunneling microscope. *Rev. Sci. Instrum.* **60**, 1200-1201 (1989).

[161] Bonnell, D. A., in Scanning Tunneling Microscopy and Spectroscopy: Theory, Techniques and Applications, edited by Bonnell, D. A. (VCH, New Yok, 1993), Chap. 2, pp. 17-23.

[162] Vasilescu, G. Electronic Noise and Interfering Signals Principles and Applications. (Springer, Berlin, 2006), pp. 306-308, 398-400.

[163] Ibe, J. P., Bey, Jr. P. P., Brandow, S. L., Brizzolara, R. A., Burnham, N. A., DiLella, D. P., Lee, K. P., Marrian, C. R. K. and Colton, R. J. On the electrochemical etching of tips for scanning tunneling microscopy. *J. Vac. Sci. Technol. A* **8**, 3570-3575 (1990).

[164] Oliva, A. I., Romero, A., Peña, J. L., Anguiano, E. and Aguilar, M. Electrochemical preparation of tungsten tips for a scanning tunneling microscope. *Rev. Sci. Instrum.* **67**, 1917-1921 (1996).

[165] Guise, O. L., Ahner, J. W., Jung, M.-C., Goughnour, P. C. and Yates, Jr. J. T. Reproducible electrochemical etching of tungsten probe tips. *Nano Lett.* **2**, 191-193 (2002).

[166] Lucier, A.-S., Mortensen, H., Sun, Y. and Grütter, P. Determination of the atomic structure of scanning probe microscopy tungsten tips by field ion microscopy. *Phys. Rev. B* **72**, 235420 (2005).

[167] Uchida, H., Huang, D., Grey, F. and Aono, M. Site–specific measurement of adatom binding energy differences by atom extraction with the STM. *Phys. Rev. Lett.* **70**, 2040-2043 (1993).

[168] Kobayashi, A., Grey, F., Williams, R. S. and Aono, M. Formation of nanometer–scale grooves in silicon with a scanning tunneling microscope. *Science* **259**, 1724-1726 (1993).

[169] Grey, F., Huang, D. H. and Aono, M. Tip displacement during STM pulse modification of silicon. *Microelectron. Eng.* **27**, 17-22 (1995).

[170] Heike, S., Hashizume, T. and Wada, Y. In situ control and analysis of scanning tunneling microscope tip by formation of sharp needles on the Si sample and W tip. *J. Vac. Sci. Technol. B* **14**, 1522-1526 (1996).

[171] Schwarzenbach, R. P., Gschweend, P. M. and Imboden, D. M. Environmental Organic Chemistry. (John Wiley & Sons, New York, 1992).

[172] Takayanagi, K., Tanishiro, Y., Takahashi, S., Takahashi, M. Structure analysis of Si(111)-7×7 reconstructed surface by transmission electron diffraction. *Surf. Sci.* **164**, 367-392 (1985).

[173] Chaika, A. N. and Myagkov, A. N. Seeing the atomic orbitals in STM images of Si(111)-(7×7) surface. *J. Phys.: Conf. Ser.* **100**, 012020 (2008).

[174] Cao, Y., Deng, J. F. and Xu, G. Q. Stereo–selective binding of chlorobenzene on Si(111)-7×7. *J. Chem. Phys.* **112**, 4759-4767 (2000).

[175] Dressler, R., Allan, M. and Haselbach, E. Symmetry control in Bond cleavage processes: Dissociative electron attachment to unsaturated halocarbons. *Chimia* **39**, 385-389 (1985).

[176] Stricklett, K. L., Chu, S. C. and Burrow, P. D. Dissociative attachment in vinyl and allyl chloride, chlorobenzene and benzyl chloride. *Chem. Phys. Lett.* **131**, 279-284 (1986).

[177] Burrow, P. D., Modelli, A. and Jordan, K. D. Temporary anion states of the chlorobenzenes. *Chem. Phys. Lett.* **132**, 441-447 (1986).

[178] Modelli, A. and Venuti, M. Temporary π* and σ* anions and dissociative electron attachment in chlorobenzene and related molecules. *J. Phys. Chem. A* **105**, 5836-5841 (2001).

[179] Beregovaya, I. V. and Shchegoleva, L. N. Potential energy surface and dissociative cleavage of chlorobenzene radical anion. *Chem. Phys. Lett.* **348**, 501-206 (2001).

[180] Skalicky, T., Chollet, C., Pasquier, N. and Allan, M. Properties of the π* and σ* states of the chlorobenzene anion determined by electron impact spectroscopy. *Phys. Chem. Chem. Phys.* **4**, 3583-3590 (2002).

[181] Houmam, A. Electron transfer initiated reactions: Bond formation and bond dissociation. *Chem. Rev.* **108**, 2180-2237 (2008).

[182] Jiang, G., Polanyi, J. C. and Rogers, D. Electron and photon irradiation of benzene and chlorobenzene on Si(111)-7×7. *Surf. Sci.* **544**, 147-161 (2003).

[183] Fontanesi, C. Baraldi, P. and Marcaccio, M. On the dissociation dynamics of the benzyl chloride radical anion. An ab initio dynamic reaction coordinate analysis study. *J. Mol. Struct. (Theochem)* **548**, 13-20 (2001).

[184] Palmer, R. E. Electron–molecule dynamics at surfaces. *Prog. Surf. Sci.* **41**, 51-108 (1992).

[185] Palmer, R. E. and Rous, P. J. Resonances in electron–scattering by molecules on surfaces. *Rev. Mod. Phys.* **64**, 383-440 (1992).

[186] Sloan, P. A. and Palmer, R. E. Tip–state control of rates and branching ratios in atomic manipulation. *Nano Lett.* **5**, 835-839 (2005).

[187] Boland, J. J. and Villarrubia, J. S. Formation of Si(111)-(1×1)Cl. *Phys. Rev. B* **41**, 9865-9870 (1990).

[188] Nakamura, Y., Mera, Y. and Maeda, K. Diffusion of chlorine atoms on Si(111)-(7×7) surface enhanced by electron injection from scanning tunneling microscope tips. *Surf. Sci.* **487**, 127-134 (2001).

[189] Sloan, P. A. and Palmer, R. E. Manipulation of polyatomic molecules with the scanning tunnelling microscope at room temperature: Chlorobenzene adsorption and desorption from Si(111)-(7×7). *J. Phys.: Condens. Matter* **18**, 1873-1885 (2006).

[190] Wolkow, R. A. and Moffatt, D. J. The frustrated motion of benzene on the surface of Si(111*). J. Chem. Phys.* **103**, 10696-10700 (1995).

[191] Macpherson, C. D., Hu, D. Q. and Leung, K. T. Room–temperature adsorption of benzene on Si(111)-7×7 by thermal–desorption spectrometry. *Solid State Commun.* **80**, 217-220 (1991).

[192] Cao, Y. et al. Formation of di–sigma bond in benzene chemisorption on Si(111)-7×7. *J. Phys. Chem. B* **103**, 5698-5702 (1999).

[193] Taguchi, Y., Fujisawa, M. and Nishijima, M. Adsorbed state of benzene on the Si(111)(7×7) surface. *Chem. Phys. Lett* **178**, 363-368 (1991).

[194] Brown, D. E., Moffatt, D. J. and Wolkow, R. A. Isolation of an instrinsic precursor to molecular chemisorption. *Science* **279**, 542-544 (1998).

[195] Soe, W.-H., Manzano, C., Sarkar, A. De, Chandrasekhar, N. and Joachim, C. Direct observation of molecular orbitals of pentacene physisorbed on Au(111) by scanning tunneling microscope. *Phys. Rev. Lett.* **102**, 176102 (2009).

[196] Bellec, A., Ample, F., Riedel, D, Dujardin, G. and Joachim, C. Imaging molecular orbitals by scanning tunneling microscopy on a passivated semiconductor. *Nano Lett.* **9**, 144-147 (2009).

[197] Repp, J. and Meyer, G. Molecules on insulating films: Scanning–tunneling microscopy imaging of individual molecular orbitals. *Phys. Rev. Lett.* **94**, 026803 (2005).

[198] Lu, X. K., Polanyi, J. C. and Yang, J. A. Reversible molecular switch based on pattern–change in chlorobenzene and toluene on a Si(111)-(7×7) surface. *Nano Lett.* **6**, 809-814 (2006).

[199] Polychlorinated Biphenyls (PCBs) CAS No. 1336–36–3. *Report on carcinogens*, Eleventh edition.

[200] McFarland, V. A. and Clarke, J. U. Environmental occurrence, abundance, and potential toxicity of polychlorinated biphenyl congeners: Considerations for a congener–specific analysis. *Environ. Health Perspect.* **81**, 225-239 (1989).

[201] Masuda, Y. Approach to rick assessment of chlorinated dioxins from Yusho PCB poisoning. *Organohalogen Compd.* **21**, 1-10 (1994).

[202] Needham, L.L. Historical perspective on Yu–Cheng incident. *Organohalogen Compd.* **14**, 231-233 (1993).

[203] Erickson, M. D. *Analytical Chemistry of PCBs.* (Butterworth, Boston, 1986), p. 45.

[204] Material Safety Data Sheet, SIGMA–ALDRICH, No 1907/2006.

[205] Dorofeeva, O. V., Novikov, V. P., Moiseeva, N. F. and Yungman, V. S. Density functional theory of conformations, barrier to internal rotations and torsional potentials of polychlorinated biphenyls. *J. Mol. Struc. (Theochem)* **637**, 137 (2003).

[206] Wolkow, R. A., Lopinski, G. P. and Moffatt, D. J. Resolving organic molecule–silicon scanning tunneling microscopy freatures with molecular orbital methods. *Surf. Sci.* **416**, L1107-1113 (1998).

[207] Almenningen, A., Bastlansen, O. and Gundersen, S. Structure and barrier of internal rotation of biphenyl derivatives in the gaseous state. Part 3. Structure of 4–fluoro–, 4,4'–difluoro–, 4–chloro– and 4,4'–dichlorobiphenyl. *J. Mol. Struct.* **128**, 95-114 (1985).

[208] Romming, C., Seip, H. M. and Oymo, I.-M. A. Structure of gaseous and crystalline 2,2'–Dichlorobiphenyl. *Acta Chem. Scand. A* **28**, 507-514 (1974).

[209] Almenningen, A., Bastiansen, O. and Fernholt, L. Structure and barrier of internal rotation of biphenyl derivatives in the gaseous state. Part 1. The molecular structure and normal coordinate analysis of normal biphenyl and perdeuterated biphenyl. *J. Mol. Struc.* **128**, 59-76 (1985).

[210] Bastiansen, O. and Samdal, S. Structure and barrier of internal rotation of biphenyl derivatives in the gaseous state. Part 4. Barrier of internal rotation in biphenyl, perdeuterated biphenyl and seven non–ortho–substituted halogen derivatives. *J. Mol. Struc.* **128**, 115-125 (1985).

[211] Arulmozhiraja, S. and Fujii, T. Torsional barrier, ionization potential, and electron affinity of biphenyl – A theoretical study. *J. Chem. Phys.* **115**, 10589-10594 (2001).

[212] Takei, Y., Yamaguchi, T., Osamura, Y., Fuke, K. and Kaya, K. Electronic spectra and molecular structure of biphenyl and para–substituted biphenyls in a supersonic jet. *J. Phys. Chem.* **92**, 577-581 (1998).

[213] Zhang, X., Xi, R., Liu, J., Jiang, J., Wang, G. and Zeng, Q. Molecular and electronic structures as well as vibrational spectra assignment of biphenyl, 2,2'– and 4,4'–dichlorobiphenyl from density functional calculations. *J. Mol. Struc. (THEOCHEM)* **763**, 67-73 (2006).

[214] Zimmermann, R., Weickhardt, C., Boesl, U. and Schlag, E. W. Influence of chlorine substituent positions on the molecular structure and the torsional potentials of dichlorinated biphenyls: R2PI spectra of the first singlet transition and AM1 calculations. *J. Mol. Struc* **327**, 81-97 (1994).

[215] Andersson, P. L., Haglund, P. and Tysklind, M. The internal barrier of rotation for 209 Polychlorinated biphenyls. *Environ. Sci. & Pollut. Res.* **4**, 75-81 (1997).

[216] Zerbi G. and Sandroni, S. Fundamental frequencies and molecular configuration of biphenyl. 2. Normal coordinates. *Spectrochim. Acta* **24A**, 511 (1968).

[217] Barrett, R. M. and Steele, D. The vibrational spectra and dihedral angles of biphenyl and the 4,4'–dihalogenobiphenyls. *J. Mol. Struc.* **11**, 105-125 (1972).

[218] McKinney, J. D., Gottschalk, K. E. and Pedersen, L. A theoretical investigation of the conformation of polychlorinated biphenyls (PCB's). *J. Mol. Struc.* **104**, 445-450 (1983).

[219] Arulmozhiraja, S., Selvin, P. C. and Fujii, T. Structures, potential energy curves, and torsional barrier heights for selected polychlorinated biphenyls: A density functional theory study. *J. Phys. Chem. A* **106**, 1765-1769 (2002).

[220] Henningsen, N., Franke, K. J., Torrente, I. F., Sxhulze, G., Priewisch, B., Rück-Braun, K., Dokic, J., Klamroth, T., Saalfrank, P. and Pascual, J. I. Inducting the roration of a single phenyl ring with tunneling electrons. *J. Phys. Chem. C* **111**, 14843-14848 (2007).

[221] Comstock, M. J., Cho, J., Kirakosian, A. and Crommie, M. F. Manipulation of azobenzene molecules on Au(111) using scanning tunneling microscopy. *Phys. Rev. B* **72**, 153414 (2005).

[222] Henze, J., Mehlhorn, M., Gawronski, H., Rieder, K.-H. and Morgenstern, K. Reversible cis–trans isomerisation of a single azobenzene molecule. *Angew. Chem. Int. Ed.* **45**, 603-606 (2006).

[223] Henzl, J., Mehlhorn, M. and Morgenstern, K. Amino–nitro–azobenzene dimmers as a prototype for a molecular–level machine. *Nanotechnology* **18**, 495502 (2007).

[224] Comstock, M. J., Levy, N., Kirakosian, A., Cho, J., Lauterwasser, F., Harvey, J. H., Strubbe, D. A., Fréchet, Trauner, D., Louie, S. G. and Crommie, M. F. Reversible photomechanical switching of individual engineered molecules at a metallic surface. *Phys. Rev. Lett*. **99**, 038301 (2007).

[225] Dri, C., Peters, M. V., Schwarz, J., Hecht, S. and Grill, L. Spatial periodicity in molecular switching. *Nature Materials* **3**, 649-653 (2008).

[226] Joachim, C., Gimzewski, J. K. and Aviram, A. Electroics using hybrid–molecular and mono–molecular devices. *Nature* **408**, 541-548 (2000).

[227] Collet, J.-F and Bardwell, J. C. A. Oxidative protein folding in bacteria. *Mol. Microbiol.* **44**, 1-8 (2002).

[228] Zheng, M., Åslund, F. and Storz, G. Activation of the OxyR transcription factor by reversible disulfide bond formation. *Science* **279**, 1718-1721 (1998).

[229] Dai, S., Schwendtmayer, C., Schürmann, P., Ramaswamy, S. and Eklund, H. Redox signalling in chloroplasts: Cleavage of disulfides by an iro–sulfur cluster. *Science* **287**, 655-658 (2000).

[230] Favaudon, V., Tourbez, H., Houée-Levin, C. and Lhoste, J.-M. CO2.-radical induced cleavage of disulfide bonds in proteins – A gamma-ray and pulse-radiolysis mechanistic investigation. *Biochemistry* **29**, 10978-10989 (1990).

[231] Zubarev, R. A., Kuger, N. A., Fridriksson, E. K., Lewis, M. A., Horn, D. M., Carpenter, B. K. and McLafferty, F. W. Electron capture dissociation of gaseous multiply–cahrged proteins is favored at disulfide bonds and other sites of high hydrogen. *J. Am. Chem. Soc.* **121**, 2857-2862 (1999).

[232] Eigler, D. M. and Schweizer, E. K. Positioning single atoms with a scanning tunneling microscope. *Nature* **344**, 524-526 (1990).

[233] Eigler, D. M., Lutz, C. P. and Rudge, W. E. An atomic switch realized with the scanning tunneling microscope. *Nature* **352**, 600-603 (1991).

[234] Fishlock, T. W., Oral, A., Egdell, R. G. and Pethica, J. B. Manipulation of atoms across a surface at room temperature. *Nature* **404**, 743-745 (2000).

[235] Kohn, W. Nobel lecture: Electronic structure of matter–wave functions and density functionals. *Rev. Mod. Phys.* **71**, 1253-1266 (1999).

[236] Pople, J. A. Nobel lecture: Quantum chemical models. *Rev. Mod. Phys.* **71**, 1267-1274 (1999).

[237] Hofer, W. A., Fisher, A. J., Lopinski, G. P. and Wolkow, R. A. Adsorption of bezene on Si(100)-(2×1): Adsorption energies and STM image analysis by ab initio methods. *Phys. Rev. B* **63**, 085314 (2001).

[238] Maksymovych, P., Sorescu, D. C. and Yates, Jr., J. T. Methanethiolate adsorption site on Au(111): A combined STM/DFT study at the single–molecule level. *J. Phys. Chem. B* **110**, 21161-21167 (2006).

[239] Borovsky, B., Krueger, M. and Ganz, E. Metastable adsorption of benzene on the Si(001) surface. *Phys. Rev. B* **57**, R4269-R4272 (1998).

[240] Thomas, L. H. The calculation of atomic fields. *Proc. Cambridge Phil. Soc.* **23**, 542-548 (1927).

[241] E. Fermi, Z. *Physik* **48**, 73 (1928).

[242] Hohenberg, P. and Kohn, W. Inhomogeneous electron gas. *Phys. Rev.* **136**, B864-B871 (1964).

[243] Kohn, W. and Sham, L. J. Self–consistent equations including exchange and correlation effects. *Phys. Rev.* **140**, A1133-A1138 (1965).

[244] Becke, A. D. A new mixing of Hartree–Fock and local density–functional theories. *J. Chem. Phys.* **98**, 1372-1377 (1993).

[245] Becke, A. D. Density–functional thermochemistry. III. The role of exact exchange. *J. Chem. Phys.* **98**, 5648-5652 (1993).

[246] Becke, A. D. Density–functional exchange–energy approximation with correct asymptotic behavior. *Phys. Rev. A* **38**, 3098-3100 (1988).

[247] Vosko, S. H., Wilk, L. and Nusair, M. Accurate spin–dependent electron liquid correlation energyies for local spin density calculations: A critical analysis. *Can. J. Phys.* **58**, 1200-1211 (1980).

[248] Ditchfield, R., Hefhre, W. J. and Pople, J. A. Self–consistent molecular methods. IX. An extended Gaussian–Type basis for molecular–orbital studies of organic molecules. *J. Chem. Phys.* **54**, 724-728 (1971).

[249] Hefhre, W. J., Ditchfield, R. and Pople, J. A. Self–consistent molecular orbital methods. XII. Further extensions of Gaussian–Type basis sets for use in molecular orbital studies of organic molecules. *J. Chem. Phys.* **56**, 2257-2261 (1972).

[250] Binkley, J. S., Pople, J. A. and Hehre, W. J. Self–consistent molecular orbital methods. 21. Small split–valence basis sets for first–row elements. *J. Am. Chem. Soc.* **102**, 939-947 (1980).

[251] Frisch, M. J., Trucks, G. W., Schlegel, H. B., Scuseria, G. E., Robb, M. A., Cheeseman, J. R., Montgomery, Jr J. A., Vreven, T., Kudin, K. N., Burant, J. C., Millam, J. M., Iyengar, S. S., Tomasi, J., Barone, V., Mennucci, B., Cossi, M., Scalmani, G., Rega, N., Petersson, G. A., Nakatsuji, H., Hada, M., Ehara, M., Toyota, K., Fukuda, R., Hasegawa, J., Ishida, M., Nakajima, T., Honda, Y., Kitao, O., Nakai, H., Klene, M., Li, X., Knox, J. E.,

Hratchian, H. P., Cross, J. B., Adamo, C., Jaramillo, J., Gomperts, R., Stratmann, R. E., Yazyev, O., Austin, A. J., Cammi, R., Pomelli, C., Ochterski, J. W., Ayala, P. Y., Morokuma, K., Voth, G. A., Salvador, P., Dannenberg, J. J., Zakrzewski, V. G., Dapprich, S., Daniels, A. D., Strain, M. C., Farkas, O., Malick, D. K., Rabuck, A. D., Raghavachari, K., Foresman, J. B., Ortiz, J. V., Cui, Q., Baboul, A. G., Clifford, S., Cioslowski, J., Stefanov, B. B., Liu, G., Liashenko, A., Piskorz, P., Komaromi, I., Martin, R. L., Fox, D. J., Keith, T., Al-Laham, M. A., Peng, C. Y., Nanayakkara, A., Challachombe, M., Gill, P. M. W., Johnson, B., Chen, W., Wong, M. W., Gonzalez, C. and Pople, J. A. *GAUSSIAN 03*, (Revision C. 02), Gaussian, Inc., Wallingford, CT, **2004**.

[252] Aucott, S. M., Milton, H. L., Robertson, S. D., Slawin, A. M. and Woollins, J. D. Crystal structures and molecular modelling of 1,8 chalcogenide–substituted naphthalenes. *Heteroatom Chem.* **15**, 530-542 (2004).

[253] Hehre, J. W., Radom, L., Schleyer, P. v.R. and Pople, J. A. *Ab Initio Molecular Orbital Theory*, Wiley, New York, **1986**.

[254] Glass, R. S., Andruski, S. W., Broeker, J. L., Firouzabadi, H., Steffen, L. K. and Wilson, G. S. Sulfur–sulfur lone pair and sulfur–naphthalene interactions in naphtha[1,8–*b*,*c*]–1,5–dithiocin. *J. Am. Chem. Soc.* **111**, 4036-4045 (1989).

[255] Modelli, A. and Venuti, M. Temporary π* and σ* anions and dissociation electron attachment in chlorobenzene and related molecules *J. Phys. Chem. A* **105**, 5836-5841 (2001).

[256] Modelli, A. and Jones, D. Temporary anion states and dissociative electron attachment in diphenyl disulfide. *J. Phys. Chem. A* **110**, 10219-10224 (2006).

[257] Zweig, A. and Hoffmann, A. K. Naphthalene 1,8–disulfide *J. Org. Chem.* **30**, 3997-4001 (1965).

[258] Teo, B. K. and Snyder-Robinson, P. A. Metal tetrathiolenes. 8. Molecular–structure of 2 isostructural 2–electron systems – $(PH_3P)_2(CO)XIR(C_{10}Cl_4S_4)$ (X=CL,H) – the first member of a novel series of metal tetrathiolene complexes. *Inorg. Chem.* **23**, 32-39 (1984).

[259] Mulliken, R. Electronic population analysis on LCAO–MO molecular wave function. I. *J. Chem. Phys.* **23**, 1833-1840 (1955).

[260] Oae, S., Nabeshima, T. and Takata, T. Unusual chemical behavior of 1,2–dithiaachenaphthene in the reactions with dinitrogen tetraoxide and aqueous bromine — In contrast to the ordinary oxidation with fenton reagent. *Heterocycles* **18**, 41-44 (1982).

[261] Bock, H., Brähler, G., Dauplaise, D. and Meinwald, J. One–electron oxidation of 1,8–chalcogen–bridged naphthalenes. *Chem. Ber.* **114**, 2622-2631 (1981).